Institute of Electrical Power Systems

Investigation and Validation of Stability for the Photovoltaic Integration into a Medium Voltage Grid Based on PHIL Testing

A Master thesis by
Carina Lehmal, BSc.

Supervisor
Ziqian Zhang, Dipl.-Ing. Dr.techn.

Reviewer
Ziqian Zhang, Dipl.-Ing. Dr.techn.
Lothar Fickert, Em.Univ.-Prof. Dipl.-Ing. Dr.techn.

September 2021

Graz University of Technology
Institute of Electric Power Systems
Inffeldgasse 18/I
8010 Graz
Austria

Head of Institute
Robert Schürhuber

Supervisor
Ziqian Zhang, Dipl.-Ing. Dr.techn.

Reviewer
Ziqian Zhang, Dipl.-Ing. Dr.techn.
Lothar Fickert, Em.Univ.-Prof. Dipl.-Ing. Dr.techn.

A Master thesis by
Carina Lehmal, BSc.

09 2021

Statutory Declaration

I declare that I have authored this thesis independently, that I have not used other than the declared sources / resources, and that I have explicitly marked all material, which has been quoted either literally or by content from the used sources.

Graz, 05.09.2021 Carina Lehmal

Eidesstattliche Erklärung

Ich erkläre an Eides statt, dass ich die vorliegende Arbeit selbstständig verfasst, andere als die angegebenen Quellen/Hilfsmittel nicht benutzt, und die den benutzten Quellen wörtlich und inhaltlich entnommenen Stellen als solche kenntlich gemacht habe.

Graz, am 05.09.2021 Carina Lehmal

Acknowledgements

First of all, I would like to express my sincerest gratitude to my supervisor, Dr. Ziqian Zhang, for his guidance starting from the beginning of the master thesis. His motivation to familiarize me with a topic that was foreign to me at the start and to patiently explain every concept and question in detail, building on the background I had already acquired during my bachelor and master's studies, helped me to expand my knowledge and to set up this master's thesis in a technically correct manner. During the realisation of the master thesis, he not only clarified the theoretical side and guided me concretely to the correct result in the mathematical models, but also actively supported me in the PHILlab during the execution of the experimental experiments. Due to our successful teamwork, the discussed topics of this master thesis as well as the experiments could be carried out thoroughly.

At this place, I would like to thank my Master's examiners Professor Dr. Schürhuber and Professor Dr. Krischan for their help in courses and their open ear whenever I had any questions. Their courses in my studies laid the foundations on which I was able to successfully build for this master's thesis.

Also, I am very grateful to Professor Dr. Lothar Fickert, who integrated me into his project in cooperation with the company Borealis Polyolefine GmbH and thus gave me the chance to be able to set up this master's thesis in the first place. He further enhanced my knowledge through in-depth discussions and passed on useful tips for considering the reasonableness of calculation, simulation and measurement results.

Next, I would like to thank the company Borealis Polyolefine GmbH for the opportunity to carry out this master thesis. I would especially like to mention Mr. Haslinger, who was always there for all performed measurements on company perimeters and who took perfect care of me when I had any questions. His commitment made it possible for me to get to know the company Borealis Polyolefine GmbH, attend meetings and gain an insight into working life.

Furthermore, I would like to thank the whole team of IEAN, especially DI Manuel Galler and DI Philipp Hackl, for the pleasant working environment, the meaningful technical discussions and help with all the small or big questions during measurements in the PHILlab.

Last, but most importantly, I would like to express my deepest gratitude to my mom and my friends. My mom's faith in me and unconditional love and support as well as all the long evenings with my friends that always put a smile on my face when I was not in such a positive mood.

Abstract

The integration of renewable energies into the voltage grid is becoming more and more important in order to meet the increasing requirements of a clean, safe and sustainable power supply. In this context, three-phase inverters play a very important role, as they are used to convert energy between different voltage forms and voltage levels and are thus the most important component when connecting photovoltaic energies and wind energies to the grid. However, due to their power electronic components, they suffer from instabilities themselves as well as from instabilities caused by dynamic interactions between inverter and voltage grid. Therefore, it is necessary to perform a stability analysis depending on the existing grid impedance before connecting an inverter to the grid.

In the present master thesis, the stability analysis of an 8 MW photovoltaic system into an existing grid at 6 kV medium voltage level is carried out. A model of the overall system is designed based on theoretical calculations and validated with on-site measurements. Building on this, an analysis of the static as well as dynamic stability is executed during subsequent measurements of the inverters in the test laboratory in order to be able to make a well-founded final statement. The inverter measurements are performed using the "power-hardware-in-the-loop" test method, which gives a very good overview of the behaviour of the whole system, while only the inverter is present as real equipment.

Kurzfassung

Die Integration von regenerativen Energien in das Spannungsnetz wird immer wichtiger, um den steigenden Anforderungen einer sauberen, sicheren und nachhaltigen Energieversorgung gerecht zu werden. Dabei spielen dreiphasige Wechselrichter eine sehr große Rolle, da sie verwendet werden um Energie zwischen unterschiedlichen Spannungsformen und Spannungsebenen umzuwandeln und damit der wichtigste Bestandteil beim Anschluss von Photovoltaik- und Windenergien ans Netz sind. Allerdings leiden sie durch ihre leistungselektronischen Komponenten selbst an Instabilitäten als auch an Instabilitäten durch dynamische Interaktionen zwischen Wechselrichter und Spannungsnetz. Deswegen ist es notwendig eine Stabilitätsbetrachtung vor Installation eines Wechselrichters in Abhängigkeit von der vorhandenen Netzimpedanz durchzuführen.

In der vorliegenden Masterarbeit wird die Stabilitätsbetrachtung einer 8-MW-Photovoltaikanlage in ein bestehendes Netz auf 6-kV-Mittelspannungsebene durchgeführt. Dabei wird anhand von theoretischen Berechnungen und Validierung dieser mit Messungen vor Ort ein Modell des Gesamtsystems entworfen. Darauf aufbauend kann bei nachfolgenden Messungen der Wechselrichter im Testlabor eine Analyse der statischen als auch dynamischen Stabilität erstellt werden, um so eine fundierte Endaussage treffen zu können. Die Messungen der Wechselrichter werden mittels der „Power-Hardware-in-the-Loop“-Testmethode durchgeführt, welche einen sehr guten Überblick des Verhaltens des Gesamtsystems gibt, während nur der Wechselrichter als reales Betriebsmittel vorhanden ist.

List of Symbols and Abbreviations

A	Cable cross-section
AA1-AA4	States of extruder motor and photovoltaic system
C_{pos}	Capacitance of the positive sequence
C_{zero}	Capacitance of the zero sequence
cosφ	Power factor
DPD	Distributed Power System
f	Frequency
f_s	Switching frequency
GNC	Generalized Nyquist criterion
IEC 61000-2-4	IEC norm
l_{cable}	Length of cable
L_{pos}	Inductance of the positive sequence
L_{zero}	Inductance of the zero sequence
I_v	Harmonic current
I_A	System current
i_{ref}	Reference current
i_S	System current
IGBT	Insulated-Gate Bipolar Transistor
Ki	Integral part of PI controller
Kp	Proportional part of PI controller
MV23	A feeder at the main busbar of the industry grid
MV24	A feeder at the main busbar of the industry grid
P	Active power of transformer
PHIL-test	Power-hardware-in-the-loop test
PI controller	Controller with proportional and integral part
PLL	Phase Locked Loop
PWM	Pulse Width Modulation

PV	Photovoltaic (DC part of PV system)
PV system	Photovoltaic plus inverter
R	Resistance of motor
R_{pos}	Resistance of the positive sequence
R_T	Transformer resistance
R_{zero}	Resistance of the zero sequence
SSM	Small signal modelling
S_{kV}	Short-circuit power at the connection point
S_A	Short-circuit power at installation of user
S_{PV}	Power of photovoltaic installation
t	Time, transformation ratio
THD	Total harmonic distortion ratio
TOR-D2	Technical and organisational rules for operators and users of grids - Part D2
ΔU	Voltage increase
U_{DC}	DC voltage, DC link voltage
u_K	Transformer short circuit ratio
U_{OS}	Transformer voltage at high-voltage level
U_{US}	Transformer voltage at low-voltage level
X_T	Transformer reactance
Y_W	Inverter admittance
Z_g	Grid impedance
Z_T	Transformer impedance
Z_W	Inverter impedance
Values with -0	Value at 50 Hz operating state
Values with -c	Controller variables
Values with -s	System variables
G_{xx}	Transfer functions

Table of Contents

1 Introduction

1.1 Motivation

In order for the present power grid to continue to comply with environmental concerns and regulatory requirements in the future, technology trends and energy storage besides further automation and communication must be implemented while still meeting the demand of multiplying consumers [1]. With regard to the required turnaround of a carbon-based conventional power grid towards a sustainable and low-emission one, renewable energies and their integration, as well as associated problems, must be taken into account. The focus in this process is on decarbonisation, decentralisation and digitalisation [1], [2], driven by the employment of electronic power converters [2]. While this transformation promotes modern power grids with high flexibility, sustainability and improved efficiency, it constitutes new challenges based on the power electronics and power converters [3], [2].

Considering the wide timescale control dynamics of power converters, the utilised control algorithm of the converters influences the stability properties of the converter, which in turn determine the stability of the entire system. In some cases, the cross coupling between the electromechanical dynamics and electromagnetic over voltages result in undesired oscillation like harmonics, inter-harmonics and resonances over a wide frequency range [2]. These in turn can cause disruptions in the power supply as well as premature aging and excessive stress of equipment and insulation even though the used technologies have been approved and certified for grid compatibility [3]. For this reason, first the causes must be identified and second the test and validation methodology revised [3], [4].

Literature sources describing these stability problems exist in every sector that uses energy as a propulsion option. In [5] the problem of harmonics is addressed from wind turbines side, in [6] and [7] for high-speed electric trains, and in [8], [9] and [10] for photovoltaics.

1.2 Current status of research

1.2.1 Steady-state validation

The steady-state discusses the first source of instability in a grid. This type of instability has existed since the beginning of the nationwide grid expansion and the ever-increasing interconnection of smaller sub-grids into a large interconnected grid, for example the ENTSOE grid in Europe [11].

Are AC generators operated parallel, oscillations occur in grid systems due to the power to phase-angle curve gradient interacting with the rotary inertia of the electric generator. Slight differences in the design of the loading and generators excite these oscillations continually. For this reason, damper windings have been installed in generators and the problem seemed to disappear.

Shortly after, the interconnection of power systems increased and the damper windings reached their limits. Both interconnected systems noticed the high external impedance of the other system. With that, the generator voltage becomes a function of angular swings, the voltage regulator steps in and as a result, negative damping becomes a negative side effect [11].

Nowadays coupled with cables, overhead lines and automatic control of power grids, oscillations in power grids have many sources specifying the natural resonance frequency completely by the network impedance itself.

Focussing now on the newer additions to the power grid with a power electronic interface like inverters, the switches inside the inverter operate with their own switching frequency. Now by the time a connection between inverter and grid is conducted, these two frequencies influence each other. Here an instability occurs as soon as the switching frequency is close to the resonance frequency of the grid. The occurring harmonics can be found in the voltage as well as in the current. Harmonics in voltage originate from parallel resonances and harmonics in current stem from serial resonances.

Briefly summarised, these oscillations cannot be eliminated, but their frequency and magnitude modified. Automatic controls of regulators is a big source for negative damping and the interconnection between power grids multiply oscillations affecting each equipment. Harmonics mostly cause additional heating of equipment and reduce the lifespan, performance and stability of the equipment [11].

1.2.2 Stability validation

Power system stability exists when the power system has the ability first to find a stable operation point and then to achieve it again in case of a physical disturbance. Throughout this process, the integrity of the complete system must be retained, meaning that the no part of the power system can fail its operation, except for the faulted elements or intentionally tripped ones to guarantee the continuity of the rest of the power system [11].

Since the power system represented by mathematical equations consists of a high-order nonlinear multivariable system, its dynamic performance depends of the constantly changing environment including the responses to loads, generator outputs, changes in topology and key operating parameters. The stability performance of a power system depends strongly on the type of disturbance. This disturbance can be both small and large, influencing the response of the power system and in turn affecting the grid equipment [11].

Normally, there are three types of system stability problems [12]:

- Steady-state stability: It exists an equilibrium point of the system, which the system can maintain.
- Small-signal stability: The system has the ability to return to the original operating point after a minor disturbance. This small perturbation is sufficiently small, that the system equations can be linearized.

- Large-signal stability: The system has the ability to switch from the original steady operating point to a new steady operating point after a large disturbance. Here most analysis takes place with Lyapunov stability.

Due to this, instability of the power system can have different forms, which gives importance to the analysis of the stability problems. Generally, the classification of power system stability is divided into three sub-areas [11]:

- Rotor angle stability
- Frequency stability
- Voltage stability

Rotor angle stability deals with the ability of synchronous machines to find an equilibrium between electromagnetic torque and mechanical torque under normal operating conditions as well as after a disturbance [11].

Frequency stability is concerned with maintaining a steady frequency, within the nominal range, after a large disturbance. The aim here is to restore the balance between generation and load with a minimum loss of load [11].

Voltage stability focuses on maintaining steady voltages on all busbars of the system under normal operating conditions as well as after disturbances. If the system loses its voltage stability, there can be a loss of load, loss of grid integrity and, consequently, a loss of synchronism of the rotor angles, which will cause synchronous machines to fail [11].

Besides the steady-state stability, for rotor angel stability and frequency stability, it makes sense to distinguish between a small and a large disturbance, as these have a different effect on the behaviour of the system and on the tools for mathematical description and design of simulation [11], [12].

1.2.3 Transient-state validation

With the transformation of the traditional centralised power system to a decentralised power system with many individual loads and generation, distributed power system (DPS) technology is becoming increasingly important. Through DPS, converters can be configured to behave in a certain way and can be controlled.

Since the control parameters are one of the most sensitive components for a stability analysis in this transient case, an inappropriate model does not equal reality values and forms an incorrect study. In general, inverters have a very high bandwidth to control them, which leads to a dynamic interaction between the inverter and the passive components of the system over a wide frequency range. When actuating the IGBTs, a PWM with high frequency is used and there is a dead-time in which the semiconductors are switched off between the duty cycles to avoid short circuits. These two circumstances add harmonics over a wide spectrum in addition to the fundamental frequency.

To filter out switching harmonics as well as possible, passive filters such as high-pass or low-pass filters made of RLC elements are used at the input of the inverter. These passive filters interact with the passive components of the overall system when the inverter is connected and thus lead to further harmonics [11].

However, with the addition of a complete inverter-grid model this results in complex systems with dynamic system interactions that lead to different stability problems [13].

In order to be able to analyse such systems, several analysis approaches exist, each having their own advantages and disadvantages.

Amongst several approaches the state-space-based approach, the transfer-function-based approach or impedance-based approach receive most of the attention of scientific studies in regard to feasibility in praxis.

1.) The state-space-based approach [12], [14], [15], [16], [17]:
This approach is already well known in the analysis of traditional power systems, therefore very well researched, and deployed in commercial software. In the state-space-based approach, the internal states and conditions of the system are precisely described by the eigenvalues and eigenvectors through the formation of the system state matrix.
However, since traditional power systems based on synchronous machines only have their dynamic focus at low frequencies, a detailed model of the connection between the inverter and the ac system in so-called inverter-based micro grids would have to be implemented for systems that are strongly driven by inverters.
From this, it can be concluded that the system state matrix has a high order and is inflexible in operation. A major disadvantage of the state-space-based approach is that the approach requires all controller parameters of the inverter to create a detailed model. Unfortunately, this information is rarely available from the inverter manufacturers, which means that no stability analysis can be conducted.

2.) The transfer-function-based/impedance-based approach [12], [18], [19], [20], [21]:
In contrast to the state-space-based approach, this approach only considers the relationship between input and output and neglects the condition of internal states. Through the analysation of the Bode plot or Nyquist plot of the open-loop transfer function or the pole-zero maps of the closed-loop transfer function it gives based on the conventional theory a result of the system stability.
In other words, this approach adopts a completely different strategy right from the start. It focuses on the interconnections between the system components and divides the existing grid and the inverter to be connected into two separate sub-systems.
In the case of a disturbance, the relationship between perturbation and output is of interest in this analysis approach and due to its applicability to a wide frequency range commonly used. Of these two subsystems, only the terminal behaviour is considered, which means that only the impedance and admittance are taken into account. By applying the Nyquist criterion to the

impedance ratio of the two subsystems, a judgement can be drawn regarding the stability between the two systems.

This means that no control parameters and internal circuits are required, neither from the existing grid nor from the inverter, but only by measuring the impedance or admittance, a clear statement can be made about the stability of the whole system. Based on this, the effect of both components can be clearly determined and suitable countermeasures can be derived.

The approach is good if ideal conditions of the external parameters can be assumed but might mask some instabilities.

In the most recent literature, the impedance-based stability criteria is preferred because it adapts better to changes in the system. After setting up the system, the non-linear system can be linearized around an operating state (small-signal modelling) and the stability can be determined using the Nyquist criterion, for example. Popular transformations are the transformation in dq-domain [22], harmonic linearization [23], modelling by dynamic phasors [24] and reduced-order method [25].

In order to be able to make a real statement about the stability based on the chosen criterion, it depends on the correct modelling of the inverter. Often, non-linear factors such as the control delay, the PLL and the inverter control dead-time are not taken into account, which means that the stability conclusion can be the opposite in reality. [13] suggests, that in high frequency range the control delay changes the system characteristic and is therefore necessary in the modelling, when looking at the stability characteristic in high frequencies.

In addition, it is only in the last few years that the difference between system and controller variables has really been taken into account and considered with a PLL transformation in different coordinate systems [26], [27], [28]. As a result, it is noticed that the non-linearity of the PLL has critical effects on the overall system stability [13].

Beyond models and simulations, often a test in reality to check the simulation results is missing in literature. Therefore, in this master thesis first a model is set up, based on analytical equations and then compared to the measurements of the laboratory test of the real hardware. This allows a more profound statement of stability to be achieved, which then corresponds to the reality in the application.

1.3 Aim and task description of this master thesis

In this master thesis, the focus is on a praxis example, where an 8 MW photovoltaic system is going to be installed parallel to an existing industry grid at a 6 kV medium voltage level. In this grid a 5.3 MW motor connected to a frequency converter with a 24-pulse-bride rectifier forms the relevant part of the production line and therefore must not fail its operation. Therefore, the key aspect of the master thesis is on the effect the photovoltaic system has on the industry grid.

In this master thesis, the following questions will be answered:

1.) How does the existing grid situation look like?
2.) Is there a change of the voltage situation for the existing grid when connected to the planned photovoltaic system?
3.) Has the planned photovoltaic system the right connection stability?
4.) Where do resonance instability and harmonics occur?
5.) What role plays the controller stability on the grid?
6.) What could be possible countermeasures in the future?

In order to be able to answer the questions of the task description, not only the steady-state but also the transient-state is considered. First, the existing grid system is calculated in the steady-state and a model is created for the planned photovoltaic installation. Then both are included in a simulation and voltage situation with and without the photovoltaic system analysed. Based on the results, an evaluation according to TOR-D2 and IEC 61000-2-4 follows, which describes the importance of the harmonics that occur in the grid.

Subsequently, the actual grid state is measured in a field test and compared with the simulation results of the calculated actual grid state. Based on this, the accuracy of the simulation can be determined and a statement about the genuineness can be made. Now the transient processes in the grid are considered. This is based on the validation process of [29] and divided into three steps.

1.) Small signal modelling of the system: Here the network and the photovoltaic installation are calculated in the dq-domain and control parameters are integrated into the models. These models use the impedance-based approach as a basis and can then be compared again with the simulation in order to make a statement about the validity of the simulation.
2.) Frequency sweeps of the simulation and the inverters in the laboratory: This can illustrate the behaviour of the grid system and the inverters over a wide frequency range and the stability of the individual components can be observed.
3.) PHIL-test: In this test, the simulation is connected to the hardware, i.e. the inverters, via the connection to a real-time system, and the overall system stability is examined when the inverters and photovoltaic are connected to the grid. Throughout the laboratory tests, two inverters from different companies are tested to show that depending on the inverter, the characteristics change and not every inverter is the right solution for the same problem.

Subsequently, these tests can be used to make a detailed statement about the effect of connecting the photovoltaic system to the grid. The structure of the master's thesis is accordingly aligned to this.

2 Steady-state validation

In chapter two, the first source of harmonics is highlighted. The processes of the industrial grid during the connection of photovoltaics, which occur in the steady state, are discussed.

There are three sections in the chapter. In the first section, the setup of the Matlab/Simulink simulation is described. In the second section, a grid analysis of the present status of the medium voltage grid is carried out according to TOR-D2 and IEC 61000-2-4. The TOR-D2 and IEC 61000-2-4 standards deal with disturbances occurring in a frequency range from 0 Hz to 9 kHz. The standards define compatibility levels for industrial and non-public power supply systems with nominal voltages up to 35 kV and a nominal frequency of 50 Hz or 60 Hz. The TOR-D2 is only used as a reference standard, since its values for the currents are not relevant for the industrial grid, but are a good guide. In the last section, the increase in voltage on the busbar is calculated due to the feed-in of the photovoltaic installation.

2.1 Design of the industry grid model

Before designing the simulation, the medium voltage grid circuit diagram is simplified into a single-line diagram for orientation. Afterwards, a simulation model can be created in Matlab/Simulink on the basis of it. The main components of the industrial grid are the connection transformer to the high voltage grid with 31.5 MVA, the main busbar with feeders for different types of loads and the planned photovoltaic system, which will be an additional feeder of the main busbar. The main feeder of the main busbar is the variable extruder motor, which is always needed for the production of the industrial grid. In Figure 1 two parallel three-winding transformers and a frequency converter represent it. The photovoltaic system is shown on the right side of the figure. Since it is not yet fixed in the setup whether a second transformer is used for the photovoltaic system for the purpose of the (n-1) criterion, the second transformer is drawn in dashed lines in the single-line diagram. During the simulation, it is possible to select between one transformer and two transformers connected in parallel with the help of a switch.

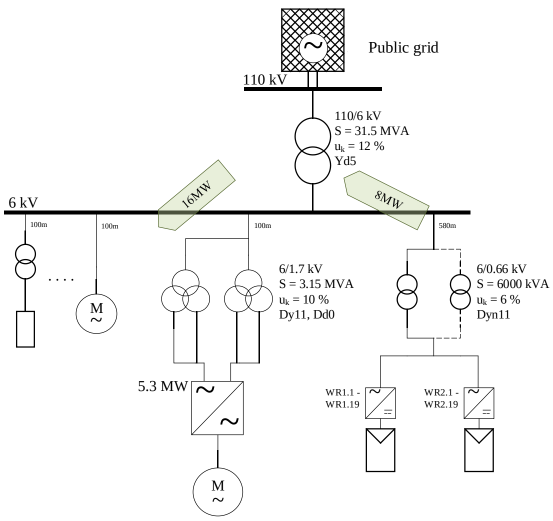

Figure 1: Grid single-line diagram

The simulation is performed in Matlab/Simulink, which is a state-of-the-art software for various engineering programming applications. Simulink is an add-on product to Matlab and is mainly used to create a wide variety of models. These models can be created with graphical blocks and generate curves directly in Simulink or send the calculated data to Matlab to generate diagrams there.

For the simulation in Simulink, the data of the individual components is taken into account and the values for the simulation are calculated accordingly.

Based on the single-line diagram the following simulation of the grid is set up in Figure 2.

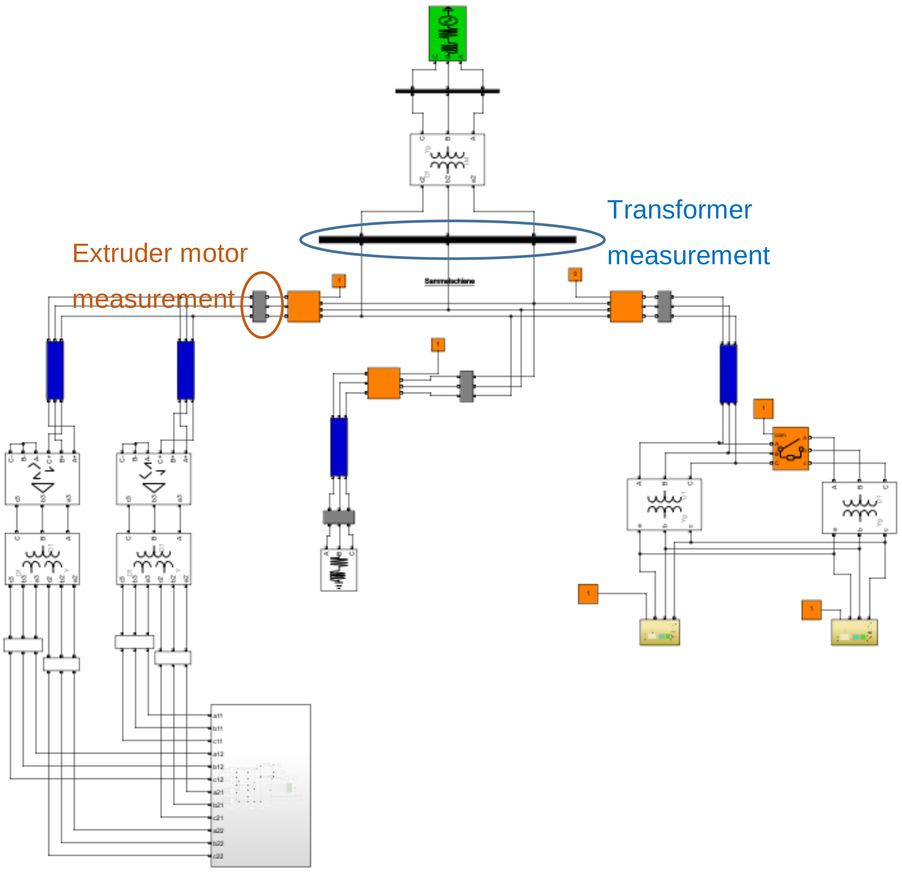

Figure 2: Simulation in Simulink

2.1.1 Calculation of equipment

For the calculation, most components are calculated following the data sheets of the medium voltage grid. Standard values are assumed for the cables connecting the individual parts and the photovoltaic installation.

2.1.1.1 Modelling of the main busbar feeder

Feeder MV23 represents the supply of the entire busbar and is connected to the voltage supply of the public grid via a Yd5 transformer. The 110 kV voltage received from the public grid is transformed to the 6 kV phase-to-phase voltage used at the plant site. In Simulink, a transformer module with a corresponding transformation ratio is used for the voltage transformation and the component data of the transformer calculated using the provided data sheets. See 2.1.1.4 for the calculation process.

2.1.1.2 Modelling of the Extrudermotor

The variable extruder motor with S = 2 x 3150 kVA is connected to feeder MV24 via the two transformers 20/21 connected in parallel. This feeder is very important for the industry grid's production and must therefore not lose its power. In Simulink, the three-winding transformer of the industry grid is described at this input by two transformer modules connected in series. The first transformer has a Zd switching group with a 1:1 transformation ratio, purely to realise the phase shift.

The transformer connected in series to it consists of the Dynd switching group and contains the correct transformation ratio and the component data. The component data is determined from the provided data sheets. See 2.1.1.4 for the calculation process.

A 12-pulse rectifier is connected to the second transformer. The rectifier is build using four separate bridge rectifier modules with the internal wiring according to the industry grid's construction plans. Since the motor connected in reality corresponds to a constant load, a resistor simulated the inverter and motor. Its value is determined from field test values (see chapter 4 for the field test results).

First, the DC link voltage of the frequency converter is determined.

$$U_{DC,no\ load} = 2 \cdot 1.7\ kV\ \cdot \sqrt{2} \approx 4.80\ kV \tag{1}$$

Taking into account an internal voltage loss of approximately 6 % the DC link voltage is reduced to:

$$U_{DC,load} = 4.80\ kV\ \cdot 0.94 = 4.51\ kV \tag{2}$$

With the DC link voltage and the measured active power of P = 0.64 MW, the resistance for the simulation is taken as R = 31.5 Ω in order to obtain consistent results with the subsequent simulation.

$$R = \frac{{U_{DC}}^2}{P} = \frac{(4.51\ kV)^2}{0.64\ MW} = 31.5\ \Omega \tag{3}$$

2.1.1.3 Modelling of cables

Pi equivalent circuit diagrams are used for cables, whereby the average construction data is obtained from typical data sheets. Based on a copper cable the conductivity at a temperature of 20 to 25 degrees Celsius is 56 m/Ωmm^2.

From that, the ohmic resistance can be derived according to the length and the cross-section of the cable. Here a minimum cross-section of 150 mm^2 is assumed, and the values calculated per 1 km.

$$R_{pos} = \frac{l_{cable}}{\gamma \cdot A} \tag{4}$$

A standard value for the reactance of the positive sequence is 0.13 Ω/km and the capacity is 0.25 μF/km. For negative sequence, the values are equal to the positive sequence values and for zero sequence 3.8 multiplies the values.

With these values, the inductivity of the cable is calculated for the positive sequence at a frequency of 50 Hz.

$$L_{pos} = \frac{X_{pos}}{2\pi f} \tag{5}$$

Thus, a cable of the simulation per 1km results in the values of:

Table 1: Cable values

R_{pos} = 0.1190 Ω/km	L_{pos} = 0.4138 mH/km	C_{pos} = 0.2500 μF/km
R_{zero} = 0.4524 Ω/km	L_{zero} = 1.6000 mH/km	C_{zero} = 0.1500 μF/km

2.1.1.4 Modelling of transformers

In the grid model, three different transformers are used. Each transformer is calculated according to the following equations.

To calculate the data of the windings of a transformer the main equation for the impedance of a transformer is used. For the voltage the value at high-voltage level of the transformer is used and later via transformation ratio transferred to low-voltage level.

$$Z_T = u_k \cdot \frac{{U_{OS}}^2}{S_T} \tag{6}$$

The empirical formula 5 kW/MVA is used for the calculation of the losses and with it, each reactive power of a transformer computed.

$$P = \frac{5\ kW}{1\ MVA} \cdot S_T \tag{7}$$

Based on the reactive power, the ohmic resistance can be derived.

$$R_T = P \cdot \frac{{U_{OS}}^2}{S_T} \tag{8}$$

With the impedance of the transformer and the ohmic resistance, the reactance can be calculated following the relation of the resistance pointer in the complex plane.

$$X_T = \sqrt{{Z_T}^2 - {R_T}^2} \tag{9}$$

Then the transformation ratio of the transformer is calculated and the values at low-voltage level are calculated.

$$t = \frac{U_{OS}}{U_{US}} \tag{10}$$

Values at low-voltage level:

$$R_{T,US} = \frac{R_{T,OS}}{t^2} \qquad X_{T,US} = \frac{X_{T,OS}}{t^2} \tag{11}$$

For the Simulink simulation, which applies a complete T equivalent circuit diagram, the impedance is subdivide per the number of windings of the transformer, therefore, the $R_{T,US}$ and $X_{T,US}$ must be divided by the number of windings of this transformer (e.g. 2-winding transformer – divided by 2; 3-winding transformer – divided by 3).

$$R_{T,OS,US,sim} = \frac{R_{T,OS}}{number\ of\ windings} \qquad X_{T,OS,US,sim} = \frac{X_{T,OS}}{number\ of\ windings} \tag{12}$$

Finally, the values are transformed into the p.u.-system for easier integration. The p.u-system is used to turn a physical variable into a fraction of a reference value. The p.u-system can be employed for impedances, voltages, currents and power calculations.

$$R_{pu,T,OS,US} = R_{T,OS,US,sim} \cdot \frac{S_T}{U_{OS,US}} \qquad X_{pu,T,OS,US} = X_{T,OS,US,sim} \cdot \frac{S_T}{U_{OS,US}} \tag{13}$$

Based on equations (6) to (13) all three existing transformers can be calculated.

Transformer 1: Represents the transformer between public grid and the medium voltage grid.

Table 2: Values for transformer 1

Datasheet	Calculation	
110 kV / 6 kV, 2 wdg.	t = 18.33	
S_T = 31.5 MVA	P = 157.5 kW	
u_k = 12 %	$R_{T,OS,sim}$ = 0.96 Ω	$X_{T,OS,sim}$ = 23.03 Ω
	$R_{T,US,sim}$ = 0.0029 Ω	$X_{T,US,sim}$ = 0.069 Ω

Transformer 2: Represents the transformer between 6 kV busbar and extruder motor

Table 3: Values for transformer 2

Datasheet	Calculation	
6 kV / 1.7 kV, 3 wdg.	t = 3.53	
S_T = 3.15 MVA	P = 15.75 kW	
u_k = 16 %	$R_{T,OS,sim}$ = 0.019 Ω	$X_{T,OS,sim}$ = 0.379 Ω
	$R_{T,US,sim}$ = 0.0015 Ω	$X_{T,US,sim}$ = 0.0305 Ω

Transformer 3: Represents the transformer between 6 kV busbar and photovoltaic installation

Table 4: Values for transformer 3

Datasheet	Calculation	
6 kV / 660 V, 2wdg	t = 9.09	
S_T = 6 MVA	P = 30 kW	
u_k = 6 %	$R_{T,OS,sim}$ = 0.015 Ω	$X_{T,OS,sim}$ = 0.179 Ω
	$R_{T,US,sim}$ = 0.00018 Ω	$X_{T,US,sim}$ = 0.0022 Ω

2.1.1.5 Modelling of other loads

In the simulation, all feeders except MV23 and MV24 of the busbar are combined into a common load on the busbar, since no further information from them is needed. This load is initialised as a three-phase load with an active power generation of 16 MW and a reactive power generation of 7 MW. These values originate from the field test measurement (see chapter 4).

2.1.1.6 Modelling of photovoltaic and inverter

The photovoltaic installation is included as a separate feeder on the busbar. The transformer used is again included with a Dyn11 transformer module. The component values are calculated according to documentation. After the transformer, the photovoltaic installation is simulated. The photovoltaic installation is constructed as a radial grid with two main feeders connected to several photovoltaic panels. The photovoltaic is modelled with a generalized model, since in steady-state only the relation to reality is of interest. Each feeder consists of a phase-locked loop control with a current control loop and an L-C filter. For the component values of the L-C filter, the data sheets of inverter 2 are used.

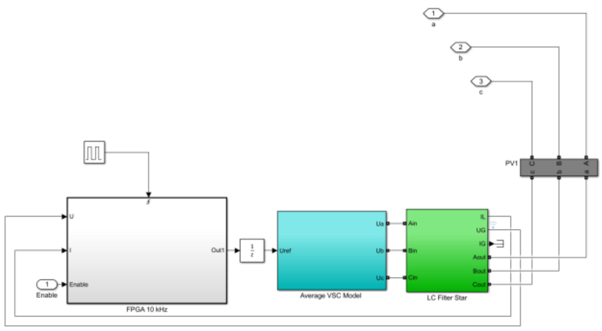

Figure 3: Simulation of the photovoltaic system

In Figure 3 the simulation of the photovoltaic system is displayed. The grey block is a three-phase voltage and current measurement. In the green block, the output filter circuit of the inverter based on the values of inverter 2 is included. The cyan block consists of a three-phase voltage source since the photovoltaic system produces a voltage that is feed into the grid. The white block contains the control equipment of the inverter. In the block, the voltage and current values are first transferred into the dq-domain, then the q-component sent into the PLL, from which the angular frequency is gained for the following PI controller. Afterwards the coupling between d and q component is added before the voltage and current are transferred back to the stationary abc-domain and sent to the cyan block to control the voltage source in it.

2.2 Harmonic analysis

2.2.1 General

The harmonic analysis is carried out according to guideline "Technical and organisational rules for operators and users of grids - Part D: Special technical rules / Main section D2: Guideline for the assessment of system perturbations" short TOR-D2 [30] and the IEC 61000-2-4 [31]. TOR-D2 is used to calculate the emission levels of harmonic currents and IEC 61000-2-4 specifies the limits for the maximum permissible harmonic voltages. Here, the TOR-D2 is only used as a guide and its reference values are considered as comparison values, since the currents occurring in the industrial network are not significant as long as the voltage values do not exceed the limits of IEC 61000-2-4.

Harmonics are described by constant, periodic deviations of the nominal voltage or the nominal current from the sinusoidal form and generate additional oscillations to the fundamental oscillation, which are superimposed on it. These harmonics have a frequency that is an integer multiple of the main frequency. Harmonics are caused by equipment with non-sinusoidal current consumption. In the case of the existing medium voltage grid, this is the extruder motor with rectifier on the busbar. If high harmonics occur in the main voltage, they can affect the main operation as well as the electrical equipment and grid users, in the sense of shortening the service life, malfunctions and malfunctions [30].

2.2.1.1 Grid codes

The plant-internal connection point MV24 is selected as the connection point of the extruder motor, since the electromagnetic compatibility and the interference phenomena are to be considered at this point. In the case of the interference phenomena, both the harmonics of voltage and current are evaluated as well as voltage deviations in the simulation of the planned photovoltaic system. For the used extruder motor, a 24-pulse rectifier is utilised due to the two parallel-connected three-winding transformers. As a result of this 24-pulse rectifier, the highest amplitudes of the occurring harmonics occur at the 23rd and 25th harmonics.

According to the IEC 61000-2-4, the industry grid is situated in class 3, since power converters feed a major part of the loads, and some loads fluctuate rapidly. Accordingly, a higher interference level than for a public grid may occur.

- Voltage deviation: +10 % to -15 %
- Frequency deviation: +/- 1 Hz
- Voltage THD: 10 %
- Harmonic levels according to Table 5

Table 5: IEC 61000-2-4 harmonic limits

Order	**% of U_n**
23	2.8
25	2.6

According to the TOR-D2 table, harmonics of 23rd and 25th order result for the currents in $p_v = 1$.

Table 6: TOR-D2 harmonic current limits

v	3	5	7	11	13	17	19	>19
p_v	6 (18)	15	10	5	4	2	1,5	1

2.2.2 Basic information on the assessment of the photovoltaic system and the 5.3 MW extruder

The rules given in the TOR-D2 are, according to their own definition, not mandatory for the assessment of the parallel operation of the photovoltaic installation with the 5.3 MW extruder motor. However, they are used as orientation in this report.

In this sense, in addition to the TOR-D2 compliance of the photovoltaic installation, the TOR-D2 compliance of the already existing connection of the 5.3-MW extruder motor is also investigated.

The harmonic analysis is carried out in two steps in the following:

- Rough analysis
- Detailed analysis

For this purpose, the network is set up in Matlab/Simulink in advance and the equipment data is calculated with the corresponding data sheet values (see chapter 2.1).

2.2.3 Rough analysis regarding the necessity of a harmonic analysis

According to the technical-organisational rules, a connection assessment can be omitted if the ratio of short-circuit power S_{kV} at the connection point V to the connection power of the installation of a network user S_A satisfies the applicable condition:

Medium voltage:

$$\frac{S_{k\,V}}{S_A} \geq 300 \tag{14}$$

The low-voltage side of the 31.5 MVA transformer, i.e. the 6 kV busbar, is selected as the connection point.

<u>Rough analysis for the photovoltaic system</u>

The short-circuit power S_{kV} is calculated by the transformer to the public grid operator and results in:

$$S_{k\,V} = \frac{S_{Trafo}}{u_k} = \frac{31.5\ MVA}{0{,}12} = 263\ MVA \tag{15}$$

The system power S_A comes from the photovoltaic system itself and results in the case of feeding in pure active power:

$$S_A = P_A = 8\,MW \tag{16}$$

This results in the ratio:

$$\frac{S_{k\,V}}{S_A} = \frac{263\,MVA}{8\,MVA} \sim 32 \tag{17}$$

The value 32 is smaller than 300 and therefore means that a further detailed analysis of the individual harmonics must be carried out for the photovoltaic installation.

<u>Rough analysis for the 5.3 MW extruder</u>

The short-circuit power S_{kV} corresponds to the value from above.

The system power S_A is calculated from the connected extruder motor to the 6 kV busbar:

$$S_A = \frac{S_{Motor}}{cos\varphi} = \frac{5.3\,MW}{0{,}9} = 5{,}88\,MVA \tag{18}$$

This gives the ratio to:

$$\frac{S_{k\,V}}{S_A} = \frac{269\,MVA}{5{,}88\,MVA} \sim 46 \tag{19}$$

The value 46 is less than 300 and therefore means that a further detailed analysis of the individual harmonics for the industry grid must be carried out.

Since the rough analysis cannot be omitted in either case, a further connection assessment is made in the next section.

2.2.4 Analysis of the individual emitted harmonic currents

First, according to TOR-D2 the harmonic load is classified and assigned to group 2 (equipment with medium and high harmonic emission, including 6-pulse converters, three-phase controllers, electronically controlled AC motors, etc.).

This harmonic load is subsequently divided into four different installation cases in combination with the photovoltaic installation and each installation case is treated individually.

According to TOR-D2, emission limit values are calculated for the individual harmonic currents and the total of all harmonic currents as a basis for comparison with the values of the simulation.

2.2.4.1 Emission limit values for individual harmonic currents according to TOR

$$\frac{I_v}{I_A} \leq \frac{p_v}{1000} \cdot \sqrt{\frac{S_{k\,V}}{S_A}} \tag{20}$$

I_v .... Harmonic current, in A

I_A .... System current, in A

p_v .... Proportionality factor

v ……… Ordinal number of harmonics

$S_{k\,V}$ .... (Mains) short-circuit power at the point of connection V, in VA

S_A .... Connected power of the grid customer's system, in VA

The system current is calculated based on the power of the extruder motor and follows on:

$$I_A = \frac{S_{Motor}}{\sqrt{3} \cdot U_{SS}} = \frac{5.88\,MVA}{\sqrt{3} \cdot 6\,kV} = 565.8\,A \tag{21}$$

From this, the emission limit value for the individual harmonic currents I_v can be calculated.

$$I_v \leq I_A \cdot \frac{p_v}{1000} \cdot \sqrt{\frac{S_{k\,V}}{S_A}} = 565.8\,A \cdot \frac{1}{1000} \cdot \sqrt{\frac{263\,MVA}{5.88\,MVA}} = 3.8\,A \tag{22}$$

2.2.4.2 Emission limit values for the total of all harmonic currents THD_i according to TOR

$$THD_{i\,A} \leq \frac{20}{1000} \cdot \sqrt{\frac{S_{k\,V}}{S_A}} \tag{23}$$

$THD_{i\,A}$ ... Total harmonic content of the grid customer's system

$S_{k\,V}$ .... (Mains) short-circuit power at the connection point V, in VA

S_A .... Connected power of the grid user's system, in VA

For the medium voltage grid, the grid data results in a $THD_{i\,A}$ of:

$$THD_{i\,A} \leq \frac{20}{1000} \cdot \sqrt{\frac{S_{k\,V}}{S_A}} = \frac{20}{1000} \cdot \sqrt{\frac{263\,MVA}{5.88\,MVA}} = 13.4\,\% \tag{24}$$

The medium voltage grid must comply with these two calculated emission limits at the 6 kV busbar in order to ensure functioning grid operation.

2.2.4.3 Calculation

To calculate the results, the Simulink model of the entire grid is used and an FFT analysis is performed up to a frequency of 5000 Hz.

This part of the analysis is checked depending on the possible installation cases (extruder motor ON/OFF or photovoltaic system feed-in ON/OFF) for the different combinations:

Table 7: Investigated states

	Extrudermotor off	Extrudermotor on
PV off	AA1	AA2
PV on	AA3	AA4

The state AA2 is the existing grid condition and AA4 the planned future state.

In the simulation, the measurement of the THD of the voltage is carried out at the 6 kV busbar and the measurement of the THD of the current is carried out at the 110/6 kV transformer.

It should be noted that when measuring the simulation on the busbar, only the extruder motor and the planned photovoltaic system are taken into account and all other harmonic sources are fictitiously switched off.

System status AA1 (motor = OFF, PV feed = OFF)

Analysis of voltage:	**THD in %**	**U_{RMS} in V**	**H_{23} in %**	**H_{25} in %**
	0	5985	0	0

In this system state, both the extruder motor and the photovoltaic installation are switched off. This state is confirmed by the 0 % THD value of the voltage[1].

System status AA2 (motor = ON, PV feed = OFF): present status of plant operation

Analysis of voltage:	**THD in %**	**U_{RMS} in V**	**H_{23} in %**	**H_{25} in %**
	2,2	5969	1,27	1,49

In AA2, only the extruder motor is used on the busbar. In this system state, the highest percentages of harmonics in voltages and current occur at the 23rd and 25th harmonics. The current harmonics have a value of H_{23} equal to 1.69 % and H_{25} equal to 1.76 %. If these values are added together squared, they give almost the complete THD_i value. Converted to the total effective current I_{eff}, the amplitude of the 23rd harmonic is 10.63 A and of the 25th harmonic 11.07 A. These values are above the values derived of the maximal allowed current values of H_{23} < 3.8 A and H_{25} < 3.8 A respectively. However, the THD_i (total) value does not exceed the 13.5 % value previously calculated from the standard.

[1] Note: Due to the simulation, a current of 44 mA flowing into the 6-kV busbar results when the circuit breakers are open, which corresponds to a "background noise" of 1.5*10-5 of the transformer rated current and is considered a satisfactory measure of the calculation accuracy.

System status AA3 (motor = OFF, PV feed = ON)

Analysis of voltage:	THD in %	U_{RMS} in V	H_{23} in %	H_{25} in %
	0,15	6018	0,01	0,01

With pure feed-in by means of a photovoltaic system, the THD values obtained for current and voltage are very low. From this, considering AA3, it can be concluded that the 24-pulse rectifier circuit of the extruder motor is responsible for the majority of the harmonics.

System status AA4 (motor = ON, PV feed = ON)

Analysis of voltage:	THD in %	U_{RMS} in V	H_{23} in %	H_{25} in %
	1,58	6008	0,9	1,1

As noted earlier, the highest percentages of harmonics occur at the 23rd and 25th harmonics. In AA4, the current harmonics have a value of H_{23} equal to 12.52 % and H_{25} equal to 13.38 %. If these values are added together squared, they result in almost the complete THD_i value.

Converted to the total effective current I_{eff}, the amplitude of the 23rd harmonic is 7.83 A and of the 25th harmonic 8.36 A. These values are above the values derived above AA2, which is the more critical case.

These values exceed the limit values of H_{23} < 3.8 A and H_{25} < 3.8 A derived above. The THD_i value also exceeds the 13.5% value previously calculated using the standard.

2.2.4.4 Results and conclusion

Reference values from IEC 61000-2-4:

Table 8: IEC 61000-2-4 summary of maximum allowable voltage values

Voltage deviation in %	Voltage THD in %	Voltage increase of 23rd order in %	Voltage increase of 25th order in %
+10 to -15	10	2.8	2.6

Reference values from the TOR-D2:

Table 9: TOR-D2 summary of maximum allowable current values

$THD_{i\,A}$ in %	I_v in A
13.4	3.8

The harmonic currents in AA2 and AA4 exceed the emission limit values of TOR-D2, but since the medium voltage grid is an industry grid and the voltage THD is completely unproblematic, no further problems are detected. In addition, the 50-hertz voltage deviation, calculated in 2.3, introduces no problem.

Comparison of the individual system states, THD values and harmonic components:

Table 10: Steady-state harmonic voltage summary

Analysis of voltage:	**THD in %**	**U_{RMS} in V**	**H_{23} in %**	**H_{23} in V**	**H_{25} in %**	**H_{25} in V**
AA1	0	5985	0	0	0	0
AA2	2,2	5969	1,27	75,81	1,49	88,94
AA3	0,15	6018	0,01	0,60	0,01	0,60
AA4	1,58	6008	0,9	54,07	1,1	66,09

2.3 Feed-In or withdrawal of power

Typically the withdrawal or feed-in of active and reactive power changes the voltage situation in electrical networks.

- Case 1: Withdrawal of active power and/or inductive reactive power manifests itself in a voltage drop
- Case 2: Feed-In of active power and/or inductive reactive power manifests itself in a voltage increase

The methodology behind both cases is the same, only the sign must be reversed. The following analysis is carried out in case 1, when energy is withdrawn.

2.3.1 Description of the calculation

For the calculation of the voltage drop at the main impedance, a distinction must be made whether the load is given as impedance or as power. When calculating with a (constant) load impedance, this can be combined in series with the main impedance to form a total impedance, and the voltages can be derived from the voltage divider rule.

On the other hand, at constant power, the current drain decreases as the voltage increases and thus the impedance apparently increases because of this voltage dependence. With current withdrawal, the situation are reversed.

Based on this formulation, the equivalent circuit and phasor diagram are illustrated in Figure 4 for one single-phase.

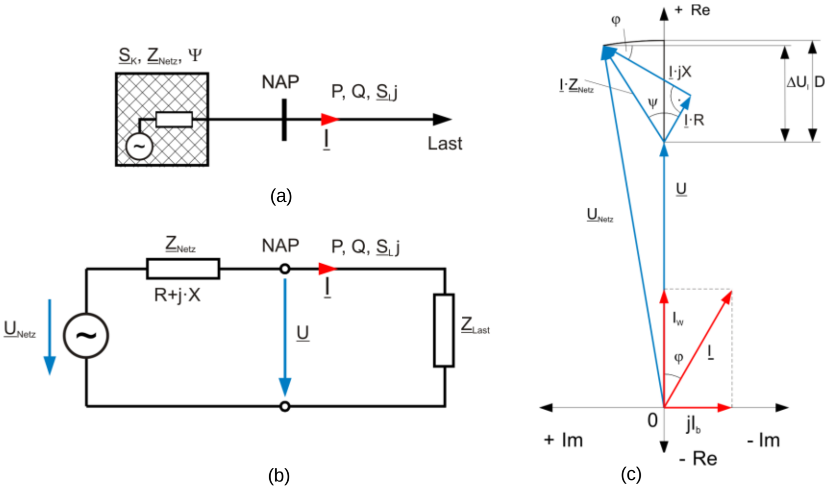

Figure 4: (a) Single-phase equivalent circuit (b) equivalent circuit (c) phasor diagram of currents and voltages

According to the phasor diagram, the longitudinal voltage drop along the grid impedance can be calculated with:

$$\underline{\Delta U} = \underline{I}_R \cdot \underline{Z}_N \tag{25}$$

In praxis, the longitudinal voltage drop can be approximated very well from the projection of the longitudinal voltage drop with $\underline{I}_w \cdot R$ and $\underline{I}_b \cdot jX$ onto the real axis. The current is projected with the phase angle φ and the voltage drop equation rewritten.

$$\underline{\Delta U} = \underline{I}_R \cdot \underline{Z}_N = R \cdot \underline{I}_w \cdot cos\varphi + X \cdot \underline{I}_b \cdot sin\varphi \tag{26}$$

Now the expression for the currents can be replaced by the representation of the power equations.

$$\Delta U = R \cdot \underline{I}_w \cdot cos\varphi + X \cdot \underline{I}_b \cdot sin\varphi = R \cdot \frac{P_L}{U} + X \cdot \frac{Q_L}{U} \tag{27}$$

For a three-phase system, the relative longitudinal voltage drop (phase-phase voltage), related to the phase-phase voltage U_N in p.u, is obtained from this by simple transformations:

$$\Delta u = \frac{\Delta U}{U_N} = \frac{P \cdot R + Q \cdot X}{U_N^2} \tag{28}$$

Based on this equation the voltage drop or voltage increase at a certain point of the grid is calculated, considering the grid parameters. The calculation is carried out for the busbar and for the photovoltaic installation.

For the following calculation it is assumed that the following values are known:

- impedance of the supply transformer (resistance and inductance of windings)
- active power consumption P_L
- reactive power consumption Q_L

2.3.2 Grid parameters

For the medium voltage grid, Figure 1 is used as a basis. The parameters for the transformers from chapter 2 after taking the number of windings into account apply.

Transformer 1: Represents the transformer between the public grid and the medium voltage grid. For the calculation, the values at low-voltage side are used since the busbar is at 6-kV level.

Table 11: Data of transformer 1

Datasheet	Calculation	
110 kV / 6 kV, 2 wdg.	t = 18.33	
S_T = 31.5 MVA	P = 157.5 kW	
u_k = 12 %	$R_{T,OS}$ = 1.9 Ω	$X_{T,OS}$ = 46.0 Ω
	$R_{T,US}$ = 0.0057 Ω	$X_{T,US}$ = 0.137 Ω

Cable to photovoltaic installation: For the calculation a cable cross-section of 240 mm² aluminium is assumed.

Based on this information the resistance and reactance are calculated with a length of 580 m.

$$R_{cable} = \frac{l}{\gamma \cdot A} = \frac{580\ m}{34\ ^{Sm}/_{mm^2} \cdot 240 mm^2} = 0{,}0711\ \Omega \tag{29}$$

To determine the reactance, the standard value 0.13 Ω/km is used and multiplied by the length.

$$X_{Kabel} = x' \cdot l = 0{,}13\ ^{\Omega}/_{km} \cdot l = 0{,}13\ ^{\Omega}/_{km} \cdot 0.58\ km = 0{,}0754\ \Omega \tag{30}$$

Photovoltaic installation: The worst-case scenario for the photovoltaic system is an operation not with complete real power (cosφ=1) but also with the feed-in of reactive power (for example cosφ=0.95) and the closing of any coupling points in the photovoltaic installation, so that the photovoltaic installation is carried out in radial operation, and represented with basically only one feeder. Because of only one single output at the end of the cable, the current flows through the entire cable (worst-case).

With an active power generation of $P_{PV} = 8.0\ MW$ and a $\cos\varphi = 0.95$ the apparent power is calculated.

$$S_{PV} = \frac{P_{PV}}{\cos\varphi} = \frac{8\ MW}{0.95} = 8{,}42\ MVA \tag{31}$$

Now the reactive power can be calculated based on the power relationship between apparent power, active power and reactive power.

$$Q_{PV} = \sqrt{{S_{PV}}^2 - {P_{PV}}^2} = \sqrt{8{,}42^2 - 8{,}0^2} = 2{,}63\ Mvar \tag{32}$$

2.3.3 Calculation

With the grid parameters, Formula (28) is now used to calculate the voltage increase.

The voltage rise at the end of the cable with the fictional single infeed is given by:

$$\Delta u = \frac{\Delta U}{U_N} = \frac{P_{PV} \cdot R + Q_{PV} \cdot X}{U_N^2} \tag{33}$$

$$= \frac{8{,}0\ MW \cdot (0.0057\ + 0{,}0711)\Omega + 2{,}63\ Mvar \cdot (0.137\ + 0{,}0754\ )\Omega}{(6\ kV)^2}$$

$$= \frac{0.62\ + 0.56}{36} = 0.0326 = 3.3\ \%$$

According to Formula (33) the voltage increase at the photovoltaic installation equals 3.3 % in the worst case (single infeed at the end) and 1.65 % in reality, since with a distributed feed the value is halved due to the more equal infeed situation.

The calculation for the voltage increase at the 6 kV busbar is quite similar. The voltage at the industry grid busbar with a feed-in of 8 MW only increases by 1.1 %.

The voltage rise at the beginning of the cable with the fictional single infeed is given by:

$$\Delta u = \frac{\Delta U}{U_N} = \frac{P_{PV} \cdot R + Q_{PV} \cdot X}{U_N^2} \tag{34}$$

$$= \frac{8{,}0\ MW \cdot (0.0057\ + 0)\Omega + 2{,}63\ Mvar \cdot (0.137\ + 0)\Omega}{(6\ kV)^2}$$

$$= \frac{0.045\ \ + 0.36}{36} = 0.0113 = 1.1\ \%$$

2.3.4 Assessment

Both voltage increases are not critical at any point in the network. Nevertheless, it is recommended to pay attention to a corresponding minimum cable cross-section, e.g. 240 mm^2 aluminium or 150 mm^2 copper, as the current load is too high for one single cable harness of the photovoltaic installation.

From the equations, the contribution of the reactive power to the voltage increase is quite high. At both point in the grid, the reactive power feed actually causes the substantial voltage increase.

Therefore, it is recommended to operate the photovoltaic system with $cos\varphi = 1$ in the sense of nearly constant voltage.

2.4 Conclusion of steady-state validation

In steady-state, two different calculations are performed. The first calculation shows the harmonic voltages and currents that occur when the photovoltaic system is connected to the industrial grid.

In order to be able to make a statement about stability for the calculated values, the standards IEC 61000-2-4 and TOR-D2 are used. According to the values of the calculation in comparison with the maximum emission limits permitted in the standard, it can be stated that the voltage limits do not lead to a problem with any of the harmonics considered and that the voltage situation in the industrial grid therefore functions safely and reliably.

Therefore, the consideration of the current values is only an additional analysis, which is neither obligatory for an industrial network, nor does it have to be adhered to. It is carried out purely out of interest in the current conditions in the sense of a possible overload of equipment. Here, some harmonics exceed the limit values.

3 Transient-state validation

In chapter three, the second source of harmonics is highlighted. The processes of the inverter, which occur in the transient case, are further discussed.

On this basis, the grid model and the inverter are modelled analytically and compared with the simulation model of the photovoltaic installation. In the first section, the stability criterion is described in more detail, then the modelling of the individual parts is carried out and in the last section the results are compared and an outlook on an unstable grid is given.

3.1 Impedance-based approach

As described in the stability overview (chapter 1), the use of the impedance-based approach has numerous advantages, especially if more than one inverter should be connected, as not every inverter has to remodelled and its loop stability repeated. However, designing an equivalent circuit of an inverter based on the impedance-based stability criterion produces one conceptual problem. Depending on the view direction both, the grid, but also the inverter can be the source, yielding in two opposite stability conclusions. Hence, the original impedance-based stability criterion should be revised [18].

3.1.1 Impedance-based equivalent circuit

In the original impedance-based stability criterion, a voltage source is used as a representation of the source, so the system is stable when unloaded. In contrast, most inverters are controlled via current-injection mode, meaning that their behaviour does not equal a voltage source. Furthermore, current sources in power applications are built via inductors with an active current control. So, this kind of source would not work with an open circuit connected to its output, since the current has no external path to flow. Therefore, the inverter has to be represented by a current source [18].

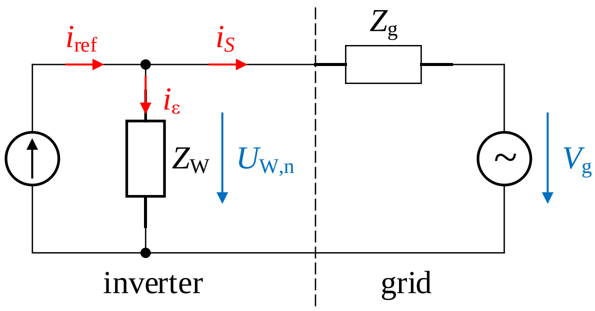

Figure 5: Impedance-based equivalent circuit

In this circuit, a Norton equivalent circuit parallel to the output impedance of the inverter Z_W represents the current source. It is noted that the inverter impedance is not a real hardware quantity but depends control design of the inverter. The control methods and parameters play the biggest role here but also the hardware part like the inverter design, namely the output filter, and the used PWM generation.

The grid impedance is modelled as a grid impedance Z_g with an ideal voltage source connected in series to the inverter circuit. Based on this model both subsystems are stable on their own. The inverter is expected to be stable when the grid impedance is zero and the grid voltage is stable without the inverter, since then the circuit is unloaded [18].

3.1.2 Impedance-based stability criterion

Considering the equivalent circuit, the inverter output current can be calculated.

$$i_S(s) = \frac{i_{ref}(s) \cdot Z_W(s)}{Z_W(s) + Z_g(s)} - \frac{V_g(s)}{Z_W(s) + Z_g(s)} \tag{35}$$

Formula (35) can be rearranged to:

$$i_S(s) = \left[i_{ref}(s) - \frac{V_g(s)}{Z_W(s)} \right] \cdot \frac{1}{1 + Z_g(s)/Z_W(s)} \tag{36}$$

From system stability analysis it is clear, when the ratio $Z_g(s)/Z_W(s)$ satisfies the Nyquist criterion, the inverter grid system is stable. Depending on the Nyquist plot of $Z_g(s)/Z_W(s)$ the stability margin of the system can be checked. Deduced from the stability criterion the inverter impedance should be as high as possible to make a wide stability margin possible. Therefore, the inverter control parameters plays a big role in an inverter-grid system and is an important performance index for the system. At the same time, it is a simple feature to compare different inverters with each other [18].

3.1.3 Nyquist criterion

When using the inverter impedance instead of the inverter admittance (Y = 1/Z) in Formula (36), the formula can be further converted.

$$i_S(s) = \left[i_{ref}(s) - V_g(s) \cdot Y_W(s) \right] \cdot \frac{1}{1 + Z_g(s) \cdot Y_W(s)} \tag{37}$$

Here the term multiplied with the terms in the brackets resembles a closed-loop transfer function of a negative feedback control system. It has a forward gain of one and a feedback gain of $Z_g(s) \cdot Y_W(s)$ or from formula (36) $Z_g(s)/Z_W(s)$. Regarding linear control theory, this gives a stable system if and only if $Z_g(s) \cdot Y_W(s)$ or $Z_g(s)/Z_W(s)$ satisfies the Nyquist criterion.

The corresponding control circuit is shown in Figure 6.

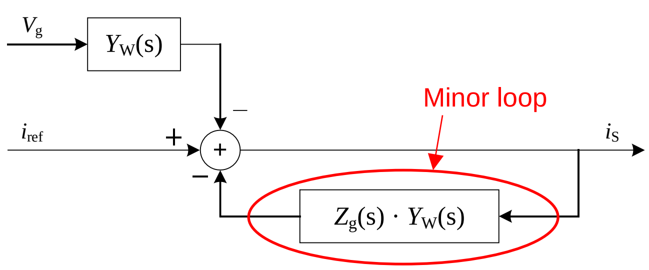

Figure 6: Control circuit

In Figure 6 the inverter current i_{ref} and the inverter admittance represent the stability of a inverter, which is connected to an ideal grid. The impedance ratio of inverter admittance and grid impedance indicate the stability in relation to the grid impedance, also called minor loop [12].

To examine the impedance ratio between grid and inverter system the Nyquist criterion or the generalised Nyquist criterion is used. The difference in use depends on the modelling of the inverter impedance. Is the inverter modelled as sequence impedances, the Nyquist criterion should be applied. Is the inverter modelled in the dq-frame with dq-impedance, the generalised Nyquist criterion (GNC) for multi-input-multi-output systems is the right choice. The difference between the two types is the usable passive region in which the system is stable. Based on the GNC a stability criterion on the basis of the frequency-domain passivity theory can be assembled [12]:

“A linear, continuous system G(s) is passive if 1) G(s) is stable without RHP poles and 2) the real part of G(jω) is non-negative or the angle of G(jω) is within [-π/2, π/2], for the whole range of the frequency ω.”

This means, if the both the inverter output admittance $Y_W(s)$ and the grid impedance $Z_g(s)$ are passive; the system is stable in the right half plane. In other words, the real part of the admittance should be bigger than zero to be stable. Figure 7 illustrates this case.

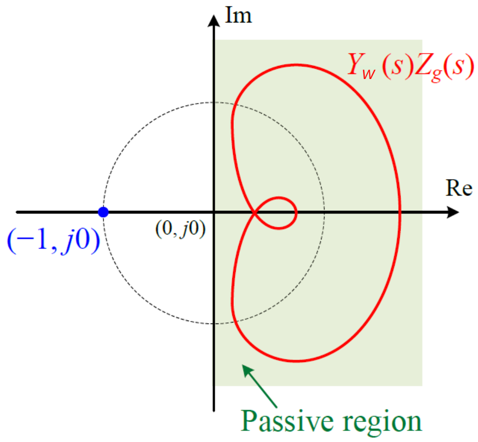

Figure 7: Nyquist plot of a passive system [12]

For a strong grid with a SCR > 3 [32], at a frequency of f = 50 Hz, the product of $Z_g(s) \cdot Y_W(s)$ is always passive, but this behavior may change with harmonics.

On that account, the used models have to be validated to give correct results. In this master thesis, the created simulation model is validated by a field test comparing real world values with simulated ones.

3.2 Modelling of the grid-inverter system

According to Figure 5, the two main components are the grid impedance and the inverter impedance. In this chapter, an analytical model for them is set up and the transformation according to the impedance-based approach is carried out.

The modelling of the grid impedance is based on a passive component, an impedance with real and imaginary parts consisting of an ohmic resistance and inductance in series and capacitance in parallel, see 3.2.5 for the transfer functions.

In a model, an inverter is split into the dc link, the current control loop and the transformation with PLL consideration. The dc link directly influences the current control loop, which in turn affects the calculated values from the transformations. An inverter consists of many non-linear factors such as inverter control dead-time, digital control delay, and phase-locked loop. Neglecting one of those non-linear factors influences the inverter stability substantially. The PLL is further described in 3.2.2 and the delay is modelled in 3.2.4. The dead-time of the switches disregarded in this master thesis.

In Figure 8 the described dependency of the several parts of the grid-inverter system is shown for better understanding. In the green box the transformation is illustrated, which will be described in the 3.2.1 and 3.2.2. In the yellow box the current control is inserted, which will be applied with the transfer functions from 3.2.3. The blue box describes the DC loop, but in this master thesis, the dc link is viewed as a constant source as only minor voltage variations are assumed.

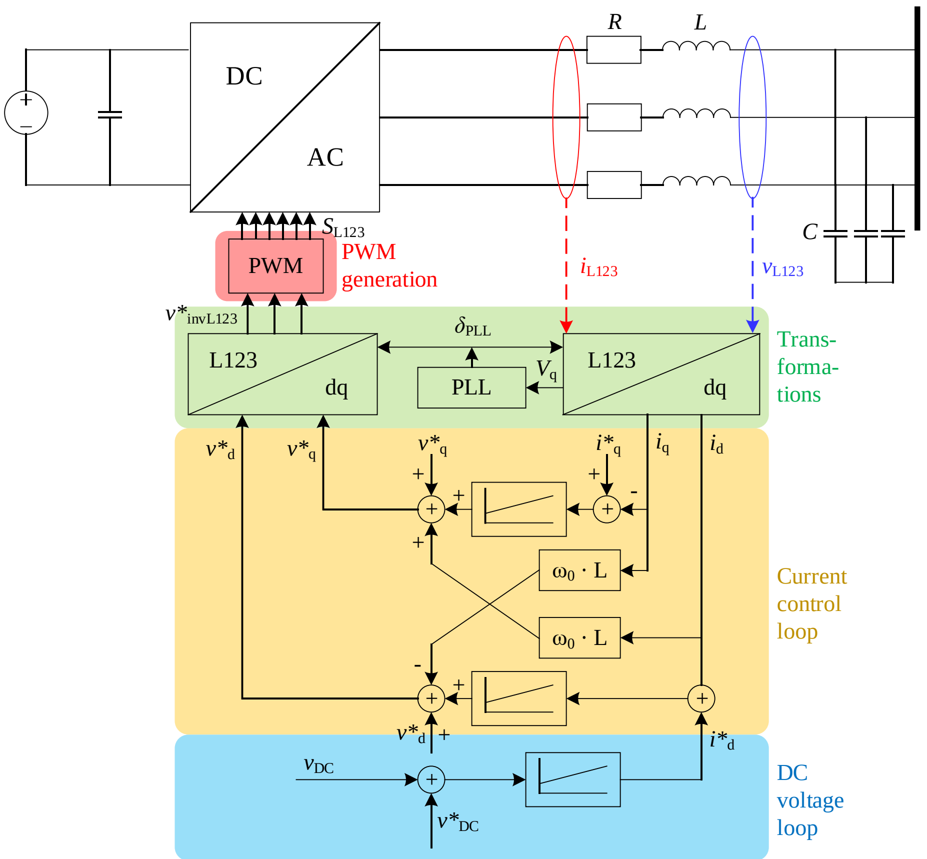

Figure 8: Inverter model [33]

3.2.1 Modelling in dq-rotating coordinate system (dq system)

Originally, the impedance-based approach is first used for DC/DC converters and then further developed to fit into a DC/AC system. Therefore, the original method should be enhanced with linearization techniques. For this process, numerous linearization techniques are possible. Harmonic linearization, modelling by dynamic phasors, reduced order method and the transformation into the dq-frame with the setup of the dq-impedance matrix has already been performed. The advantage of the dq-impedance models is that the harmonic instability as well as the low-frequency oscillations can be analysed, using the GNC. For dq-impedance modelling, the system components need to be transformed in the common dq-frame.

To make the transformation into dq-domain from the measured symmetrical values of a stationary phase coordinate system (abc system) of the sensors, the values are first transformed with the Clark transformation and afterwards further transformed with the Park transformation.

In the abc domain, at least three conductors with alternating voltages or currents are used, which have a 120-degree phase-shift between the phases.

Mathematical it can be written with:

$$\begin{bmatrix} u_a(t) \\ u_b(t) \\ u_c(t) \end{bmatrix} = U_m \cdot \begin{bmatrix} \cos(\omega t + \varphi) \\ \cos(\omega t + \varphi - \frac{2\pi}{3}) \\ \cos(\omega t + \varphi + \frac{2\pi}{3}) \end{bmatrix} \tag{38}$$

Initially these values are transformed into αβ components. This means the three-phase system with a phase shift of 120-degrees between phases becomes a two-phase coordinate system with a phase shift of 90 degrees between the phases fixed to the stator (stationary system). The α-axis describes the real axis and is in phase with phase a of the three-phase system. A transformation matrix is used to calculate the αβ components.

$$\begin{bmatrix} u_\alpha(t) \\ u_\beta(t) \end{bmatrix} = \frac{2}{3} \cdot \begin{bmatrix} 1 & -\frac{1}{2} & -\frac{1}{2} \\ 0 & \frac{\sqrt{3}}{2} & -\frac{\sqrt{3}}{2} \end{bmatrix} \cdot \begin{bmatrix} u_a(t) \\ u_b(t) \\ u_c(t) \end{bmatrix} \tag{39}$$

Then the values are transformed into the dq-domain. In this transformation, the stationary coordinates form a two-phase rotating system with a 90-degree shift. Here a rotation angle between α-axis and d-axis is fit in.

$$\begin{bmatrix} u_d(t) \\ u_q(t) \end{bmatrix} = \begin{bmatrix} \cos(\theta_{PLL}) & \sin(\theta_{PLL}) \\ -\sin(\theta_{PLL}) & \cos(\theta_{PLL}) \end{bmatrix} \cdot \begin{bmatrix} u_\alpha(t) \\ u_\beta(t) \end{bmatrix} \tag{40}$$

Summarised in one equation, the following formula is obtained for the complete transformation from abc to dq components:

$$\begin{bmatrix} u_d(t) \\ u_q(t) \end{bmatrix} = \begin{bmatrix} \cos(\theta_{PLL}) & \sin(\theta_{PLL}) \\ -\sin(\theta_{PLL}) & \cos(\theta_{PLL}) \end{bmatrix} \cdot \frac{2}{3} \cdot \begin{bmatrix} 1 & -\frac{1}{2} & -\frac{1}{2} \\ 0 & \frac{\sqrt{3}}{2} & -\frac{\sqrt{3}}{2} \end{bmatrix} \cdot U_m \cdot \begin{bmatrix} \cos(\omega t + \varphi) \\ \cos\left(\omega t + \varphi - \frac{2\pi}{3}\right) \\ \cos\left(\omega t + \varphi + \frac{2\pi}{3}\right) \end{bmatrix} \tag{41}$$

$$= U_m \cdot \begin{bmatrix} \cos(\omega t + \varphi - \theta_{PLL}) \\ \sin(\omega t + \varphi - \theta_{PLL}) \end{bmatrix} \tag{42}$$

Now the expression $(\omega t + \varphi)$ can be summarised to the angle of the grid (θ_g) and it results for Formula (42) in dq-domain to:

$$\begin{bmatrix} u_d(t) \\ u_q(t) \end{bmatrix} = U_m \cdot \begin{bmatrix} \cos(\theta_g - \theta_{PLL}) \\ \sin(\theta_g - \theta_{PLL}) \end{bmatrix} \tag{43}$$

The angle difference can be described as the error angle between grid and PLL.

$$\theta_\varepsilon = \theta_g - \theta_{PLL} \tag{44}$$

This means, that the each variables is dependent of the angle difference between. Transformed into Laplace –domain this gives the following equation:

$$\begin{bmatrix} u_{d-c} \\ u_{q-c} \end{bmatrix} = U_m \cdot \begin{bmatrix} \cos(\theta_\varepsilon) \\ \sin(\theta_\varepsilon) \end{bmatrix} \tag{45}$$

Now the small signal modelling of this matrix is conducted.

First, the matrix is separately differentiated for d and q component and then linearized at the operating point. At operating point means, that the difference between θ_g and $\theta_{PLL}$is very small. This means mathematically:

$$\theta_g - \theta_{PLL} \ll \quad \begin{cases} \cos(\sim 0) = 1 \\ \sin(\ll) = 1 \end{cases} \tag{46}$$

With that, first Equation (45) is differentiated and then linearized.

$$\begin{gathered} V_{d-c} - \cos(\theta_\varepsilon) \cdot V = 0 \\ \Delta V_{d-c} + (-\cos(\theta_{\varepsilon 0})) \cdot \Delta V + (\sin(\theta_{\varepsilon 0}) \cdot V_0) \cdot \Delta\theta_\varepsilon = 0 \\ \Delta V_{d-c} - \Delta V = 0 \end{gathered} \tag{47}$$

$$\begin{gathered} V_{q-c} - \sin(\theta_\varepsilon) \cdot V = 0 \\ \Delta V_{q-c} + (-\sin(\theta_{\varepsilon 0})) \cdot \Delta V + (\cos(\theta_{\varepsilon 0}) \cdot -V_0) \cdot \Delta\theta_\varepsilon = 0 \\ \Delta V_{q-c} - V_0 \cdot \Delta\theta_\varepsilon = 0 \end{gathered}$$

Now an ideal grid system is assumed without fault conditions. This means that the grid voltage is constant ($\Delta V = 0$) and thus the grid angle is zero ($\theta_g = 0$).

For θ_ε therefore applies:

$$\theta_\varepsilon = -\theta_{PLL} \tag{48}$$

For Formula (47) applies:

$$\begin{aligned} \Delta V_{d-c} &= 0 \\ \Delta V_{q-c} &= -V_0 \cdot \Delta\theta_{PLL} \end{aligned} \tag{49}$$

From this, it can be deduced that the d component in the dq-transformation must always be zero and the q component is influenced by the angle of the PLL.

3.2.2 Hardware modelling

As mentioned at the beginning of this chapter the longitudinal grid impedance is modelled with an ohmic resistor and inductance in series and transversal capacitance. This model gives the following equation in time domain.

$$\begin{gathered} L\frac{d}{d\,t}i_L(t) + R \cdot i_L(t) = U(t) - V_g(t) \\ C\frac{d}{d\,t}u(t) = i_L(t) - i_g(t) \end{gathered} \tag{50}$$

Transferred into Laplace-domain and split into d and q components, this gives two equations.

$$\begin{cases} (L \cdot s + R) \cdot \Delta i_{Ld} - \omega \cdot L \cdot \Delta i_{Lq} = \Delta U_d - \Delta V_{gd} \\ (L \cdot s + R) \cdot \Delta i_{Lq} + \omega \cdot L \cdot \Delta i_{Ld} = \Delta U_q - \Delta V_{gq} \end{cases}$$

$$\begin{cases} C \cdot s \cdot \Delta u_d - \omega \cdot C \cdot \Delta \mathrm{u}_q = \Delta i_{Ld} - \Delta i_{gd} \\ C \cdot s \cdot \Delta u_q + \omega \cdot C \cdot \Delta \mathrm{u}_d = \Delta i_{Lq} - \Delta i_{gq} \end{cases}$$

$$\begin{cases} \Delta i_{Ld} = \dfrac{1}{(L \cdot s + R)} \cdot (\omega \cdot L \cdot \Delta i_{Lq} + \Delta U_d - \Delta V_{gd}) \\ \Delta i_{Lq} = \dfrac{1}{(L \cdot s + R)} \cdot (-\omega \cdot L \cdot \Delta i_{Ld} + \Delta U_q - \Delta V_{gq}) \end{cases} \tag{51}$$

$$\begin{cases} \Delta u_d = \dfrac{1}{C \cdot s} \cdot (\omega \cdot C \cdot \Delta \mathrm{u}_q + \Delta \mathrm{i}_{Ld} - \Delta \mathrm{i}_{gd}) \\ \Delta u_q = \dfrac{1}{C \cdot s} \cdot (-\omega \cdot C \cdot \Delta \mathrm{u}_d + \Delta \mathrm{i}_{Lq} - \Delta \mathrm{i}_{gq}) \end{cases}$$

Lastly, this can be written in matrix-form for the current and the inverter voltage for easier application:

$$\begin{bmatrix}\Delta i_{Ld}\\ \Delta i_{Lq}\end{bmatrix}=\begin{bmatrix}0 & \frac{\omega\cdot L}{(L\cdot s+R)}\\ -\frac{\omega\cdot L}{(L\cdot s+R)} & 0\end{bmatrix}\cdot\begin{bmatrix}\Delta i_{Ld}\\ \Delta i_{Lq}\end{bmatrix}+\frac{1}{(L\cdot s+R)}\cdot\begin{bmatrix}\Delta U_{d}\\ \Delta U_{q}\end{bmatrix}-\frac{1}{(L\cdot s+R)}\cdot\begin{bmatrix}\Delta V_{gd}\\ \Delta V_{gq}\end{bmatrix} \tag{52}$$

$$\begin{bmatrix}\Delta U_{d}\\ \Delta U_{q}\end{bmatrix}=\begin{bmatrix}(L\cdot s+R) & -\omega\cdot L\\ \omega\cdot L & (L\cdot s+R)\end{bmatrix}\cdot\begin{bmatrix}\Delta i_{Ld}\\ \Delta i_{Lq}\end{bmatrix}+\begin{bmatrix}\Delta V_{gd}\\ \Delta V_{gq}\end{bmatrix} \tag{53}$$

The transfer function from the grid voltage to the current is achieved by setting the inverter voltage to zero.

$$\begin{bmatrix}0\\ 0\end{bmatrix}=\begin{bmatrix}(L\cdot s+R) & -\omega\cdot L\\ \omega\cdot L & (L\cdot s+R)\end{bmatrix}\cdot\begin{bmatrix}\Delta i_{Ld}\\ \Delta i_{Lq}\end{bmatrix}+\begin{bmatrix}\Delta V_{gd}\\ \Delta V_{gq}\end{bmatrix} \tag{54}$$

$$G_{V-I}=\begin{bmatrix}-\frac{(L\cdot s+R)}{L^2\cdot s^2+2\cdot L\cdot R\cdot s+L^2\cdot\omega^2+R^2} & -\frac{(L\cdot\omega)}{L^2\cdot s^2+2\cdot L\cdot R\cdot s+L^2\cdot\omega^2+R^2}\\ \frac{(L\cdot\omega)}{L^2\cdot s^2+2\cdot L\cdot R\cdot s+L^2\cdot\omega^2+R^2} & -\frac{(L\cdot s+R)}{L^2\cdot s^2+2\cdot L\cdot R\cdot s+L^2\cdot\omega^2+R^2}\end{bmatrix} \tag{55}$$

The transfer function from the inverter voltage to the current is achieved by setting the grid voltage to zero.

$$\begin{bmatrix}\Delta U_{d}\\ \Delta U_{q}\end{bmatrix}=\begin{bmatrix}(L\cdot s+R) & -\omega\cdot L\\ \omega\cdot L & (L\cdot s+R)\end{bmatrix}\cdot\begin{bmatrix}\Delta i_{Ld}\\ \Delta i_{Lq}\end{bmatrix}+\begin{bmatrix}0\\ 0\end{bmatrix}$$

$$G_{U-I}=\begin{bmatrix}\frac{(L\cdot s+R)}{L^2\cdot s^2+2\cdot L\cdot R\cdot s+L^2\cdot\omega^2+R^2} & \frac{(L\cdot\omega)}{L^2\cdot s^2+2\cdot L\cdot R\cdot s+L^2\cdot\omega^2+R^2}\\ -\frac{(L\cdot\omega)}{L^2\cdot s^2+2\cdot L\cdot R\cdot s+L^2\cdot\omega^2+R^2} & \frac{(L\cdot s+R)}{L^2\cdot s^2+2\cdot L\cdot R\cdot s+L^2\cdot\omega^2+R^2}\end{bmatrix} \tag{56}$$

3.2.3 Small signal modelling of phase locked loop

With the linearization, only a small error between grid and angle to the dq-domain is assumed. Therefore, the synchronisation between controller variables and measured variables must be very good.

However, as soon as a controller is installed in a system and the measured variables should be influenced by calculated ones via a feedback loop, there is a difference between system variables and controller variables due to a time delay.

Therefore, the values of the controller and system are not synchronised affecting the phase angle and calculations. An easy solution is the usage of a phase locked loop (PLL). As the name indicates, the PLL locks onto the input signal and compares this signal to the internal periodic signal, while it adjusts the internal oscillator to keep the phases matched. Consequently, the input and output frequencies are the same and the values now synchronised [34].

The only task of the PLL is to record the phase of the incoming signal and follow it. This requires three central components: a phase comparator, a loop filter with controller (PI controller) and integrator and the feedback loop [34]. Accordingly, the control circuit of the PLL can be created.

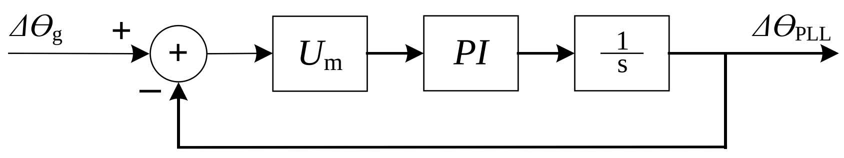

Figure 9: SSM of PLL

The transfer function of the PLL alone results in:

$$G_{PLL}(s) = \left(K_{p,PLL} + \frac{K_{i,PLL}}{s}\right) \tag{57}$$

From Figure 9 the corresponding transfer function for the PLL can be derived:

$$\Delta\theta_{PLL} = (\Delta\theta_g - \Delta\theta_{PLL}) \cdot U_m \cdot G_{PLL} \cdot \frac{1}{s} \tag{58}$$

The feedback loop of the PLL is always the q-component of the grid voltage, which transforms Formula (58) further.

$$\Delta\theta_{PLL} = -\Delta V_{q-c} \cdot G_{PLL} \cdot \frac{1}{s} \tag{59}$$

If $\theta_\varepsilon = -\theta_{PLL}$ is considered again, it follows:

$$\Delta\theta_\varepsilon = \Delta V_{q-c} \cdot G_{PLL} \cdot \frac{1}{s} \tag{60}$$

Lastly, this can be written in matrix-form for easier application:

$$\Delta\theta_\varepsilon = \begin{bmatrix} 0 & G_{PLL} \cdot \frac{1}{s} \\ 0 & G_{PLL} \cdot \frac{1}{s} \end{bmatrix} \cdot \begin{bmatrix} \Delta V_{d-c} \\ \Delta V_{q-c} \end{bmatrix} \tag{61}$$

With this contemplation, two models can be created. One model without consideration of the PLL and one model with implementation of the PLL.

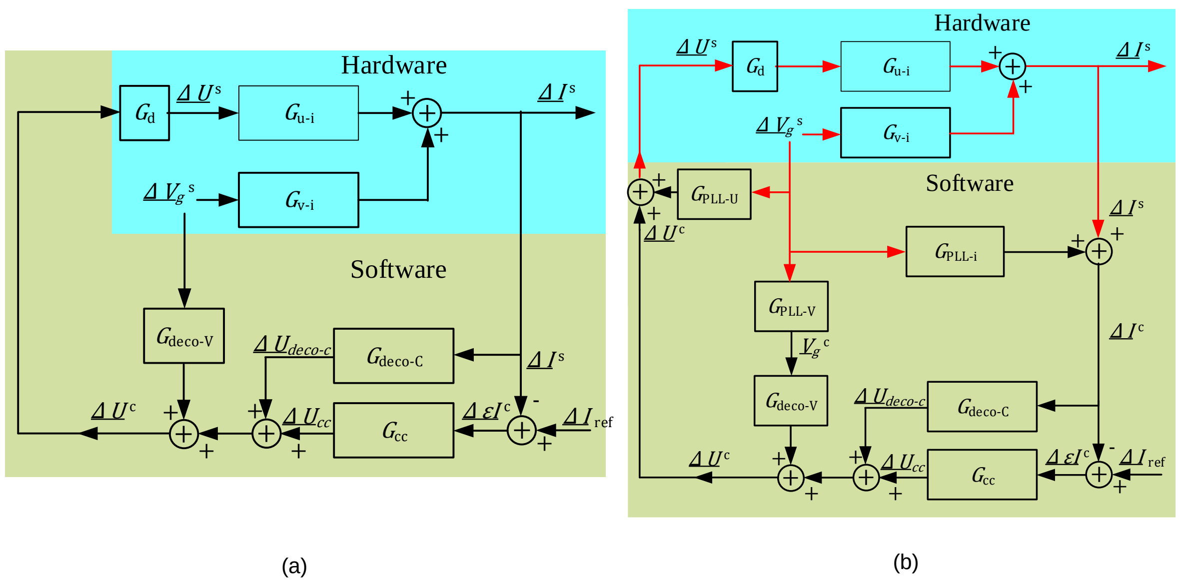

Figure 10: Control circuit of SSM model: (a) without PLL (b): with PLL

In *Figure 10*, the underline means that the variable is a vector and consists of a d and q component.

The difference between the circuit without PLL and with PLL is the consideration of the angel difference between the controller variables and the system variables. In the model with PLL, this angel difference is regarded with the addition of separate PLL transfer functions. There are three transitions between system and controller hence three different transfer functions according to the transition relation between hardware and controller variables are put into the model.

The transition relation is built on the voltage and current relationship and their interjacent phase angle.

In this phasor diagram, the voltage and current are displayed in dq-components and all needed angles of hardware and software components included.

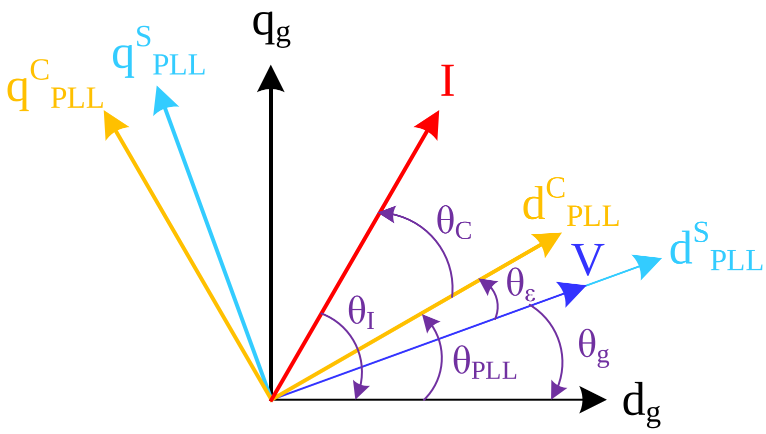

Figure 11: PLL phasor diagram

In the phasor diagram, the black coloured d and q-axis display the dq-domain of the grid, the bright blue coloured axis the dq-domain of the PLL from the system. Here already the angle difference between grid angle and PLL is inserted with θ_g. Then the PLL-axis of the system is transformed into the controller part and another error angle, as described before, is inserted with θ_ε. Then the voltage and the current phasors are inserted. Here the voltage is in phase with the d-axis of the PLL from the system. The current phasor is arbitrarily inserted and finally the angles between the phasors included.

With PLL usage two angle relations are derived; one for the current and one for the voltage.

$$\text{Voltage: } \theta_\varepsilon = \theta_g - \theta_{PLL}$$
$$\text{Current: } \theta_c = \theta_I - \theta_{PLL} \qquad (62)$$

From those relations the separate PLL transfer functions accordingly to the relationship with the model can be set up.

Transformation V_g^S to V_g^C:

The error angle of the voltage is represented by θ_ε. Since the PLL is a non-linear system, the transformation from system to controller variables is performed with a sine and cosine-matrix.

$$\begin{bmatrix} V_{d-c} \\ V_{q-c} \end{bmatrix} = \begin{bmatrix} \cos(\theta_\varepsilon) & \sin(\theta_\varepsilon) \\ -\sin(\theta_\varepsilon) & \cos(\theta_\varepsilon) \end{bmatrix} \cdot \begin{bmatrix} V_{d-s} \\ V_{q-s} \end{bmatrix} \tag{63}$$

Now the small signal modelling of this matrix is conducted.

First, the matrix is separately differentiated for d and q component and then linearized at the operating point.

$$\begin{gathered} V_{d-c} - \cos(\theta_\varepsilon) \cdot V_{d-s} - \sin(\theta_\varepsilon) \cdot V_{q-s} = 0 \\ \Delta V_{d-c} + (-\cos(\theta_{\varepsilon 0})) \cdot \Delta V_{d-s} + (-\sin(\theta_{\varepsilon 0})) \cdot \Delta V_{q-s} + (\sin(\theta_{\varepsilon 0}) \cdot V_{d-s0} - \cos(\theta_{\varepsilon 0}) \cdot V_{q-s0}) \cdot \Delta\theta_\varepsilon = 0 \\ \Delta V_{d-c} - \Delta V_{d-s} + V_{q-s0} \cdot \Delta\theta_\varepsilon = 0 \\ V_{q-c} + \sin(\theta_\varepsilon) \cdot V_{d-s} - \cos(\theta_\varepsilon) \cdot V_{q-s} = 0 \\ \Delta V_{q-c} + (\sin(\theta_{\varepsilon 0})) \cdot \Delta V_{d-s} + (-\cos(\theta_{\varepsilon 0})) \cdot \Delta V_{q-s} + (\cos(\theta_{\varepsilon 0}) \cdot V_{d-s0} + \sin(\theta_{\varepsilon 0}) \cdot V_{q-s0}) \cdot \Delta\theta_\varepsilon = 0 \\ \Delta V_{q-c} - \Delta V_{q-s} + V_{d-s0} \cdot \Delta\theta_\varepsilon = 0 \end{gathered} \tag{64}$$

Finally, the transformation matrix is build.

$$\begin{bmatrix} \Delta V_{d-c} \\ \Delta V_{q-c} \end{bmatrix} = \begin{bmatrix} V_{q-s0} \\ -V_{d-s0} \end{bmatrix} \cdot \Delta\theta_\varepsilon + \begin{bmatrix} \Delta V_{d-s} \\ \Delta V_{q-s} \end{bmatrix} \tag{65}$$

Transformation I^S to I^C:

For this transformation, the whole process is repeated. The error angle of the voltage is represented by θ_c. Since the PLL is a non-linear system, the transformation from system to controller variables is performed with a sine and cosine-matrix.

$$\begin{bmatrix} I_{d-c} \\ I_{q-c} \end{bmatrix} = \begin{bmatrix} \cos(\theta_c) & \sin(\theta_c) \\ -\sin(\theta_c) & \cos(\theta_c) \end{bmatrix} \cdot \begin{bmatrix} I_{d-s} \\ I_{q-s} \end{bmatrix} \tag{66}$$

Now the small signal modelling of this matrix is conducted.

First, the matrix is separately differentiated for d and q component and then linearized at the operating point.

$$\begin{gathered} I_{d-c} - \cos(\theta_c) \cdot I_{d-s} - \sin(\theta_c) \cdot I_{q-s} = 0 \\ \Delta I_{d-c} + (-\cos(\theta_{c0})) \cdot \Delta I_{d-s} + (-\sin(\theta_{c0})) \cdot \Delta I_{q-s} + (\sin(\theta_{c0}) \cdot I_{d-s0} - \cos(\theta_{c0}) \cdot I_{q-s0}) \cdot \Delta\theta_c = 0 \\ \Delta I_{d-c} - \Delta I_{d-s} + I_{q-s0} \cdot \Delta\theta_c = 0 \\ \\ I_{q-c} + \sin(\theta_c) \cdot I_{d-s} - \cos(\theta_c) \cdot I_{q-s} = 0 \\ \Delta I_{q-c} + (\sin(\theta_{c0})) \cdot \Delta I_{d-s} + (-\cos(\theta_{c0})) \cdot \Delta I_{q-s} + (\cos(\theta_{c0}) \cdot I_{d-s0} + \sin(\theta_{c0}) \cdot I_{q-s0}) \cdot \Delta\theta_c = 0 \\ \Delta I_{q-c} - \Delta I_{q-s} + I_{d-s0} \cdot \Delta\theta_c = 0 \end{gathered} \tag{67}$$

Finally, the transformation matrix is build.

$$\begin{bmatrix}\Delta I_{d-c}\\ \Delta I_{q-c}\end{bmatrix} = \begin{bmatrix} I_{q-s0}\\ -I_{d-s0}\end{bmatrix} \cdot \Delta\theta_c + \begin{bmatrix}\Delta I_{d-s}\\ \Delta I_{q-s}\end{bmatrix} \tag{68}$$

<u>Transformation U^C to U^S:</u>

For this transformation, the direction is in the other direction. Therefore, the first matrix has to be inverted. The error angle of the voltage is represented by θ_ε. Since the PLL is a non-linear system, the transformation from system to controller variables is performed with a sine and cosine-matrix.

$$\begin{bmatrix}U_{d-c}\\ U_{q-c}\end{bmatrix} = \begin{bmatrix}\cos(\theta_\varepsilon) & \sin(\theta_\varepsilon)\\ -\sin(\theta_\varepsilon) & \cos(\theta_\varepsilon)\end{bmatrix} \cdot \begin{bmatrix}U_{d-s}\\ U_{q-s}\end{bmatrix} \tag{69}$$

Now the matrix is inverted to display the relation from the system variables to the controller values.

$$\begin{bmatrix}U_{d-s}\\ U_{q-s}\end{bmatrix} = \begin{bmatrix}\cos(\theta_\varepsilon) & -\sin(\theta_\varepsilon)\\ \sin(\theta_\varepsilon) & \cos(\theta_\varepsilon)\end{bmatrix} \cdot \begin{bmatrix}U_{d-c}\\ U_{q-c}\end{bmatrix} \tag{70}$$

Now the small signal modelling of this matrix is conducted.

First, the matrix is separately differentiated for d and q component and then linearized at the operating point.

$$\begin{gathered} U_{d-s} - \cos(\theta_\varepsilon)\cdot U_{d-c} + \sin(\theta_\varepsilon)\cdot U_{q-c} = 0\\ \Delta U_{d-s} + (-\cos(\theta_{\varepsilon 0}))\cdot \Delta V_{d-c} + (\sin(\theta_{\varepsilon 0}))\cdot \Delta U_{q-c} + (\sin(\theta_{\varepsilon 0})\cdot U_{d-c0} + \cos(\theta_{\varepsilon 0})\cdot U_{q-c0})\cdot \Delta\theta_\varepsilon = 0\\ \Delta U_{d-s} - \Delta U_{d-c} + U_{q-c0}\cdot\Delta\theta_\varepsilon = 0\\ \\ U_{q-s} - \sin(\theta_\varepsilon)\cdot U_{d-c} - \cos(\theta_\varepsilon)\cdot U_{q-c} = 0\\ \Delta V_{q-s} + (-\sin(\theta_{\varepsilon 0}))\cdot \Delta U_{d-c} + (-\cos(\theta_{\varepsilon 0}))\cdot \Delta U_{q-c} + (-\cos(\theta_{\varepsilon 0})\cdot U_{d-c0} + \sin(\theta_{\varepsilon 0})\cdot U_{q-c0})\cdot \Delta\theta_\varepsilon = 0\\ \Delta U_{q-s} - \Delta U_{q-c} + U_{d-c0}\cdot\Delta\theta_\varepsilon = 0 \end{gathered} \tag{71}$$

Finally, the transformation matrix is build.

$$\begin{bmatrix}\Delta U_{d-s}\\ \Delta U_{q-s}\end{bmatrix} = \begin{bmatrix} -U_{q-s0}\\ U_{d-s0}\end{bmatrix} \cdot \Delta\theta_\varepsilon + \begin{bmatrix}\Delta U_{d-c}\\ \Delta U_{q-c}\end{bmatrix} \tag{72}$$

After all three transfer functions have been set up; Formula (105) can be used.

<u>Transformation V_g^S to V_g^C:</u>

$$\begin{bmatrix}\Delta V_{d-c}\\ \Delta V_{q-c}\end{bmatrix} = \begin{bmatrix} V_{q-s0}\\ -V_{d-s0}\end{bmatrix} \cdot \begin{bmatrix} 0 & G_{PLL}\cdot\frac{1}{s}\\ 0 & G_{PLL}\cdot\frac{1}{s}\end{bmatrix} \cdot \begin{bmatrix}\Delta V_{d-c}\\ \Delta V_{q-c}\end{bmatrix} + \begin{bmatrix}\Delta V_{d-s}\\ \Delta V_{q-s}\end{bmatrix} \tag{73}$$

$$\begin{bmatrix}\Delta V_{d-s}\\ \Delta V_{q-s}\end{bmatrix}=\begin{bmatrix}1 & -G_{PLL}\cdot\frac{1}{s}\cdot V_{q-s0}\\ 0 & 1+G_{PLL}\cdot\frac{1}{s}\cdot V_{d-s0}\end{bmatrix}\cdot\begin{bmatrix}\Delta V_{d-c}\\ \Delta V_{q-c}\end{bmatrix}$$

To achieve the relationship from system to controller variables the matrix has to be inverted. The final transfer function for the relationship between V_g^S to V_g^C is:

$$G_{PLL-V}=\begin{bmatrix}1 & \frac{V_{q-s0}\cdot G_{PLL}}{G_{PLL}\cdot V_{d-s0}+s}\\ 0 & \frac{s}{G_{PLL}\cdot V_{d-s0}+s}\end{bmatrix}\tag{74}$$

Transformation I^S to I^C:

$$\begin{aligned}\begin{bmatrix}\Delta I_{d-c}\\ \Delta I_{q-c}\end{bmatrix}&=\begin{bmatrix}I_{q-s0}\\ -I_{d-s0}\end{bmatrix}\cdot\begin{bmatrix}0 & G_{PLL}\cdot\frac{1}{s}\\ 0 & G_{PLL}\cdot\frac{1}{s}\end{bmatrix}\cdot\begin{bmatrix}\Delta V_{d-c}\\ \Delta V_{q-c}\end{bmatrix}+\begin{bmatrix}\Delta I_{d-s}\\ \Delta I_{q-s}\end{bmatrix}\\ \begin{bmatrix}\Delta I_{d-c}\\ \Delta I_{q-c}\end{bmatrix}&=\begin{bmatrix}I_{q-s0}\cdot G_{PLL}\cdot\frac{1}{s}\cdot\Delta V_{q-c}\\ -I_{d-s0}\cdot G_{PLL}\cdot\frac{1}{s}\cdot\Delta V_{q-c}\end{bmatrix}+\begin{bmatrix}\Delta I_{d-s}\\ \Delta I_{q-s}\end{bmatrix}\end{aligned}\tag{75}$$

According to

Figure 10, however, the current does not start at ΔV_{q-c} but at ΔV_{q-s}. Therefore, the relation from Formula (73) is used but solved for ΔV_{q-s}.

$$\Delta V_{q-c}=\frac{\Delta V_{q-s}\cdot s}{G_{PLL}\cdot V_{d-s0}+s}\tag{76}$$

Formula (76) is inserted into formula (75) and the final matrix is obtained from which the transfer function is derived.

$$\begin{bmatrix}\Delta I_{d-c}\\ \Delta I_{q-c}\end{bmatrix}=\begin{bmatrix}0 & \frac{\mathrm{I}_{q-s0}\cdot G_{PLL}}{G_{PLL}\cdot V_{d-s0}+s}\\ 0 & -\frac{\mathrm{I}_{d-s0}\cdot G_{PLL}}{G_{PLL}\cdot V_{d-s0}+s}\end{bmatrix}+\begin{bmatrix}\Delta I_{d-s}\\ \Delta I_{q-s}\end{bmatrix}\tag{77}$$

With the transfer function for the current:

$$G_{PLL-I}=\begin{bmatrix}0 & \frac{I_{q-s0}\cdot G_{PLL}}{G_{PLL}\cdot V_{d-s0}+s}\\ 0 & -\frac{I_{d-s0}\cdot G_{PLL}}{G_{PLL}\cdot V_{d-s0}+s}\end{bmatrix}\tag{78}$$

Transformation U^C to U^S:

$$\begin{bmatrix}\Delta U_{d-s}\\ \Delta U_{q-s}\end{bmatrix}=\begin{bmatrix}-U_{q-s0}\\ U_{d-s0}\end{bmatrix}\cdot\begin{bmatrix}0 & G_{PLL}\cdot\frac{1}{s}\\ 0 & G_{PLL}\cdot\frac{1}{s}\end{bmatrix}\cdot\begin{bmatrix}\Delta V_{d-c}\\ \Delta V_{q-c}\end{bmatrix}+\begin{bmatrix}\Delta U_{d-c}\\ \Delta U_{q-c}\end{bmatrix}\tag{79}$$

$$\begin{bmatrix}\Delta U_{d-c}\\ \Delta U_{q-c}\end{bmatrix} = \begin{bmatrix}-U_{q-s0}\cdot G_{PLL}\cdot\frac{1}{s}\cdot\Delta V_{q-c}\\ U_{d-s0}\cdot G_{PLL}\cdot\frac{1}{s}\cdot\Delta V_{q-c}\end{bmatrix} + \begin{bmatrix}\Delta U_{d-c}\\ \Delta U_{q-c}\end{bmatrix}$$

According to *Figure 10*, however, also this voltage does not start at ΔV_{q-c} but at ΔV_{q-s}. Therefore, the relation from Formula (73) is used but solved for ΔV_{q-s} and gives Formula (76). This is now put into Formula (79) and the final matrix is obtained from which the transfer function is derived.

$$\begin{bmatrix}\Delta U_{d-c}\\ \Delta U_{q-c}\end{bmatrix} = \begin{bmatrix}\Delta U_{d-s}\\ \Delta U_{q-s}\end{bmatrix} - \begin{bmatrix}0 & -\frac{U_{q-s0}\cdot G_{PLL}}{G_{PLL}\cdot V_{d-s0}+s}\\ 0 & \frac{U_{d-s0}\cdot G_{PLL}}{G_{PLL}\cdot V_{d-s0}+s}\end{bmatrix}\cdot\begin{bmatrix}\Delta V_{d-s}\\ \Delta V_{q-s}\end{bmatrix} \tag{80}$$

With the transfer function for the voltage:

$$G_{PLL-U} = \begin{bmatrix}0 & -\frac{U_{q-s0}\cdot G_{PLL}}{G_{PLL}\cdot V_{d-s0}+s}\\ 0 & \frac{U_{d-s0}\cdot G_{PLL}}{G_{PLL}\cdot V_{d-s0}+s}\end{bmatrix} \tag{81}$$

3.2.4 Current control loop transfer function

The current control loop consists of a PI controller, has a feedback loop where from the reference value the measured d, and q current of the system variables is subtracted.

This gives the following relation and subsequently the transfer function.

$$\begin{bmatrix}\Delta U_{cc-d}\\ \Delta U_{cc-q}\end{bmatrix} = \begin{bmatrix}k_{pc}+\frac{k_{ic}}{s} & 0\\ 0 & k_{pc}+\frac{k_{ic}}{s}\end{bmatrix}\cdot\left(\begin{bmatrix}\Delta I_{dref}\\ \Delta I_{qref}\end{bmatrix} - \begin{bmatrix}\Delta I_{ds}\\ \Delta I_{qs}\end{bmatrix}\right) \tag{82}$$

$$G_{cc} = \begin{bmatrix}k_{pc}+\frac{k_{ic}}{s} & 0\\ 0 & k_{pc}+\frac{k_{ic}}{s}\end{bmatrix} \tag{83}$$

3.2.5 Modelling of delay unit

Due to the time delay required for the measured values to arrive at the controller and the next values to be calculated, a delay should be included. A good way to implement a delay is with the Padé approximation. Depending on the order of the used Padé approximation, the accuracy of the whole system can increase.

In the master thesis the Padé approximation with order, one is used. The delay is inserted once in the final schematic circuit. The position is at the transition between controller values and hardware values.

The transfer function of the Padé approximation with first order is derived from the Padé table:

$$G_d = \begin{bmatrix} \frac{2 - s \cdot t_s}{2 + s \cdot t_s} & 0 \\ 0 & \frac{2 - s \cdot t_s}{2 + s \cdot t_s} \end{bmatrix} \tag{84}$$

In Formula (84) t_s is the sampling rate and can be changed to simulate different time delays. When modelled with a zero-order hold block, for the consideration of pulse with modulation (PWM) 0.5 t_s are introduced additionally. Then with a one-period calculation delay of the digital controller 1.5 t_s are a typical value [35].

3.2.6 Decoupling transfer functions

Two transfer functions are still missing, which are decoupling the d from the q component during the transformation.

The first one is the decoupling transfer function of the current control loop. From the voltage to current relation, the transfer function follows.

$$\begin{bmatrix} U_{deco-c-d} \\ U_{deco-c-q} \end{bmatrix} = \begin{bmatrix} 0 & -\omega \cdot L \\ \omega \cdot L & 0 \end{bmatrix} \cdot \begin{bmatrix} I_d \\ I_q \end{bmatrix} \tag{85}$$

$$G_{deco-c} = \begin{bmatrix} 0 & -\omega \cdot L \\ \omega \cdot L & 0 \end{bmatrix} \tag{86}$$

The second one is the decoupling transfer function of the grid voltage. From the voltage to current relation, the transfer function follows.

$$\begin{bmatrix} V_{deco-V-d} \\ V_{deco-V-q} \end{bmatrix} = \begin{bmatrix} 1 & 0 \\ 0 & 1 \end{bmatrix} \cdot \begin{bmatrix} V_d \\ V_q \end{bmatrix} \tag{87}$$

$$G_{deco-V} = \begin{bmatrix} 1 & 0 \\ 0 & 1 \end{bmatrix} \tag{88}$$

3.3 Transfer function of inverter

According to *Figure 10*, all the transfer functions for the model without and with PLL are set up. Based on the control circuits the equations on hardware and software side can be described

Model without PLL:

The left picture of *Figure 10* is used to get the hardware and software equation of the model.

Hardware: $$\underline{\Delta I_s} = G_{U-I} \cdot \underline{\Delta U_S} + G_{V-I} \cdot \underline{\Delta V_g} \tag{89}$$

Software: $$\underline{\Delta U_s} = G_d \cdot \underline{\Delta U_C} \tag{90}$$

$$\underline{\Delta U_C} = G_{deco-V} \cdot \underline{\Delta V_g} + \underline{\Delta I_S} \cdot G_{deco-c} + (\underline{\Delta I_{ref}} - \underline{\Delta I_S}) \cdot G_{cc}$$

Formula (89) is inserted into Formula (90) and the general equation based on Figure 5 finally built.

In a small signal model, the final equation has this shape:

$$\underline{\Delta I_S} = G_{ctr} \cdot \underline{\Delta I_{\mathrm{ref}}} + Y \cdot \underline{\Delta V_g} \tag{91}$$

With Formula (89), (90) and all the transfer functions, the equation is as follow:

$$\begin{aligned}\underline{\Delta I_S} = &-\frac{G_{cc} \cdot G_d \cdot G_{U-I}}{-G_{cc} \cdot G_d \cdot G_{U-I} + G_d \cdot G_{deco-c} \cdot G_{U-I} - 1} \cdot \underline{\Delta I_{ref}} \\ &-\frac{G_d \cdot G_{U-I} \cdot G_{deco-V} + G_{V-I}}{-G_{cc} \cdot G_d \cdot G_{U-I} + G_d \cdot G_{deco-c} \cdot G_{U-I} - 1} \cdot \underline{\Delta V_g}\end{aligned} \tag{92}$$

Accordingly, with regard to the definition of the current direction *Y* results in:

$$Y = \frac{G_d \cdot G_{U-I} \cdot G_{deco-V} + G_{V-I}}{-G_{cc} \cdot G_d \cdot G_{U-I} + G_d \cdot G_{deco-c} \cdot G_{U-I} - 1} \tag{93}$$

The value for ΔI_{ref} remains constant in the considerations of this master's thesis, whereby this part is omitted from the equation.

Model with PLL:

The right picture of *Figure 10* is used to get the hardware and software equation of the model.

Hardware:
$$\underline{\Delta I_s} = G_{U-I} \cdot \underline{\Delta U_S} + G_{V-I} \cdot \underline{\Delta V_g} \tag{94}$$

Software:
$$\underline{\Delta U_s} = G_d \cdot (\underline{\Delta V_g} \cdot G_{PLL-U} + \underline{\Delta U_C}) \tag{95}$$

$$\begin{aligned}\underline{\Delta U_C} = &G_{deco-V} \cdot G_{PLL-V} \cdot \underline{\Delta V_g} + \left(\underline{\Delta I_S} + G_{PLL-I} \cdot \underline{\Delta V_g}\right) \cdot G_{deco-c} + (\underline{\Delta I_{ref}} \\ &- \left(\underline{\Delta I_S} + G_{PLL-I} \cdot \underline{\Delta V_g}\right)) \cdot G_{cc}\end{aligned}$$

Formula (94) is inserted into Formula (95) and the general equation based on Figure 5 finally built.

In a small signal model, the final equation has this shape:

$$\underline{\Delta I_S} = G_{ctr} \cdot \underline{\Delta I_{\mathrm{ref}}} + Y \cdot \underline{\Delta V_g} \tag{96}$$

With Formula (94), (95) and all the transfer functions, the equation is as follow:

$$\begin{aligned}\underline{\Delta I_S} = &-\frac{G_{cc} \cdot G_d \cdot G_{U-I}}{-G_{cc} \cdot G_d \cdot G_{U-I} + G_d \cdot G_{deco-c} \cdot G_{U-I} - 1} \cdot \underline{\Delta I_{ref}} \\ &-\frac{G_d \cdot G_{U-I}(-G_{cc} \cdot G_{PLL-I} + G_{deco-c} \cdot G_{PLL-I} + G_{deco-V} \cdot G_{PLL-V} + G_{PLL-U}) + G_{V-I}}{-G_{cc} \cdot G_d \cdot G_{U-I} + G_d \cdot G_{deco-c} \cdot G_{U-I} - 1} \cdot \underline{\Delta V_g}\end{aligned} \tag{97}$$

Accordingly, with regard to the definition of the current direction *Y* results in:

$$Y = \frac{G_d \cdot G_{U-I}(-G_{cc} \cdot G_{PLL-I} + G_{deco-c} \cdot G_{PLL-I} + G_{deco-V} \cdot G_{PLL-V} + G_{PLL-U}) + G_{V-I}}{-G_{cc} \cdot G_d \cdot G_{U-I} + G_d \cdot G_{deco-c} \cdot G_{U-I} - 1} \tag{98}$$

The value for ΔI_{ref} remains constant in the considerations of this master's thesis, whereby this part is omitted from the equation. Since photovoltaic as a source does not change its voltage generation rapidly and the target time constant is smaller than 1 second, it can be represented by a constant DC source.

3.4 Investigation of modelling results

Now the analytical model with modelling of the PLL and without modelling of the PLL can be compared with each other. The simulation model of the photovoltaic system can then be checked against the analytical models.

In order to test the behaviour of the analytical models, the parameter *s* is changed in the Laplace-domain.

$$s = j \cdot 2\pi \cdot f \tag{99}$$

With the change of the frequency over a defined frequency range, the Laplace operator *s* is changed and thus the transfer functions from the previous section. This makes it very easy to test the behaviour of the models over a wide frequency range, which is similar to the frequency sweep in the next chapter. The frequency range from 150 to 5000 Hz is examined.

By inserting the transfer functions from point 3.2, the admittance and the real part of the impedance of the models can be illustrated.

3.4.1 Comparison between model with and without PLL

In the next diagram, the impedance of the analytical model without PLL is shown in red as a function of the frequency, and the analytical model with PLL is shown in blue. As can be seen, there are mainly differences of the PLL effect on the qq-component, the dq-component and small ones on the qd-component. From the curve, it is clear that the impedance with PLL is much lower at lower frequencies than the transfer function without PLL. At higher frequencies, however, it adapts to the curve without PLL.

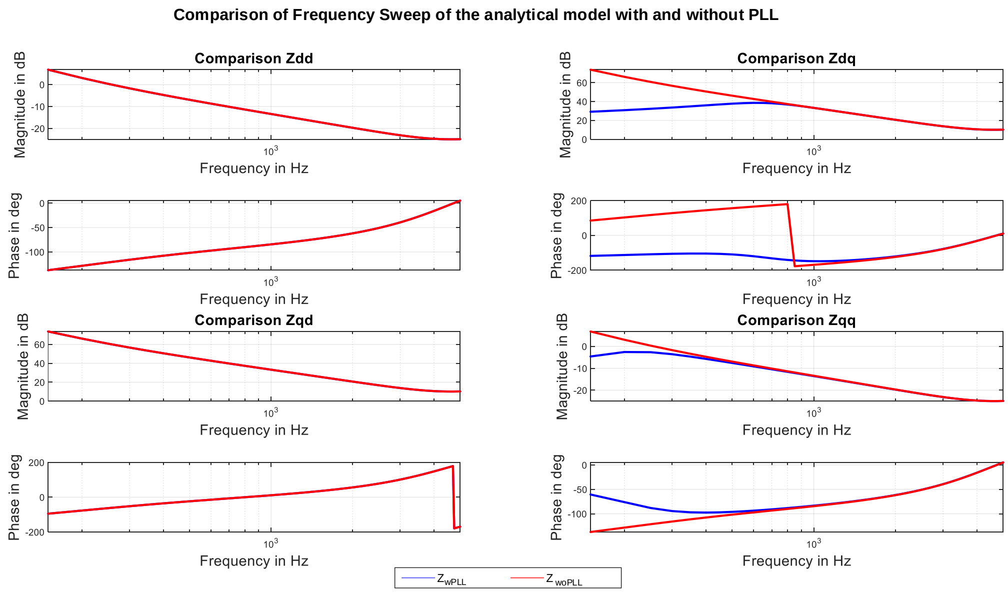

Figure 12: Analytical model comparison impedance result

Due to the lower impedance in the previous diagram, the real part of the admittance of the curve with PLL, again in blue, is higher than that of the red curve without PLL. This corresponds to a higher stability of the system according to the stability criterion. From this comparison, it can be observed that there is a clear difference between the model with and without PLL and that it is important to pay attention to the PLL.

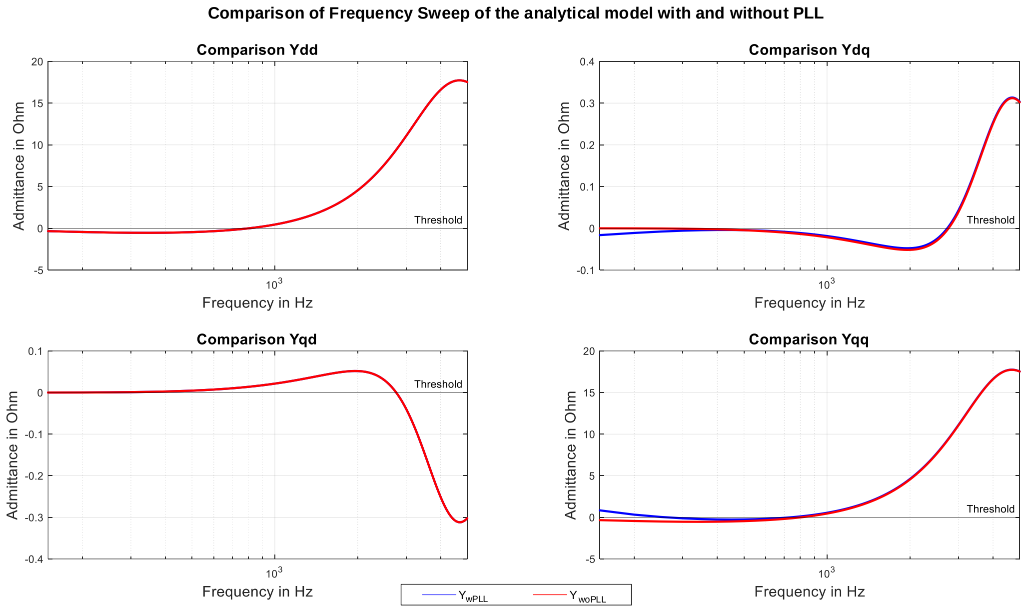

Figure 13: Analytical model comparison real part of admittance result

3.4.2 Model with PLL with different Padè orders

Since, according to the literature, the control delay plays a role especially at higher frequencies, the analytical model is also tested with higher-order Padè function. The following diagram shows the comparison between the normal model with first-order Padè in the curve with the solid blue line and the second, third and fourth order with the dashed lines. The functions of the second and fourth order are almost congruent. The phenomenon described in the literature clearly occurs - the curves are equivalent up to about 1000 Hz and differ thereafter.

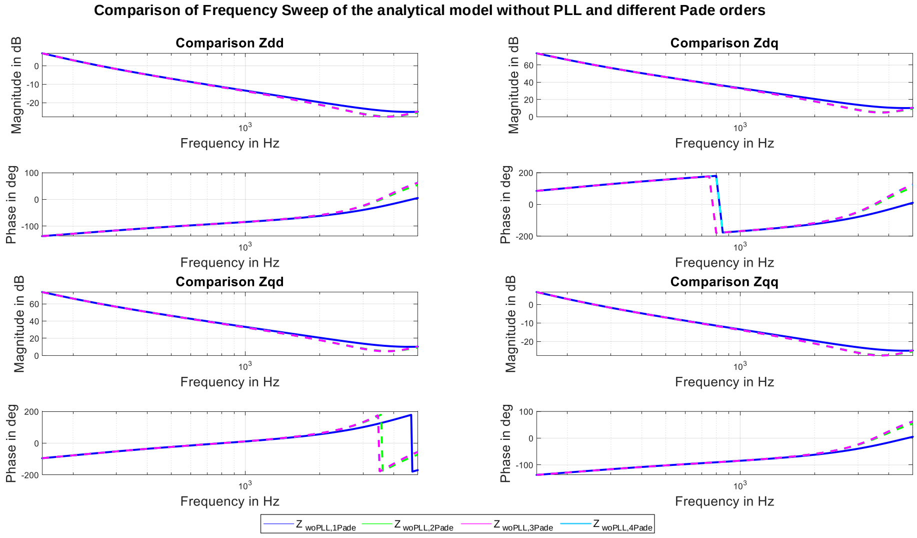

Figure 14: Analytical model with PLL impedance result different Padè orders

The amplitude level of the real part also changes accordingly. The amplitude is much higher at the higher frequencies compared to the first Padè order.

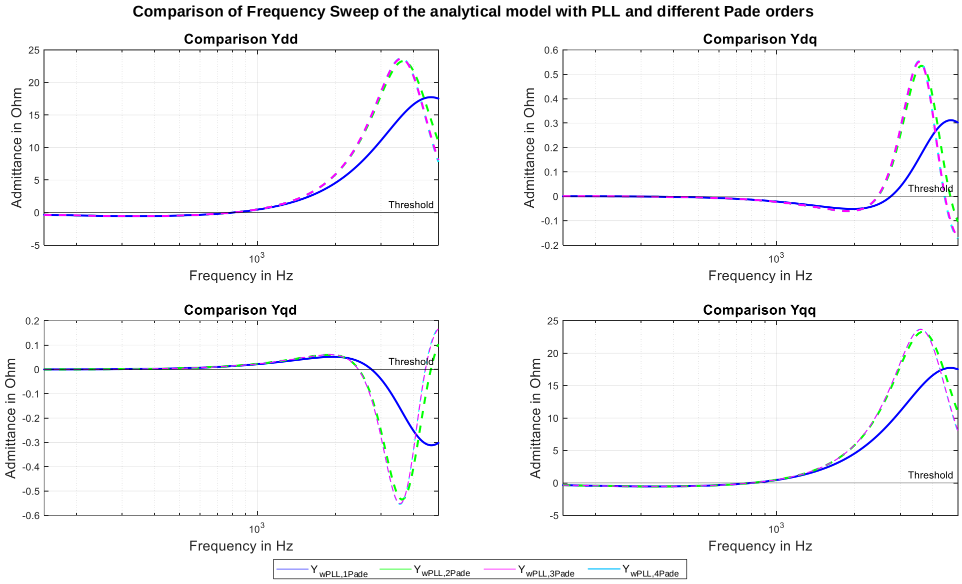

Figure 15: Analytical model with PLL real part of admittance result different Padè orders

The same behaviour is detected in the models without PLL.

3.4.3 Comparison between analytical models and photovoltaic model

In this diagram, the curve from the photovoltaic simulation model is now added to the curves with and without PLL. In the best case, the simulation model should coincide with the analytical model with PLL. This is certainly the case for the dd and qq components, but the curves for the dq and qd components differ from each other. However, since the dd and qq components are the most important variables, the larger deviation in the other two components is not a major problem. One reason for the greater deviation in the coupling components could be the low values of the impedance in ohm and thus the calculation errors made by the programme.

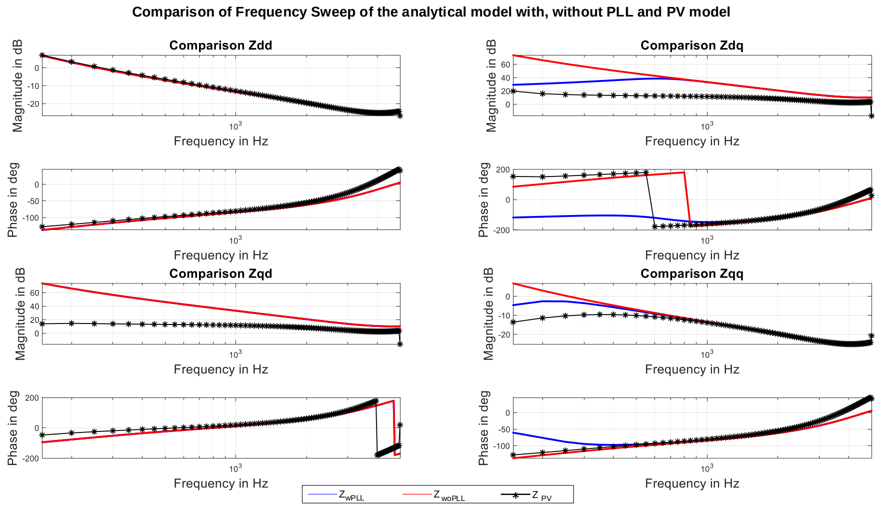

Figure 16: Comparison of analytical model with, without PLL and PV model impedance results

When considering the real part of the admittance, all four dq component curves agree very well and have only a slight deviation at higher frequencies.

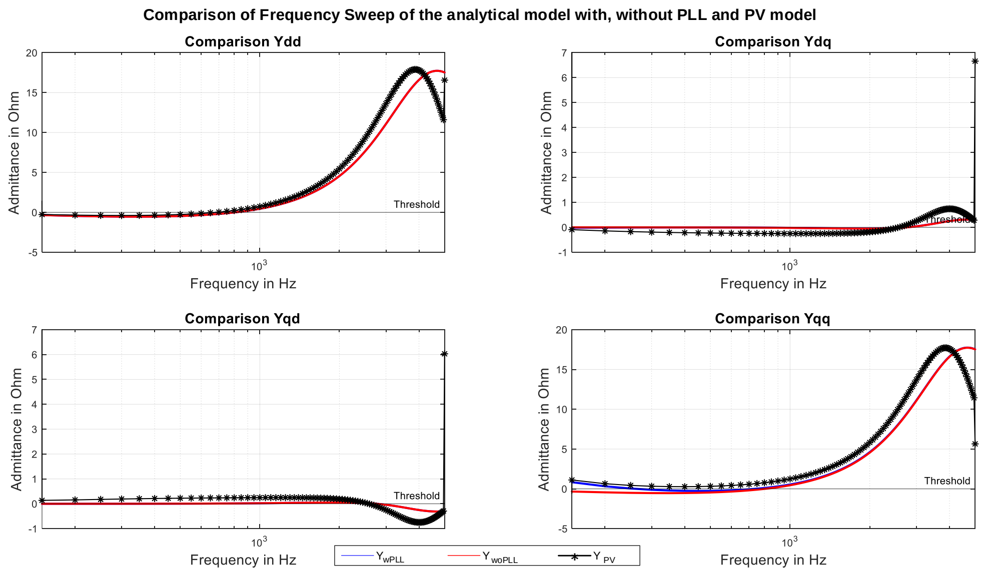

Figure 17: Comparison of analytical model with, without PLL and PV model real part of admittance

3.5 Validation of stability theory

To wrap up the chapter and to validate the stability theory and criterion with a simple example, a capacitance is connected in parallel to the photovoltaic model from the previous section. Figure 18 represents the Simulink model for this circuit. With a switch, the capacitance is connected to the grid after 1 s and thus changes the impedance of the whole grid system ($Z_g(s)$). With the impedance of the output filter of the inverter in combination with the parallel capacitance and the grid impedance a LCL-resonance circuit is formed. The voltage and current in dq-components in the inverter are measured as well as the current supplied to the grid.

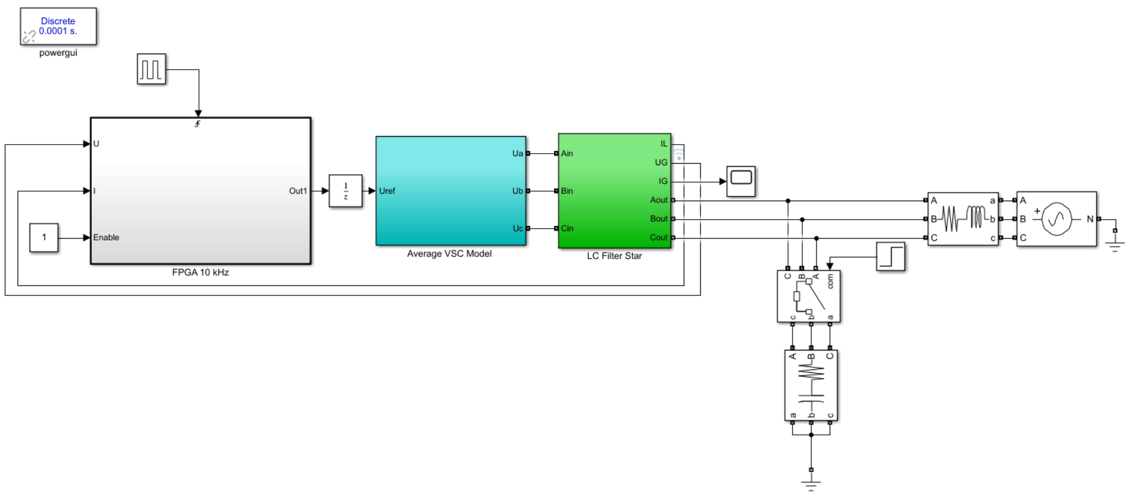

Figure 18: Grid with photovoltaic system and added capacitance

Now two different states are considered. For the first condition, a frequency point is selected at which the real part of the admittance has a negative amplitude and for the second frequency point the real part has a positive amplitude. According to the stability criterion, the voltage and current conditions should become unstable at the first frequency point and remain stable at the second, even though an additional capacitance is added.

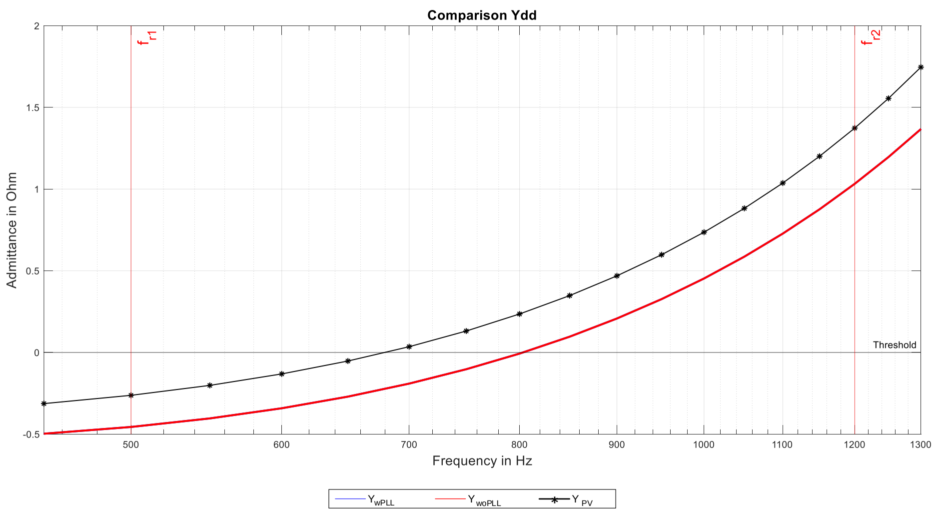

Figure 19: Comparison of f_r

In the first state, the resonance frequency f_{r1} = 500 Hz is selected. To verify the credibility of the stability criterion, the currents fed to the grid and the dq components of the voltage and current of the inverter are analysed.

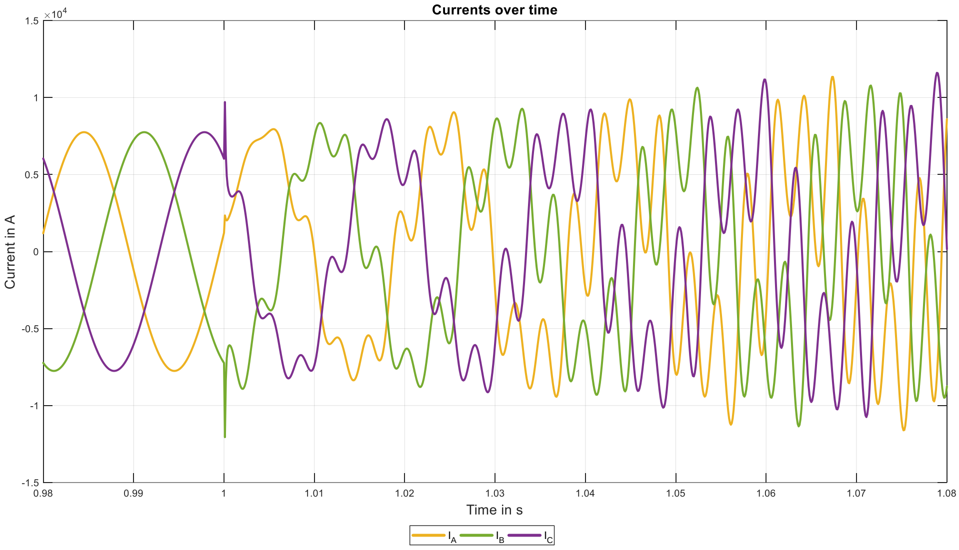

Figure 20: Current to the grid before and after connection case 1

In Figure 20, the three-phase currents fed into the grid are sinusoidal before the connection at 1 s, but they are no longer able to stabilise themselves after the capacitance is connected to the grid. As a result, the inverter acts as a resonance source as it now generates a negative damping and the voltage and current ratios are amplified and oscillate.

Furthermore, the amplitude of the currents is approximately doubled after 80 ms. If this happens in reality, this overcurrent would trigger the hardware protection of the inverter.

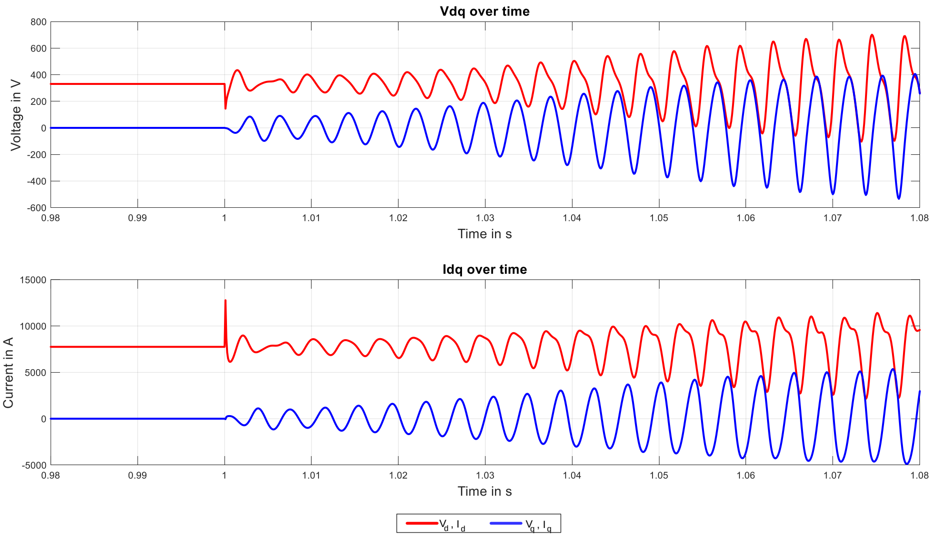

Figure 21: V_{dq} and I_{dq} of inverter before and after connection case 1

The same behaviour can also be seen in the dq components of voltage and current. The magnitudes no longer have a constant value, but increase their amplitude and begin to oscillate. Accordingly, the values of the controllers in the inverter change with the oscillation and lead to further instabilities.

This unstable behaviour of the grid system supports the stability criterion for the unstable case.

For the second case, the frequency point f_{r2} = 1200 Hz is used. Here, the black line of Figure 19 has a positive real part of the admittance and should, according to the stability criterion, guarantee stable voltage and current conditions even if the parallel capacitance is connected.

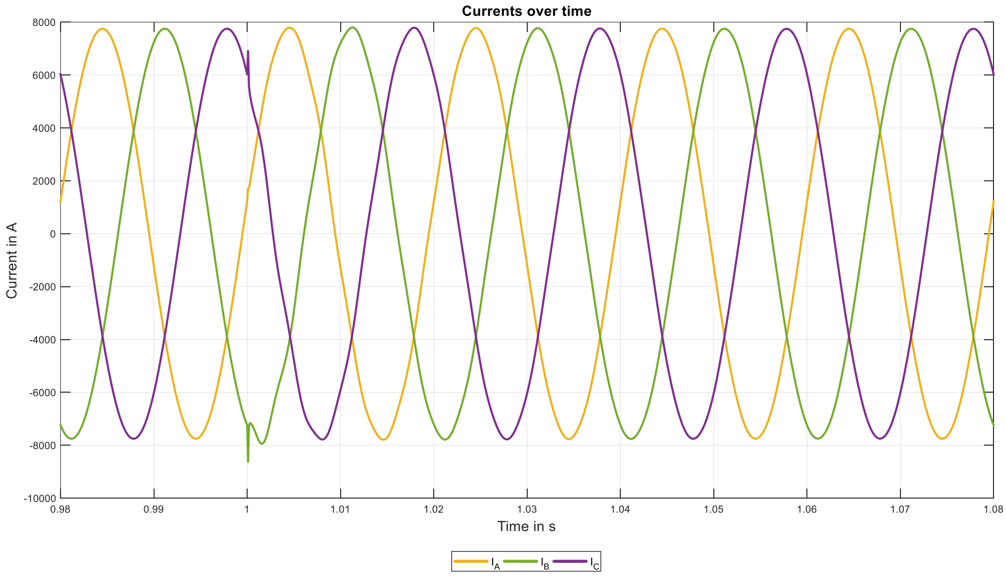

Figure 22: Current to the grid before and after connection case 2

In Figure 22, there is a small disturbance at 1 s when the switch connects the capacitance to the grid, but then the current ratios immediately settle again.

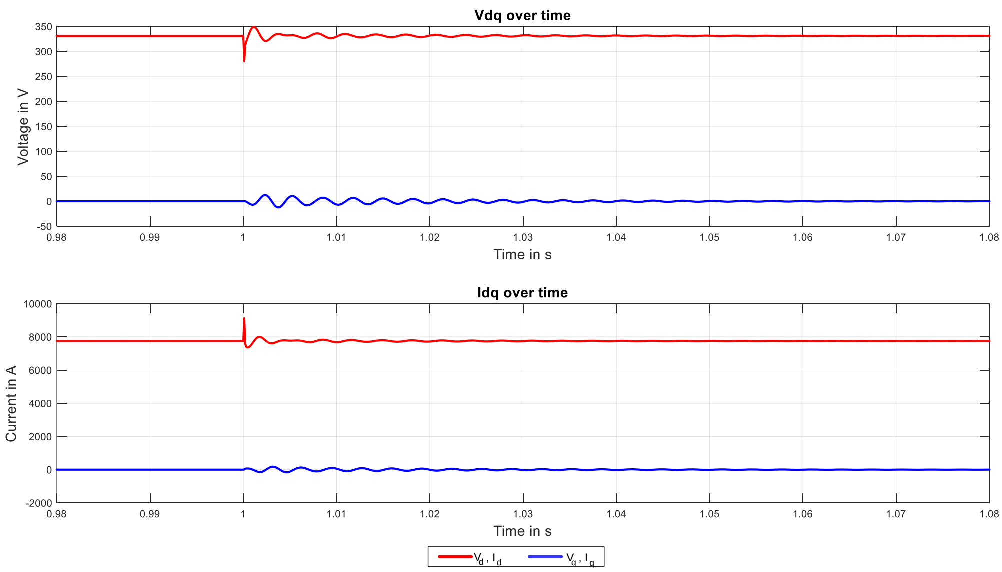

Figure 23: $\underline{V}_{dq}$ and $\underline{I}_{dq}$ of inverter before and after connection case 2

The same behaviour can be observed in the d and q components of the current and voltage of the inverter. At 1 s there is a small disturbance, but after less than 60 ms the conditions have returned to normal.

This stable behaviour of the grid system supports the stability criterion for the stable case. Since both tests fulfil the stability criterion, the integrity is validated.

3.6 Countermeasures for an unstable inverter behaviour

In the case of the tested components of this master thesis, the unstable behaviour described in section 3.5 is not detected, which means that it can be assumed that the industry grid remains stable when connected to the inverters and that there is no overcurrent and no additional harmonic generation by the inverter.

If the impedances of inverter and grid would not satisfy the stability criterion, where the real part of G(jω) is negative or the angle bigger [+π/2, -π/2], the inverter would behave like a resonance source at this frequency and generate a harmonic. In this case, countermeasures would have to be applied to be able to use the inverter anyway.

There are two methods to adapt the inverter to a specific grid. Possibility 1 is the filtering of this specific frequency with a harmonic filter of passive or active type. The filter is connected after the output of the inverter and filters out the frequency at which the stability criterion is not fulfilled. Possibility 2 is to change the control algorithm of the inverter. There are two options. In one method, the control topology is changed by adapted the inverter impedance to the grid by a virtual impedance. The other method directly changes the controller parameters of the inverter.

This second method will now be demonstrated. The same grid structure is used as in section 3.5, but the parameters of the current control loop are reduced. Then the first frequency point is selected again and it is determined whether the voltage and current ratios are now stable due to the change in the control parameters.

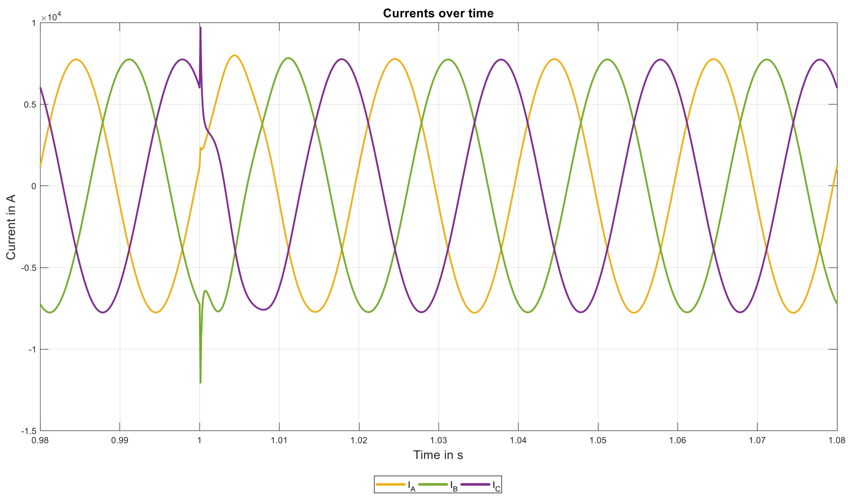

Figure 24: New controller parameters at $\underline{I}_{abc}$

As can be seen in Figure 24, by changing the controller parameters, the unstable voltage and current conditions are changed to a stable operation.

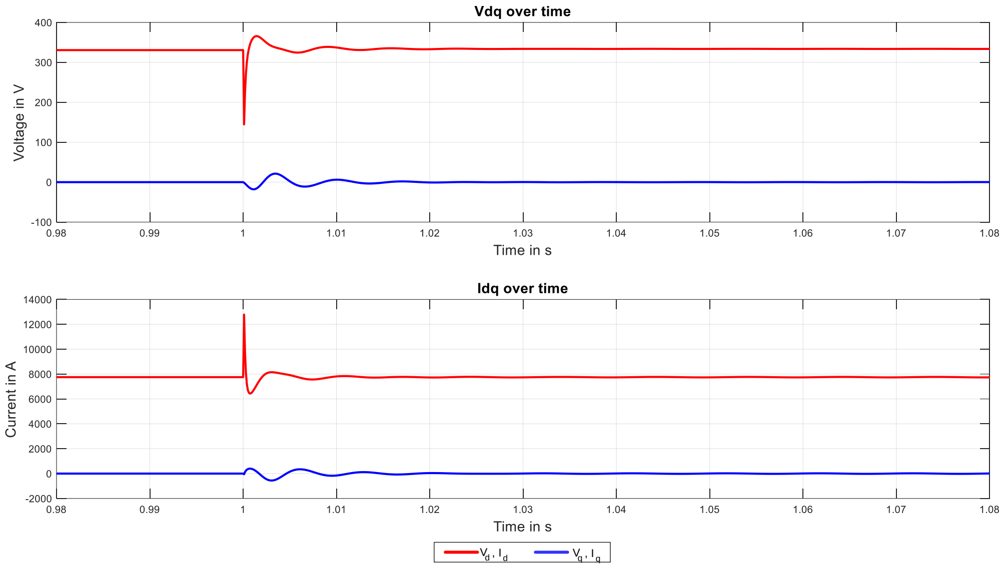

Figure 25: New controller parameters at $\underline{V}_{dq}$ and $\underline{I}_{dq}$

In addition, the same behaviour is observed for the dq components of voltage and current.

4 Field measurement and evaluation

In this chapter, the results of the field measurement and evaluation of the medium voltage grid are presented and a comparison with the simulation is made. The measuring set-up and the measuring devices are listed and the voltage situation at the most important two outgoing feeders are displayed.

4.1 Measuring set-up

The measurement of the medium voltage grid is carried out two times during the production of two different products, which gives the opportunity to document the influence of different production goods on the voltage situation.

During the measurement, all feeders of the 6 kV busbar are analysed with a 3-phase current measurement by current clamps and the values recorded with the DEWETRON DEWE2-A4 meter and TRON Series Modules over an observation period of one to two minutes. FLUKE i5s 600V CATIII AC current clamps are used to measure the current. The output of the current clamp is set at 400mV/A with a working range of 0.01 A - 5 A AC RMS at a frequency range of 40 Hz - 5 kHz. In addition, a 3-phase voltage measurement is recorded at the busbar.

Following the measurement, the recorded values are imported into Matlab and evaluated there. Of interest are the curves for active and reactive power as well as the current and voltage curves with a special focus on the 3rd , 5th , 7th , 11th , 13th , 23rd and 25th harmonic of all feeders.

On the following pages, the most important busbar feeders and outlets are displayed. Among them are the connection of the busbar to the transformer of the public grid operator “MV23” and the feeder to the extruder motor “MV24”. The analysis for the other busbar feeders is carried out in the course of this master thesis and show no noticeable problems.

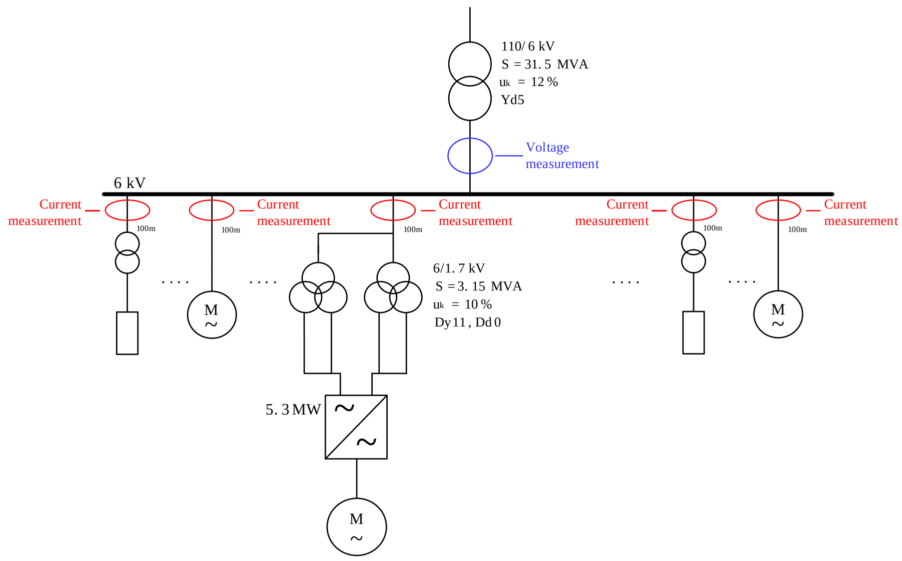

Figure 26: Measuring set-up for the field test (single-line scheme)

In reality, each busbar feeder had its own terminals to which the voltage and current transformers connected and to which also the measuring equipment is connected. For each measurement, a separate measurement file is created and the measurement recorded for at least 60 seconds.

Figure 27: Measuring set-up in reality

4.1.1 First measurement

The first measurement is recorded at standard production conditions.

4.1.1.1 Transformer feeder "MV23"

Feeder "MV23" represents the connection of the busbar to the transformer of the public grid operator.

Transformer 2 with S = 31.5 MVA is connected to feeder MV23. The transformer has vector group Yd5 and transforms the 110 kV voltage received from BAU B67A to the 6 kV phase-to-phase voltage. A 3-phase current measurement is carried out at this feeder on the secondary side of the transformer. The current transformer installed there has a transformation ratio of 1:4000.

<u>Diagram of voltage, current, active and reactive power:</u>

In Figure 28, the voltage and current are first shown as RMS values on the left-hand side. It can be seen that the values fluctuate only slightly over the measurement period of 100 s.

On the right side, the three-phase voltage and current curve is shown. The voltages displayed here (normal state of the grid) are the peak value of the phase-to-earth voltage and are defacto the same (approx. 10 V_{prim} difference). The current is represented as the peak value of the respective conductor current. Both curves have a correct sinusoidal shape without strong distortions.

The lower left diagram shows the active and reactive power. For a better representation, the mean value over time is calculated from both values. The two power curves also fluctuate only slightly over the measurement period.

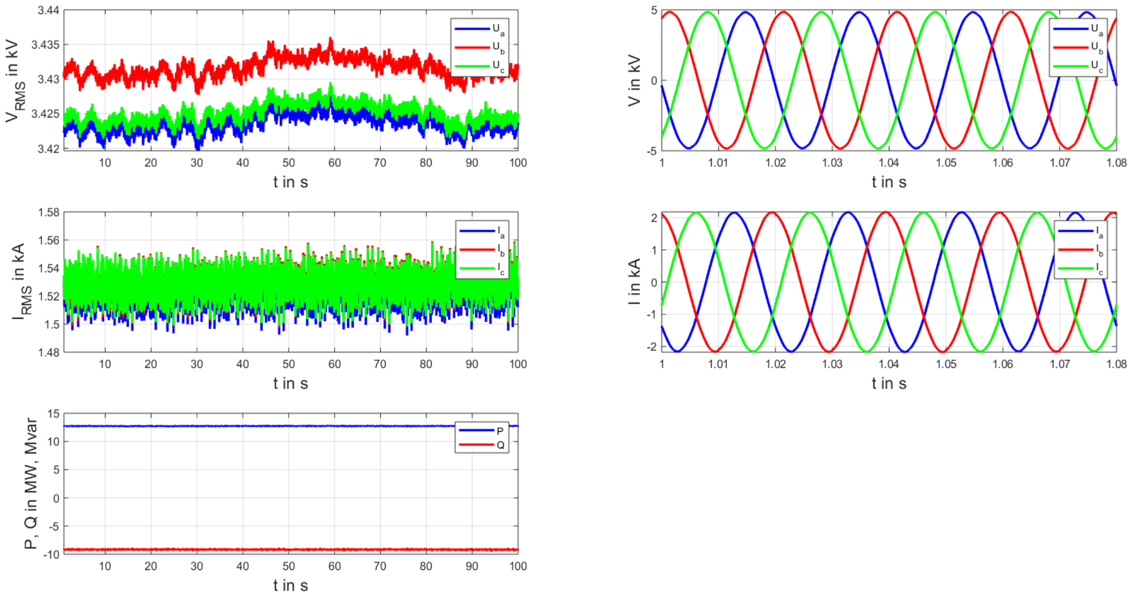

(a) (b)

Figure 28: (a) Curves of U, I, P and Q (b) zoom to four periods

<u>Diagram of the harmonics of voltage and current:</u>

In Figure 29, the harmonics of the voltage are shown on the left side and the harmonics of the current on the right side. Harmonics of the 3rd, 5th , 7th and 11th, 13th , 23rd and 25th order are always considered. For this feeder, the 17th and 19th order harmonics are also considered.

The voltage harmonics of the 5th , 11th and 13th order greater than 10 V_{prim}. The largest current harmonics also occur here in comparison to the feeders MV01-MV22. The 3rd, 5th , 7th and 11th order harmonics have very similar magnitudes.

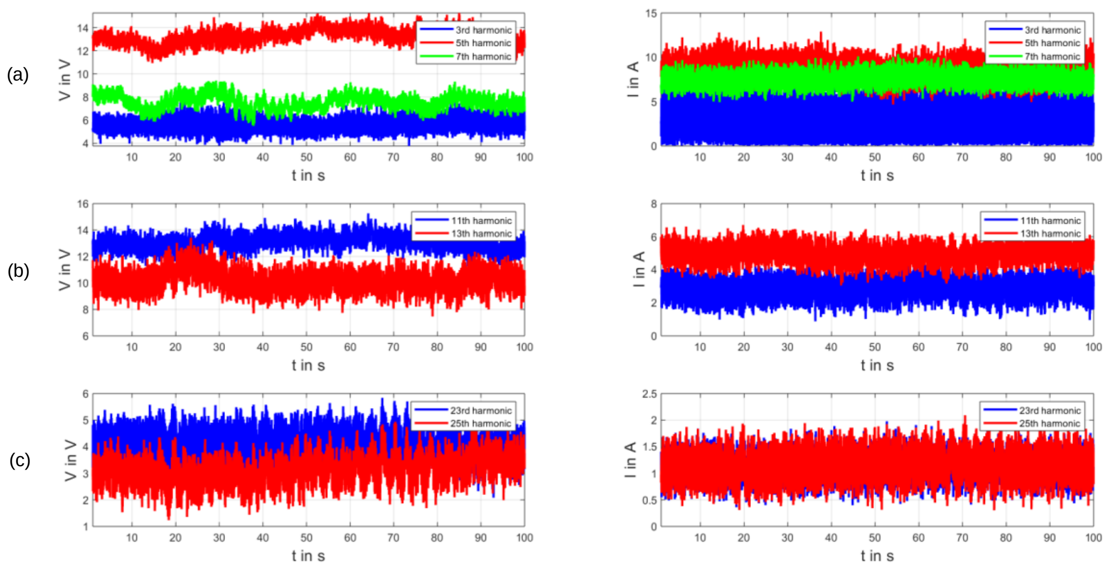

Figure 29: (a) Harmonics of 3rd, 5th, 7th (b) Harmonics of 11th, 13th (c) Harmonics of 23rd, 25th

4.1.1.2 Motor feeder "MV24"

Feeder "MV23" represents the connection of the busbar to the extruder motor.

The variable extruder motor with S = 2 x 3150 kVA is connected to outlet MV24 via the two transformers 20/21 wired in parallel. The transformers have the vector group Dyn11,Dd0 and transform the voltage of the 6 kV level to 1700 V. After the transformers, a 24-pulse inverter is installed that supplies the variable extruder motor. At this feeder, a 3-phase current measurement is carried out on the secondary side of the current transformer. The current transformer installed there has a transformation ratio of 1:600.

<u>Diagram of voltage, current and active and reactive power:</u>

In Figure 30, the voltage and current are first shown as RMS values on the left-hand side. It can be seen that the values fluctuate only slightly over the measurement period of 100 s.

On the right side, the three-phase voltage and current curve is shown. The voltages displayed here (normal state of the grid) is the peak value of the phase-to-earth voltage and are defacto the same (approx. 10 V_{prim} difference). The current is represented as the peak value of the respective conductor current. The voltage curve has a correct sinusoidal shape without strong distortions.

On the other hand, the course of the current shows clear distortions of the sinusoidal shape. These distortions are partly caused by the 24-pulse rectifier at this feeder.

The lower left diagram shows the active and reactive power. For a better representation, the mean value of both values is calculated over time. The two power curves also fluctuate only slightly over the measurement period.

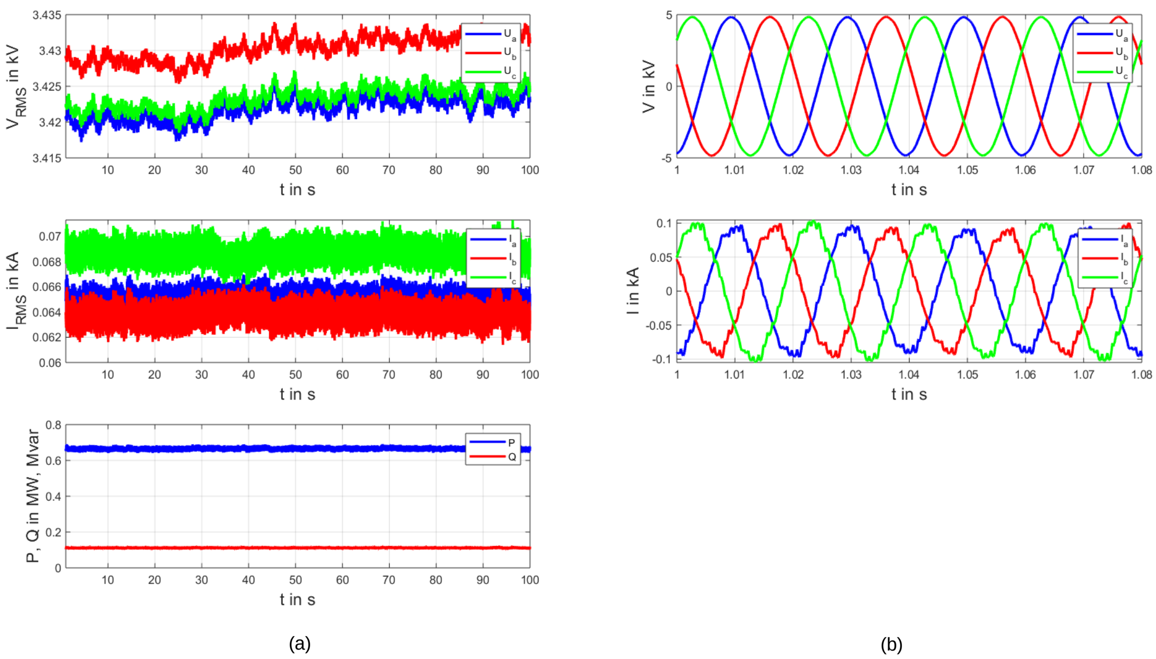

Figure 30: (a) Curves of U, I, P and Q (b) zoom to four periods

Diagram of the harmonics of voltage and current:

In Figure 31, the harmonics of the voltage are shown on the left-hand side and the harmonics of the current on the right-hand side. Harmonics of the 3rd, 5th , 7th and 11th, 13th , 23rd and 25th order are always considered. For this feeder, the 17th and 19th order harmonics are also considered.

For MV24, the 5th , 11th and 13th order voltage harmonics are greater than 10 V_{prim}. The largest current harmonics occur here at the 7th and 11th order.

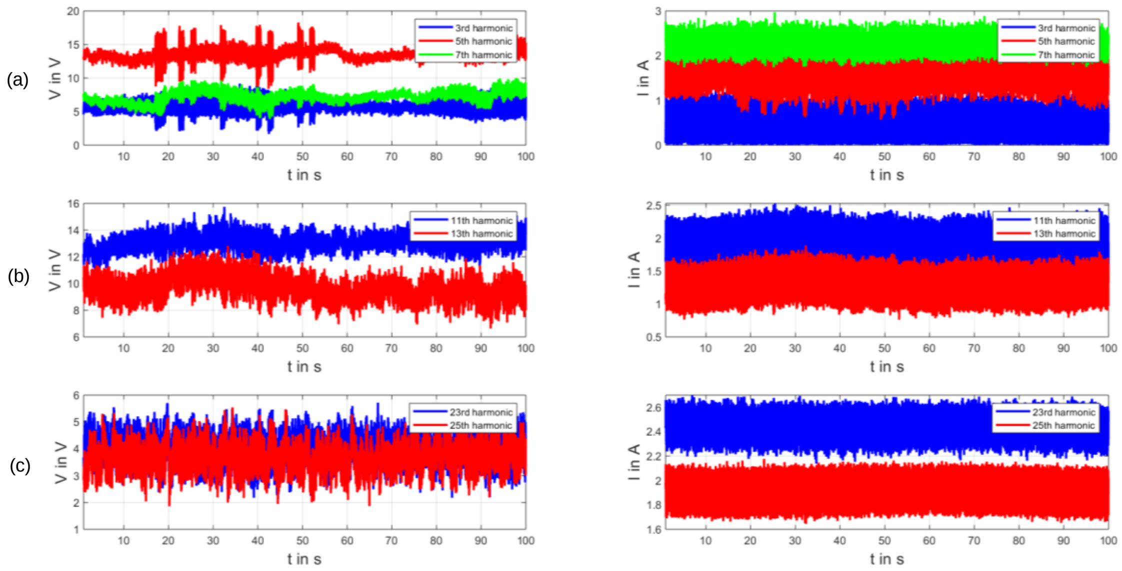

Figure 31: (a) Harmonics of 3rd, 5th, 7th (b) Harmonics of 11th, 13th (c) Harmonics of 23rd, 25th

4.1.2 Second measurement

For the second measurement, the production capacity is increased to the maximum of the production line, and the same measurement repeated.

For feeder “MV24” the increase process is documented over a measurement period of 30 minutes and three operating states are defined. Operating state 1 is at the beginning of the measurement, operating state 2 in the middle at 15 minutes and operating state 3 at the end at 30 minutes.

The values of voltage, current, active and reactive power stayed in the same range as the values from the first measurement, and only the proportions of the harmonics changed.

4.2 Comparison and results

4.2.1 Comparison between measurement and simulation

4.2.1.1 Transformer feeder "MV23"

During the measurement, the nominal value of the string voltage $\left(\frac{U_{rated}}{\sqrt{3}}\right)$ and the maximum effective value of the respective conductor current $\left(\frac{I_{peak}}{\sqrt{2}}\right)$ are specified. These values are therefore also considered in the simulation. For the harmonics, the mean values are considered for the measured values in each case.

In general, the basic oscillation values of voltage and current of the simulation correspond very closely to the values of reality, whereby the simulation gives a very good insight into the voltage and current relationships. For the voltage, there is an error of 1.04 %, for the current an error of 1.1 %.

The harmonic values of the simulation reflect the measured values quite well, although these are usually somewhat lower in the simulation because the current harmonics fed in by the other loads are not taken into account. All harmonics that are also present in reality occur in the simulation.

Table 12: Comparison of simulation and measurement MV23

Measurement			**Simulation**		
$U_{Extruder}$	3.43 kV		$U_{Extruder}$	3.29 kV	
$I_{31.5\ MVA\text{-}Trafo}$			$I_{31.5\ MVA\text{-}Trafo}$		
I_1	1.58 kA		I_1	1.43 kA	
	average	% of I_1		average	% of I_1
I_3	3.13 A	0.19 %	I_3	0.30 A	0.02 %
I_5	8.66 A	0.55 %	I_5	4.77 A	0.33 %
I_7	7.55 A	0.48 %	I_7	4.78 A	0.33 %
I_{11}	2.87 A	0.18 %	I_{11}	2.86 A	0.19 %
I_{13}	4.99 A	0.32 %	I_{13}	2.36 A	0.16 %
I_{17}	0.32 A	0.02 %	I_{17}	2.47 A	0.17 %
I_{19}	0.28 A	0.02 %	I_{19}	2.49 A	0.17 %
I_{23}	1.14 A	0.07 %	I_{23}	1.63 A	0.11 %
I_{25}	1.15 A	0.07 %	I_{25}	0.65 A	0.05 %
THD	**13.3 A**	**0.84 %**	**THD**	**6.31 A**	**0.44 %**

4.2.1.2 Motor feeder "MV24"

During the measurement, the nominal value of the string voltage $\left(\frac{U_{rated}}{\sqrt{3}}\right)$ and the maximum effective value of the respective conductor current $\left(\frac{I_{peak}}{\sqrt{2}}\right)$ are specified. These values are therefore also considered in the simulation. For the harmonics, the mean values are considered for the measured values in each case.

In general, the fundamental oscillation values of voltage and current of the simulation correspond very well to the values of reality, whereby the simulation gives a very good insight into the voltage and current relationships. For the voltage, there is an error of 1.04 %, for the current an error of 1.04 %.

The harmonic values of the simulation reflect the measured values quite well, whereby these are usually somewhat higher in the simulation. This is good for the subsequent simulation with a connected PV system, as stability with larger harmonic components indicates increased stability with lower harmonic components (reality).

All harmonics that are also present in reality occur in the simulation.

Table 13: Comparison of simulation and measurement MV24

Measurement			**Simulation**		
$U_{Extruder}$	3.43 kV		**$U_{Extruder}$**	3.29 kV	
$P_{Extruder}$	0.64 MW		**$P_{Extruder}$**	0.64 MW	
I_1	70.34 A_{eff} (reading)		**I_1**	68.04 A_{eff}	
	mean value	% of I_1		mean value	% of I_1
I_3	0.51 A	0.73 %	**I_3**	0.18 A	0.26 %
I_5	1.63 A	2.32 %	**I_5**	5.34 A	7.9 %
I_7	2.28 A	3.24 %	**I_7**	5.47 A	8.0 %
I_{11}	1.82 A	2.59 %	**I_{11}**	3.18 A	4.7 %
I_{13}	1.29 A	1.84 %	**I_{13}**	2.70 A	4.0 %
I_{17}	0.77 A	1.09 %	**I_{17}**	2.85 A	4.2 %
I_{19}	0.74 A	1.05 %	**I_{19}**	2.72 A	4.0 %
I_{23}	2.44 A	3.47 %	**I_{23}**	1.85 A	2.7 %
I_{25}	1.92 A	2.73 %	**I_{25}**	0.61 A	0.90 %
THD	**4.89 A**	**6.95 %**	**THD**	**7.08 A**	**10.4 %**

4.3 Photovoltaic system simulation based on field test result

According to the good accuracy of the simulation in relation to the measurement, the simulated photovoltaic model can now be added to the simulation and the voltage and current situations can be observed using FFT analysis.

The feeder of the frequency converter and the feeder to the transformer between the industrial grid and the public grid are discussed.

4.3.1 Transformer feeder "MV23" with photovoltaic system

For the consideration, the switch for the photovoltaic system is now closed in the simulation and then the simulation is started. The simulation is performed for a simulation period of 5 s, in order to observe any instabilities.

Voltage:

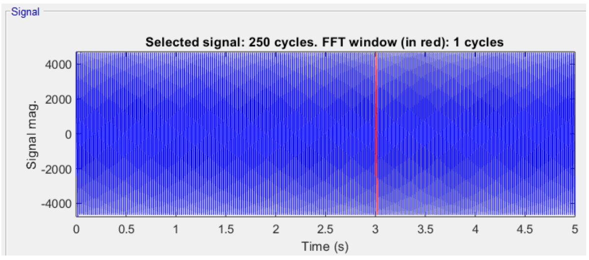

Current:

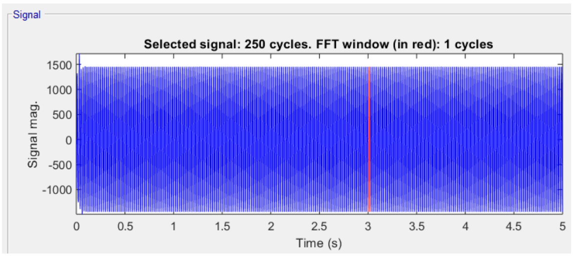

Figure 32: Voltage and current over time MV23

Over the entire simulation period, the current signal is stable and no instabilities occur. A very sinusoidal signal occurs with a THD of 0.90 %. This means that the total THD has increased by half, compared to the simulation without the connected photovoltaic system. The current drawn by the transformer drops to 1.02 kA.

The voltage signal is also stable over the simulation period. The voltage has a sinusoidal signal with a THD of 0.83 %. This means that the total THD has increased by half, compared to the simulation without the connected photovoltaic system. The phase voltage remains constant at 3.30 kV. This proves the stability of the voltage with the connected photovoltaic system.

4.3.2 Motor feeder "MV24" with photovoltaic system

As with the previous simulation, a simulation period of 5 s is also considered here.

Voltage: Current:

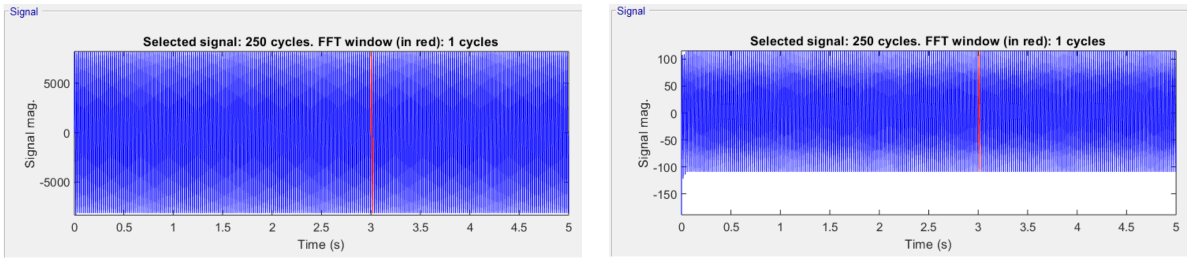

Figure 33: Voltage and current over time MV24

Over the entire simulation period, the current signal is stable and no instabilities occur. A sinusoidal signal occurs with a THD of 11.22 %. This means that the total THD has increased by about 1 % compared to the simulation without the connected photovoltaic system. The current remains constant with a value of 68.1 A. This ensures stability for the extruder motor from the point of view of the current.

The voltage signal is also stable over the simulation period. The voltage has a sinusoidal signal with a THD of 0.80 %. This means that the total THD has increased by half, compared to the simulation without the connected photovoltaic system. The phase voltage remains constant at 3.30 kV. This proves the stability of the voltage despite a slightly worse THD with the connected photovoltaic system.

4.4 Conclusion

4.4.1 Comparison of measurement and simulation

For the operating condition without the photovoltaic system, the simulation and measurement agree very well. This behaviour can be clearly seen in the voltage and current diagrams. Accordingly, the simulation represents a reliable starting point for further simulations. The next table shows the evaluation results.

Table 14: Measurement and simulation with PV

	Without photovoltaic system			**With photovoltaic system**	
Extruder THD		measurement	simulation		simulation
	current	6.95 %	10.40 %	current	11.22 %
	voltage	0.69 %	0.48 %	voltage	0.80 %
Transformer THD	current	0.85 %	0.44 %	current	0.90 %
	voltage	0.69 %	0.47 %	voltage	0.83 %

4.4.2 Interpretation

Extruder operation **without** photovoltaic system:

All harmonics that are also present in reality occur in the simulation. The harmonic values of the simulation reflect the measured values quite well, whereby these are usually somewhat higher in the direction of the safe side of the simulation. This increases the informative value of the simulation when the PV system is connected.

Extruder operation **with** photovoltaic system:

The voltage and current conditions at the extruder change only insignificantly when the photovoltaic system is connected.

5 Laboratory test

In this chapter, the dynamic case of the grid model is explored further. In the first section, the frequency sweep is described in more detail and the results are shown, explaining the stability of the individual components and relating them to each other. Here, the frequency sweeps of the simulations of the grid model as well as of two inverters in reality in the laboratory are performed. The inverters are from the same series as the inverters that will be used for the planned photovoltaic system, only they have a lower power because the impedance characteristic is not dependent on the output current and voltage. In the second section, the PHIL-test of the complete system is carried out with both inverters and thus the final evaluation of the overall system stability is given.

5.1 Frequency Sweep

The frequency sweep records the behaviour of the equipment over the selected frequency range. In the case of this master's thesis, the behaviour of the grid model and the behaviour of the inverter are of interest. These two results can then be put in relation to each other and a first statement about the stability can be made.

By building the ratio between the inverter impedance to the grid impedance the short circuit ratio (SCR) is displayed. With the SCR the relative strength and stability of a power system is analysed. Normally, the higher the SCR, the more stable the grid and the better the grid security. The lower the SCR, the worse the grid conditions and stability [29]. Everything above a SCR of 3 is a strong grid and very stable grid [32]. Everything lower than this number indicates instabilities in the grid.

5.1.1 Method description

In order to test the behaviour of any equipment over a wide frequency range and thus check the stability with the grid, a harmonic voltage or current must be fed in in addition to the fundamental frequency. This happens via an added voltage or current source [29].This verification process is called “Frequency Sweep”.

In the case of an added voltage source, this results in an output voltage of:

$$V(t) = V_{fm}\cos\left(2\pi f_{fm} + \theta_{vfm}\right) + V_{hm}\cos(2\pi f_{hm} + \theta_{vhm}) \qquad (100)$$

The first part of Formula (100) describes the fundamental frequency part and the second part the overlaid harmonic frequency. During the test process, the harmonic frequency part changes its frequency and the output impedance at every changed harmonic frequency can be measured [29].

With an additional voltage, also the current now consists of a fundamental part and a harmonic part of the same nature.

$$I(t) = I_{fm}\cos\left(2\pi f_{fm} + \theta_{ifm}\right) + I_{hm}\cos(2\pi f_{hm} + \theta_{ihm}) \qquad (101)$$

Applying this theory to the model of an inverter the output voltage has the following relationship:

$$\boldsymbol{V}(s) = \boldsymbol{Z}(s) \cdot \left[\boldsymbol{I}(s) - \boldsymbol{I}_{ref}(s)\right] \tag{102}$$

In the equation, every component is a 2x2 matrix. The current from the inverter $\boldsymbol{I}_{ref}$ is included in the equation. This current only contains the fundamental part due to the control strategy, and must be filtered out using a band stop filter, so only the harmonic part remains in the formula for the output voltage:

$$\boldsymbol{V}(s) = \boldsymbol{Z}(s) \cdot \boldsymbol{I}(s) \tag{103}$$

By transforming, the equation for the impedance is obtained.

$$\boldsymbol{Z}(s) = \frac{\boldsymbol{U}(s)}{\boldsymbol{I}(s)} \tag{104}$$

For a photovoltaic source, a current source adding the harmonics to the current must be fit into the model. In that case, only the harmonic current is produced, disregarding the fundamental part [29].

Now for small signal modelling, those equations have to be transformed into the dq-domain and the same process executed.

Taking Formula (103) and using it for a stationary abc three-phase system following equations for voltage and current can be obtained.

$$\begin{bmatrix} V_{ah}(t) \\ V_{bh}(t) \\ V_{bh}(t) \end{bmatrix} = \begin{bmatrix} V_{hm}\cos(2\pi f_{hm} + \theta_{vhm}) \\ V_{hm}\cos\left(2\pi f_{hm} + \theta_{vhm} - \frac{2\pi}{3}\right) \\ V_{hm}\cos\left(2\pi f_{hm} + \theta_{vhm} + \frac{2\pi}{3}\right) \end{bmatrix} \qquad \begin{bmatrix} I_{ah}(t) \\ I_{bh}(t) \\ I_{bh}(t) \end{bmatrix} = \begin{bmatrix} I_{hm}\cos(2\pi f_{hm} + \theta_{ihm}) \\ I_{hm}\cos\left(2\pi f_{hm} + \theta_{ihm} - \frac{2\pi}{3}\right) \\ I_{hm}\cos\left(2\pi f_{hm} + \theta_{ihm} + \frac{2\pi}{3}\right) \end{bmatrix} \tag{105}$$

Now the transformation to dq-domain is carried out and the voltage and current equation changes to:

$$\begin{bmatrix} V_{dh}(t) \\ V_{qh}(t) \end{bmatrix} = \begin{bmatrix} V_m \cdot \cos(\theta_{vh}) \\ V_m \cdot \sin(\theta_{vh}) \end{bmatrix} \qquad \begin{bmatrix} I_{dh}(t) \\ I_{qh}(t) \end{bmatrix} = \begin{bmatrix} I_m \cdot \cos(\theta_{ih}) \\ I_m \cdot \sin(\theta_{ih}) \end{bmatrix} \tag{106}$$

When calculating these expressions, both current and voltage only consist of real numbers and do not have an imaginary part. Since both relations have an angular frequency of $2\pi f_{hm}$, both current and voltage are converted into a DC value and the result only describes the linear part of the load impedance. Therefore, the total output impedance cannot be determined with this calculation alone [29].

To reflect the non-linear part as well, and get imaginary parts in the end result the angular velocity of the added harmonic cannot be the same as the angular velocity of the dq transformation.

For this reason, another frequency part is added to the angular velocity [29].

$$\begin{bmatrix} V_{ah}(t) \\ V_{bh}(t) \\ V_{bh}(t) \end{bmatrix} = \begin{bmatrix} V_{hm}\cos\left(2\pi(f_{hm} + f_p)t + \theta_{vhm}\right) \\ V_{hm}\cos\left(2\pi(f_{hm} + f_p)t + \theta_{vhm} - \frac{2\pi}{3}\right) \\ V_{hm}\cos\left(2\pi(f_{hm} + f_p)t + \theta_{vhm} + \frac{2\pi}{3}\right) \end{bmatrix} \tag{107}$$

$$\begin{bmatrix} I_{ah}(t) \\ I_{bh}(t) \\ I_{bh}(t) \end{bmatrix} = \begin{bmatrix} I_{hm}\cos\left(2\pi(f_{hm}+f_p)t+\theta_{ihm}\right) \\ I_{hm}\cos\left(2\pi(f_{hm}+f_p)t+\theta_{ihm}-\frac{2\pi}{3}\right) \\ I_{hm}\cos\left(2\pi(f_{hm}+f_p)t+\theta_{ihm}+\frac{2\pi}{3}\right) \end{bmatrix} \tag{108}$$

Now the dq transformation can be repeated with an angular velocity of $2\pi f_{hm}$ and the voltage and current determined.

$$\begin{bmatrix} V_{dh}(t) \\ V_{qh}(t) \end{bmatrix} = \begin{bmatrix} V_m \cdot \cos\left(2\pi f_p t + \theta_{vh}\right) \\ V_m \cdot \sin\left(2\pi f_p t + \theta_{vh}\right) \end{bmatrix} \qquad \begin{bmatrix} I_{dh}(t) \\ I_{qh}(t) \end{bmatrix} = \begin{bmatrix} I_m \cdot \cos\left(2\pi f_p t + \theta_{ih}\right) \\ I_m \cdot \sin\left(2\pi f_p t + \theta_{ih}\right) \end{bmatrix} \tag{109}$$

Based on these expressions, voltage and current are AC quantities with the frequency f_p.

5.1.1.1 Frequency sweep

The verification process via frequency sweep consists of five parts.

1. Connection of inverter and selection of the operating point for the measurement
2. Addition of voltage or current source without harmonic part and test for stability at fundamental frequency
3. Start of the frequency sweep in a selected frequency range by addition of harmonic
4. Repetition for each harmonic frequency and measurement of voltage and current
5. Calculation of impedance at each harmonic

The following flow chart displays the first four steps. In the next part, the last step of the frequency sweep, the calculation of the impedances, is described.

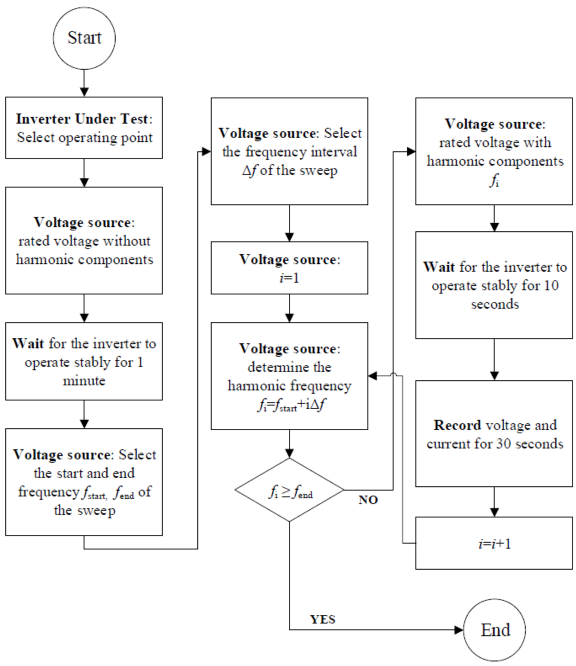

Figure 34: Flow chart of frequency sweep [29]

5.1.1.2 Measurement evaluation in dq-domain

The measurement takes place in a stationary three-phase system; therefore, the relationship between voltage and current is as follows:

$$\begin{bmatrix} V_a(t) \\ V_b(t) \\ V_c(t) \end{bmatrix} = \begin{bmatrix} Z_a & 0 & 0 \\ 0 & Z_b & 0 \\ 0 & 0 & c_a \end{bmatrix} \begin{bmatrix} I_a(t) \\ I_b(t) \\ I_c(t) \end{bmatrix} \tag{110}$$

According to Formula (110), the impedance in stationary abc components of each phase is independent of the other phases. After a transformation into Laplace-domain, this stays the same, however with a transformation according to the small signal analysis into dq-domain; the impedance obtains a coupling relationship [29].

$$\begin{bmatrix} V_d(s) \\ V_q(s) \end{bmatrix} = \begin{bmatrix} Z_{dd}(s) & Z_{dq}(s) \\ Z_{qd}(s) & Z_{qq}(s) \end{bmatrix} \begin{bmatrix} I_d(s) \\ I_q(s) \end{bmatrix} \tag{111}$$

Now instead of calculating one impedance at each harmonic, four impedances should be computed. To achieve this, two sets of linearly uncorrelated harmonic injections are necessary.

According to Formula (107) and (108), the angular velocity during the transformation has to be different to the injected frequency. Correspondingly, $2\pi(f_{hm} \pm f_p)$ would be a suitable way to determine the four impedances [29].

$$\begin{bmatrix} V_{dh1}(s) \\ V_{qh1}(s) \end{bmatrix} = \begin{bmatrix} Z_{dd}(s) & Z_{dq}(s) \\ Z_{qd}(s) & Z_{qq}(s) \end{bmatrix} \begin{bmatrix} I_{dh1}(s) \\ I_{qh1}(s) \end{bmatrix} \qquad \begin{bmatrix} V_{dh2}(s) \\ V_{qh2}(s) \end{bmatrix} = \begin{bmatrix} Z_{dd}(s) & Z_{dq}(s) \\ Z_{qd}(s) & Z_{qq}(s) \end{bmatrix} \begin{bmatrix} I_{dh2}(s) \\ I_{qh2}(s) \end{bmatrix} \tag{112}$$

With these two measurements, the four impedances in dq-domain can be measured.

$$\begin{bmatrix} Z_{dd}(s) & Z_{dq}(s) \\ Z_{qd}(s) & Z_{qq}(s) \end{bmatrix} = \begin{bmatrix} V_{dh1}(s) & V_{dh2}(s) \\ V_{qh1}(s) & V_{qh2}(s) \end{bmatrix} \begin{bmatrix} I_{dh1}(s) & I_{dh2}(s) \\ I_{qh1}(s) & I_{qh2}(s) \end{bmatrix}^{-1} \tag{113}$$

Now again the influence of the inverter current I_{ref} has to be filtered out with a Band stop filter and finally the accurate impedances in dq-domain can be calculated [29].

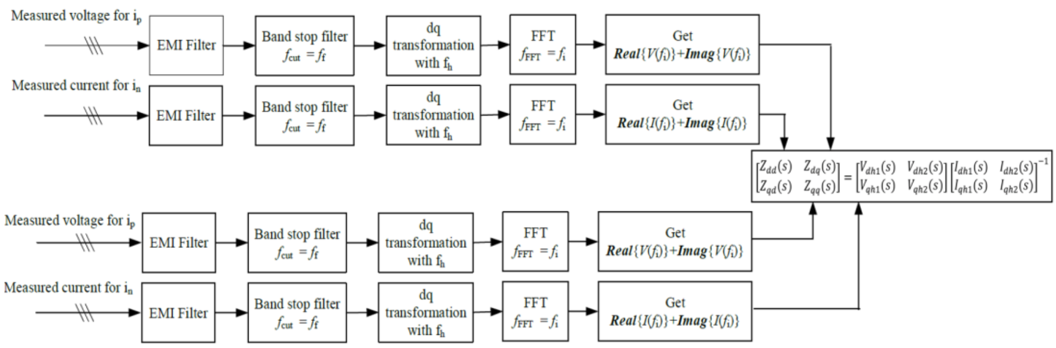

Figure 35: Schematic of the calculation process [29]

After calculating the four impedances for each harmonic, a plot of the impedance as a function of the used harmonics is a useful summary of the frequency sweep. From this, the stability criterion can be deployed and via the negative part of the admittance of each dq component unstable frequency ranges illustrated.

5.1.2 Results of frequency sweeps

Using the calculation scheme presented in the previous chapter, a frequency sweep of the real world inverters as well as of the simulation models of Simulink is conducted. Afterwards, the values can be compared in a diagram and a first statement about the basic stability can be given. A frequency range from 150 to 5000 Hz is investigated.

5.1.2.1 Frequency sweeps of real world inverters

During the frequency sweep of the inverters, they are switched on in the PHIL laboratory and the corresponding measurement data is obtained.

Table 15: Technical Data Inverter 1 and Inverter 2

Inverter 1:		**Inverter 2:**	
Input:			
Start Voltage	200V	Start Voltage	620 V
MPPT Operating Voltage Range	200 V – 1000 V	MPPT Operating Voltage Range	591 V – 1300 V
Output:			
Nominal AC Active Power	100 kW	Rated Output	92 kVA
Max. THD	< 3 %	Max. THD	< 3 %
Rated Current	144.4 V @ 400 V	Rated Current	3 x 132.3 A

<u>Measurement setup:</u>

To operate an inverter, a DC and an AC voltage are required. The DC voltage comes from the source, in this case the photovoltaic system, and the AC voltage is the link to the grid.

Since there is no real photovoltaic panel to generate the DC voltage, this is replaced in the lab with a power amplifier (PA). This PA generates the necessary DC voltage for the inverter. The DC voltage of both inverters is set to U_{DC} = 700 V. The AC voltage is supplied via a second PA. This PA generates a three-phase voltage with an amplitude of $U_{rms,\,p\text{-}p}$ = 400 V which equals $U_{rms,\,p\text{-}n}$ = 325 V. Both inverters are set to an operating point of 8 MW.

Then a harmonic current is additionally fed in and a three-phase current and voltage measurement is carried out. The transformer on DC side of Figure 36 decouples the ground connection, since in reality the photovoltaic installation also does not have the same ground potential. The magnitudes of the injecting voltage are matched to the PAs of the laboratory. This makes no difference to the impedance characteristics, as these are not dependent on the output current and voltage.

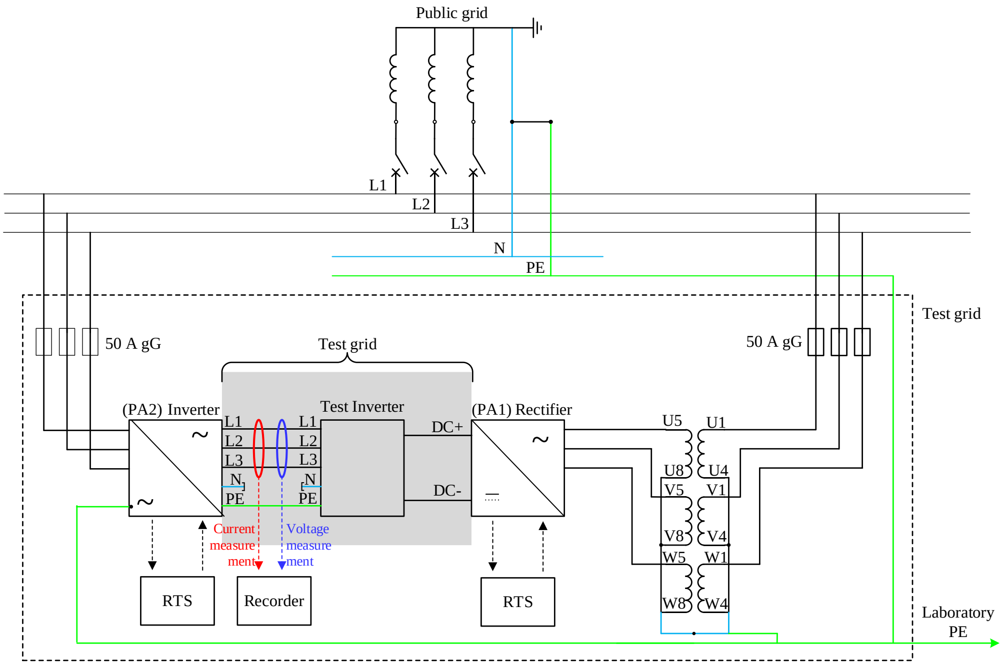

Figure 36: Laboratory setup frequency sweep

5.1.2.2 Frequency sweep of grid model

To make the frequency sweep of the grid model and measure the grid impedance, a current source is placed at the location of the inverters. The current source feeds in the additional current and calculates the values of the grid impedance for each harmonic current via a dq-transformation.

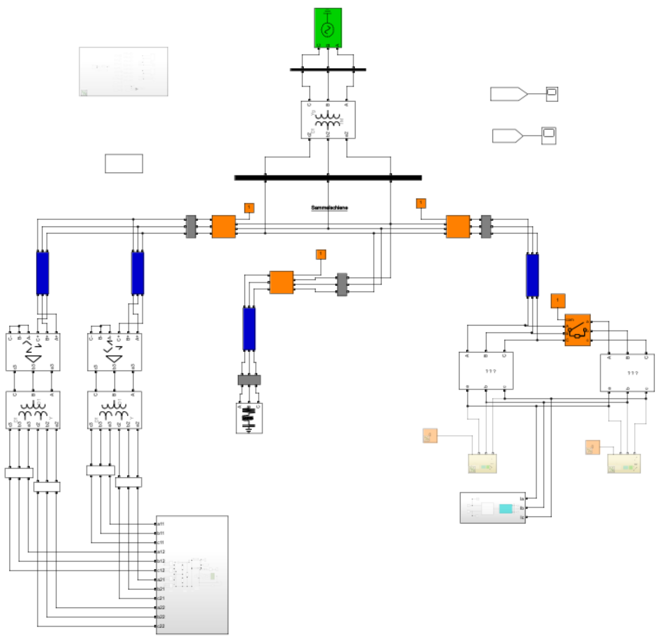

Figure 37: Simulation setup for frequency sweep

The current source consists of two blocks in Simulink. Block 1 contains the measuring device in which the transformation is carried out according to the verification process, and Block 2 consists of the reconstruction of a three-phase current source with parallel internal resistors. Block 1 is shown in the picture below for better understanding. The amplitude is determined on the basis of the maximum values of the current from the field test according to the following formula. Five percent of the base current amplitude is assumed and a ratio of 2:1 between the d and q components is adopted.

$$|I_{5\%}| = \sqrt{I_d^2 + I_q^2} \tag{114}$$

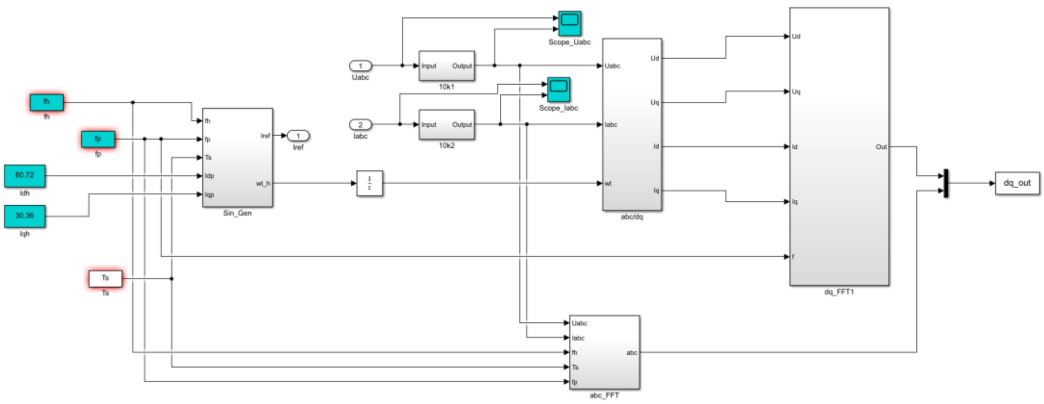

Figure 38: Measurement block

5.1.2.3 Frequency sweep results

The results of the frequency sweep are divided into two parts. First, the inverters alone are considered and their behaviour is discussed. Then the grid impedance is added in a common diagram and the result is explained.

Frequency sweep of real world inverters:

For the results of the frequency sweep of the real world inverters, the impedances in the dq-domain of the inverters are considered first and then the real parts of the admittance of the inverter. At the points where the real part of the admittance is negative, there is negative damping and instability in the event of resonance in the network.

Comparison of Zdd, Zdq, Zqd and Zqq of both inverters

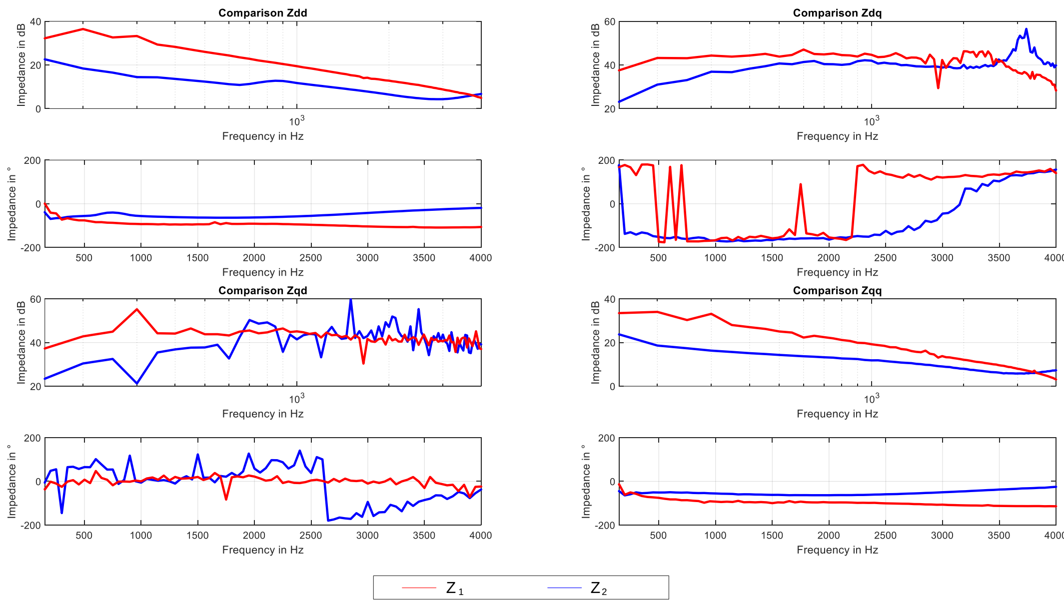

Figure 39: Comparison of inverter impedance of inverter 1 and 2

In Figure 39 the inverter impedance of the two tested inverters is displayed. As can be seen, the behaviour of both inverters is very similar over the selected frequency range, with inverter 2 generally having a lower impedance.

Comparison of Real part of Ydd, Ydq, Yqd and Yqq of both inverters

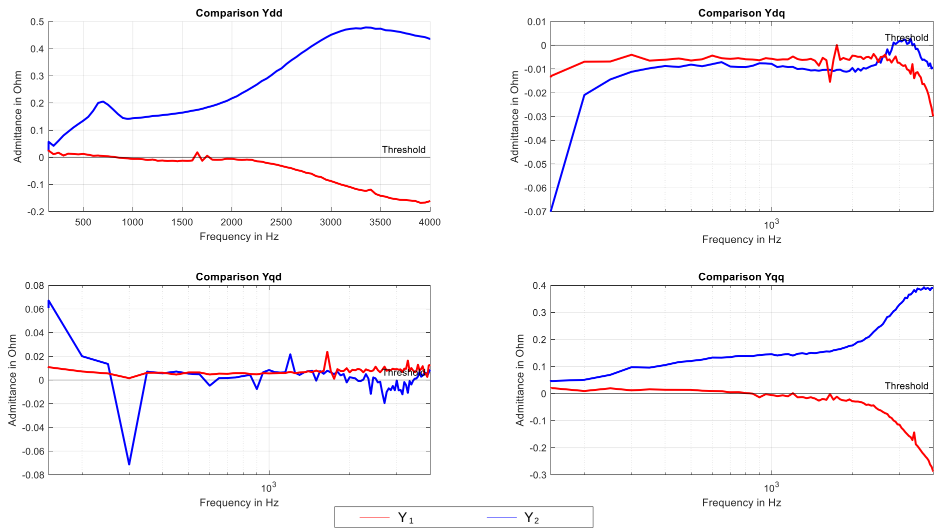

Figure 40: Comparison of inverter admittance of inverter 1 and 2

The focus is on the dd and qq components as they are more expressive than the coupling components. Due to the lower impedance of inverter 2, its real part of the admittance is generally higher than that of inverter 1 and there are larger ranges in which the real part is greater than zero. If the GNC is used, inverter 2 has a more stable internal behaviour. This could be due to a slower control of the inverter. However, this slower behaviour results in poor control in the event of sudden errors such as a fault ride through.

Frequency sweep of simulated grid impedance:

In the frequency sweep of the grid model, a passive behaviour of the impedance is generally assumed and therefore only the impedance is shown.

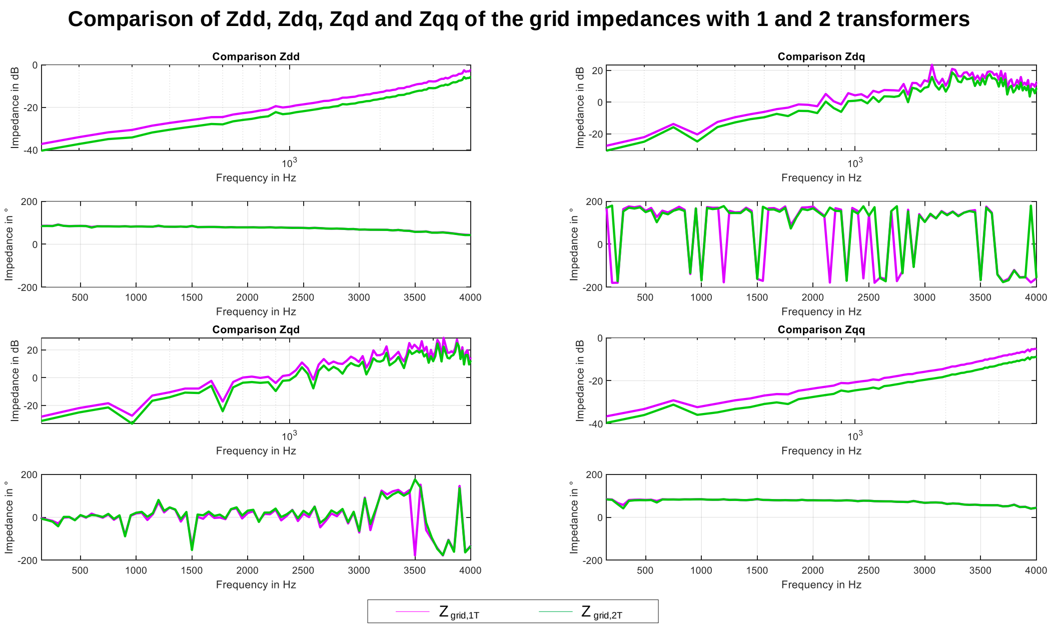

Figure 41: Comparison of grid impedance of 1 and 2 transformers

In Figure 41, the grid impedance is plotted for an operation with one transformer in the photovoltaic installation and compared to the grid impedance when using two transformers connected in parallel. As can be seen, the green line representing the grid impedance with two transformers is slightly smaller at all points. This behaviour makes sense, as the resistance value is reduced when impedances are connected in parallel.

The figure below shows the comparison between the inverter impedances and the grid impedance when operated with only one transformer of the photovoltaic system.

The pink line represents the grid impedance and it can be seen that the grid impedance is always lower than the inverter impedances. This behaviour follows the stability criterion very well, which means that the entire system is stable when the inverter is connected. The difference in amplitude at the point with the smallest distance is about 15 dB, which corresponds to a resistance value of 5.62 Ω and provides a large enough distance between the curves.

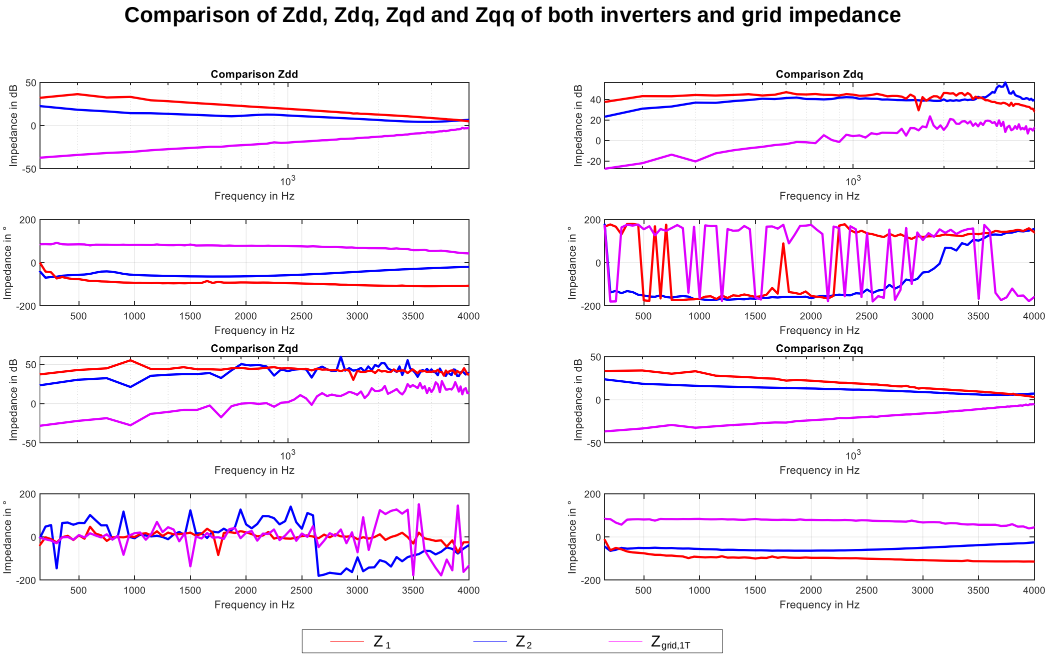

Figure 42: Comparison of inverters to grid impedance of operation with 1 transformer

Even with 2 parallel transformers and thus lower impedance, the inverter impedance of both inverters remains greater than the grid impedance in all components of the dq-domain. Again the stability criterion is followed very well, which means that the entire system is also stable when this inverter is connected. The difference in amplitude at the point with the smallest distance is about 10 dB, which corresponds to a resistance value of 3.16 Ω and provides a large enough distance between the curves.

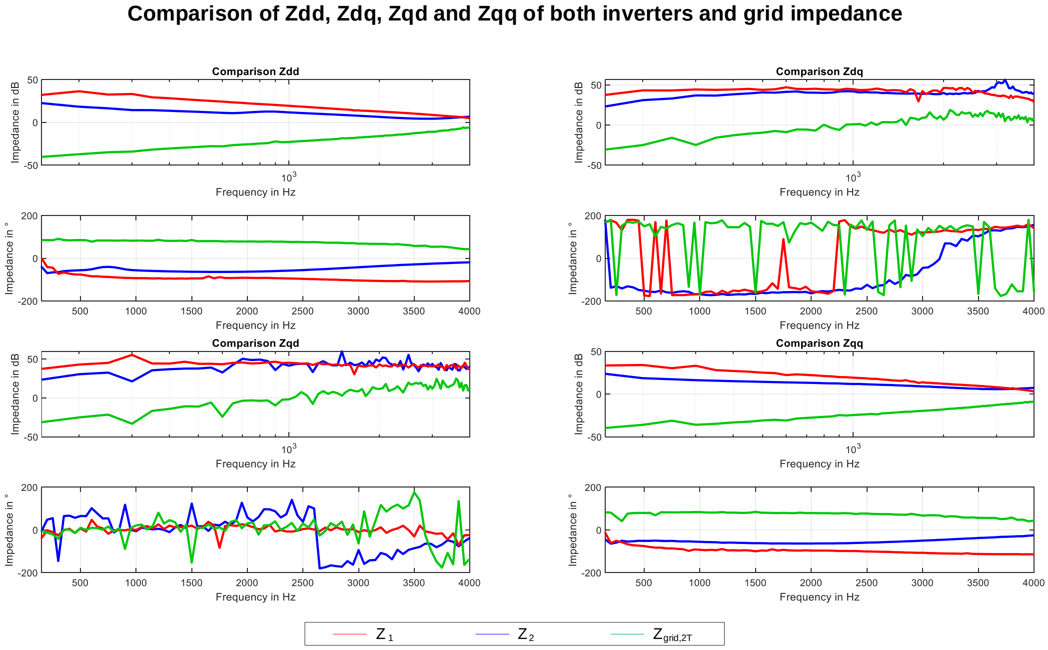

Figure 43: Comparison of inverters to grid impedance of operation with two transformers

5.2 PHIL – test

In inverter-coupled power supply systems, the dynamic characteristics strongly depend on the implemented control strategy. This fact has already been described in the previous pages by modelling the small-signal equivalent circuit of the inverter power system. In order to carry out a realistic examination of the entire system, a verification of the simulation can be carried out with so-called hardware-in-the-loop test methods.

By using Power/Controller-Hardware-In-The-Loop (PHIL or CHIL) systems, complex system behaviour during faults can be detected during planning. The grid connection behaviour of converter-coupled systems is mapped in simulations and these simulation models then verified by realistic results using power hardware-in-the-loop methods.

PHIL tests are used to carry out a realistic examination of the overall system. In a PHIL test, the network and the generating system are evaluated in a real-time simulation (RTS). In this context, Real time simulations means that all the needed parameters to control the system must be completely calculated within a time step. Therefore, only the inverter has to be an actual hardware device while the rest of the grid model can be simulated.

The results are then transferred to the tested inverter via a power amplifier (PA). The power amplifier calculates for every time step the needed values and transmits the values back to the inverter. As a result, the inverter behaves in this configuration in the same way as in a real environment. With a PHIL-test, the system behaviour during large disturbances, like a three-phase fault can be examined, without any stress for real world equipment [33].

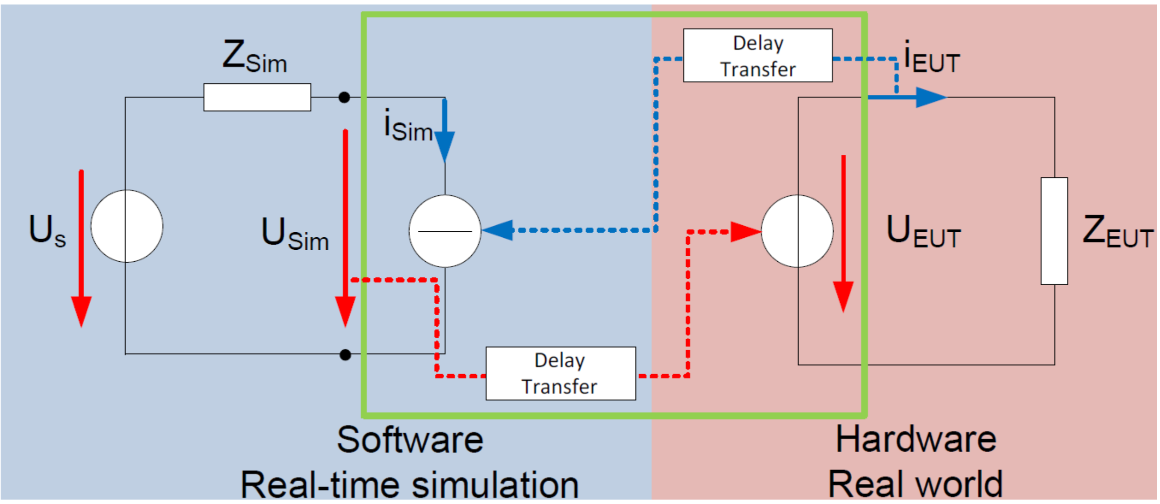

Figure 44: Topology of a PHIL test [33]

The setup of this master's thesis with a photovoltaic on the generation side and the inverter to be tested changes the schematics. Since photovoltaic as a source does not change its voltage generation rapidly and the target time constant is smaller than 1 second, it can be represented by a constant DC source, which corresponds to a rectifier. A PA, generating a DC voltage, represents this rectifier.

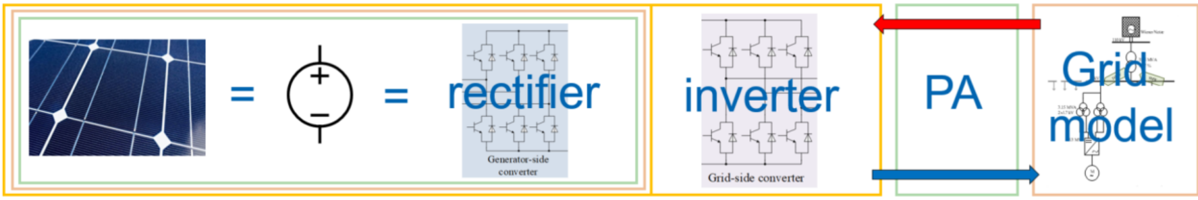

Figure 45: Schematic of the PHIL test of this master thesis

The verification process of the stability analysis in this master thesis is based on [29] with power-hardware-in-the-loop (PHIL) testing. In the document, a quick verification process for local and global stability is explained. For a small signal stability analysis, the local stability is of interest.

5.2.1 Method description

For the PHIL test, four different programmes are used for control. First, the two PAs are switched on via ACScontrol and the corresponding values for DC and AC voltage generation are set. The values are adjusted to the same amplitudes as for the frequency sweep. U_{DC} = 700 V and $U_{rms,\ p\text{-}p}$ = 400 V which equals $U_{rms,\ p\text{-}n}$ = 325 V. Then the grid model with photovoltaic system can be imported via Matlab/Simulink and the required current and voltage values connected to the inputs and outputs of the RTS system dSpace by importing the Simulink programme into Configuration Desk. After the inputs and outputs are linked, the file is compiled and an overview of the voltages and currents is created in Control Desk for monitoring during the test. Via Control Desk, the variables of the Simulink file can be modified during operation and thus the whole system can be controlled.

During the PHIL-test, the current from the inverter is increased with the multiplication by I_{gain} to simulate a much higher current than in reality possible. The inverter in the laboratory is set to 8 % of the rated power, equalling P = 8 kW, to achieve the worst-case scenario for the test. During the test, I_{gain} is increased from 1 to 50 and the voltage and current recorded. Figure 46 shows this relation between hardware and software.

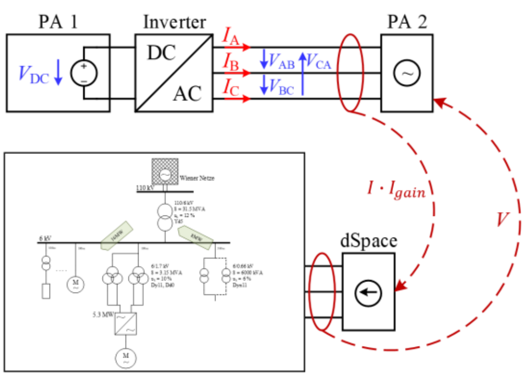

Figure 46: Laboratory setup scheme in combination with RTS connection

5.2.2 Laboratory setup

Based on the schematics above and [29], the laboratory set up of a PHIL laboratory needs two AC/DC voltage power amplifiers, a set of real-time simulators and an integrated measurement and control system. In the setup of the master thesis, PA1 simulates the voltage of the photovoltaic installation and supplies the inverter to be tested with its DC source. PA2 supplies the three-phase voltage from the grid and represents the connection to the grid. The inverter in the grey box is the real world inverter to be tested. The transformer on DC side decouples the ground connection, since in reality the photovoltaic installation also does not have the same ground potential.

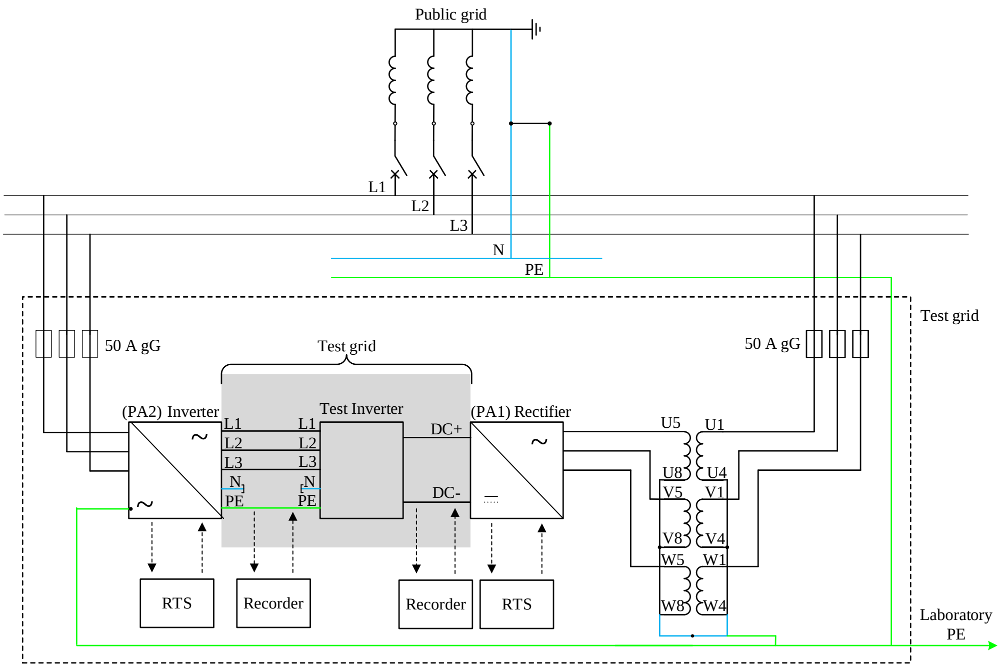

Figure 47: Laboratory setup PHIL-test

The next picture shows the PHIL laboratory during the test with the test set-up. The computers control the RTS system and all the necessary calculation programmes. The inverter represents the equipment under test (EUT) and the power amplifiers are located behind the green box.

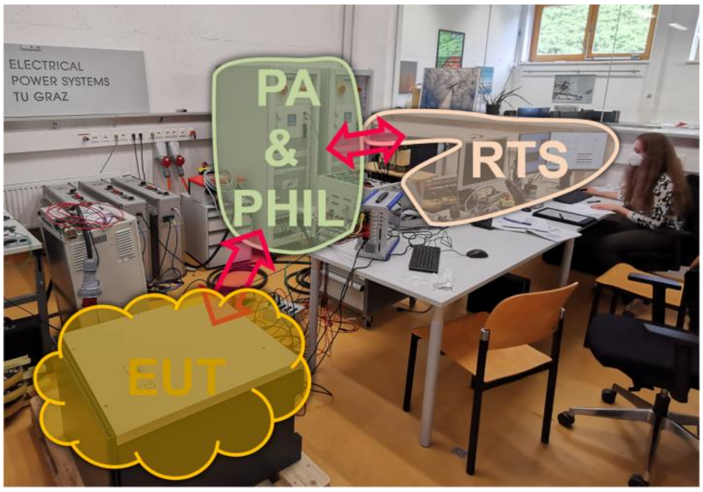

Figure 48: Picture of PHIL test in laboratory

5.2.3 PHIL – test results

5.2.3.1 Integrity of PHIL-test

In a correct PHIL-test, the voltage increases as the current increases. To prove the correctness of the PHIL-test, the RMS value over the entire test period is considered. If I_{gain} is increased, U must also increase accordingly.

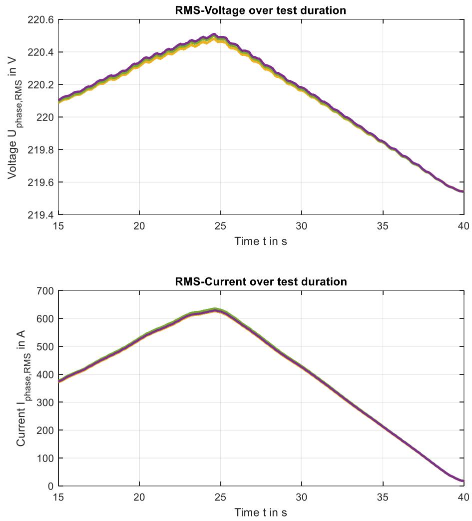

Figure 49: Correctness of PHIL-test

Figure 49 describes this behaviour very well. As I_{gain} increases, the voltage also increases, and as I_{gain} decreases, the voltage also decreases.

5.2.3.2 Results of PHIL-test

In the next two images, the stability of the entire system in the PHIL-test is considered.

Figure 50 represents the entire system with only one transformer for the photovoltaic system. Although, as previously described, the voltage must increase with increasing Igain, it must not become unstable and its value must only change in a small range.

On the left side of Figure 50 it is clearly visible that the current is increased and decreased again, but the voltage remains approximately constant over the entire time. Since the system does not oscillate, it can be deduced that the system remains stable with the inverter connected in the worst-case state and the photovoltaic system switched on, even with a much higher photovoltaic feed-in.

The right side shows the voltage and current at the maximum value of I_{gain} during a few periods. The voltage has a fairly accurate sinusoidal shape while the current contains many harmonics. The current contains these harmonics because the inverter is not operated at its rated power but only at 8 % of it. If the power of the inverter is increased, the curves of the current also become more sinusoidal. This is because an inverter always produces 3rd, 5th, and 7th order harmonics, but these are in comparison to the fundamental voltage and current at rated power according to the THD specified in the data sheet. Now only 8 % of the rated power is used and the harmonics are amplified with I_{gain}.

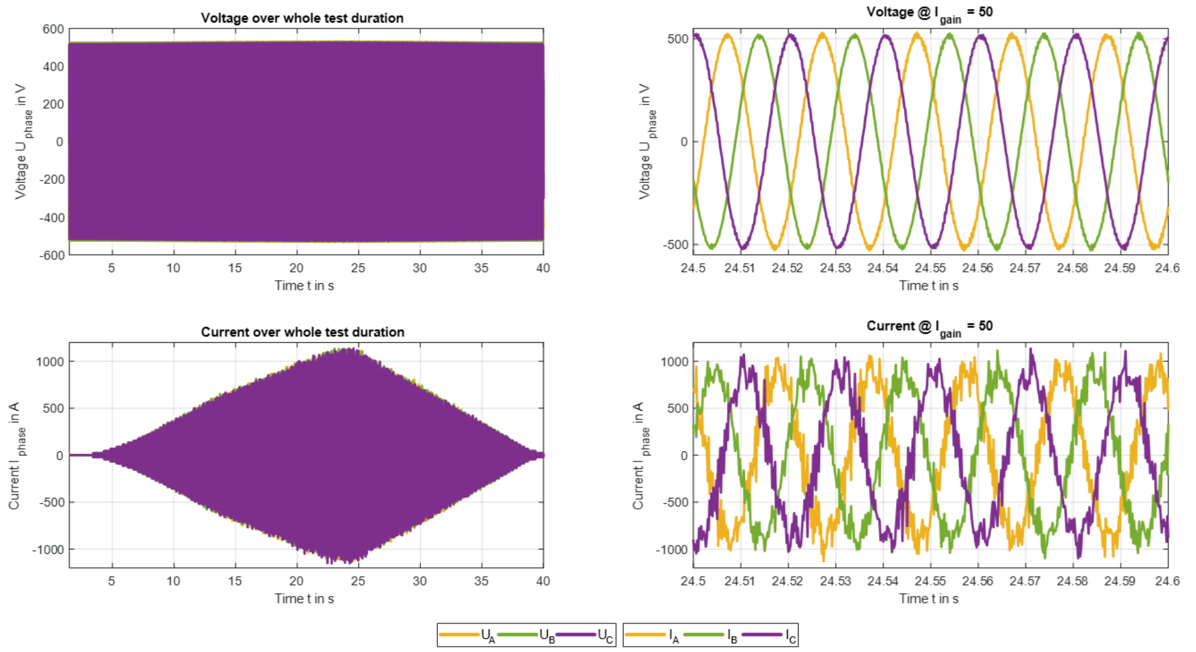

Figure 50: PHIL-test with grid model with 1 transformer

Figure 51 represents the entire system with 2 transformers connected in parallel.

On the left side of Figure 51 it is clearly visible that the current is increased and decreased again, but the voltage remains approximately constant over the entire time. Since the system does not oscillate, it can be deduced that the system remains stable with the inverter connected in the worst-case state and the photovoltaic system switched on, even with a much higher photovoltaic feed-in. Here, a longer time interval is maintained between the increases of I_{gain} than in the previous picture.

The same behaviour as with Figure 50 can be observed in the two images on the right.

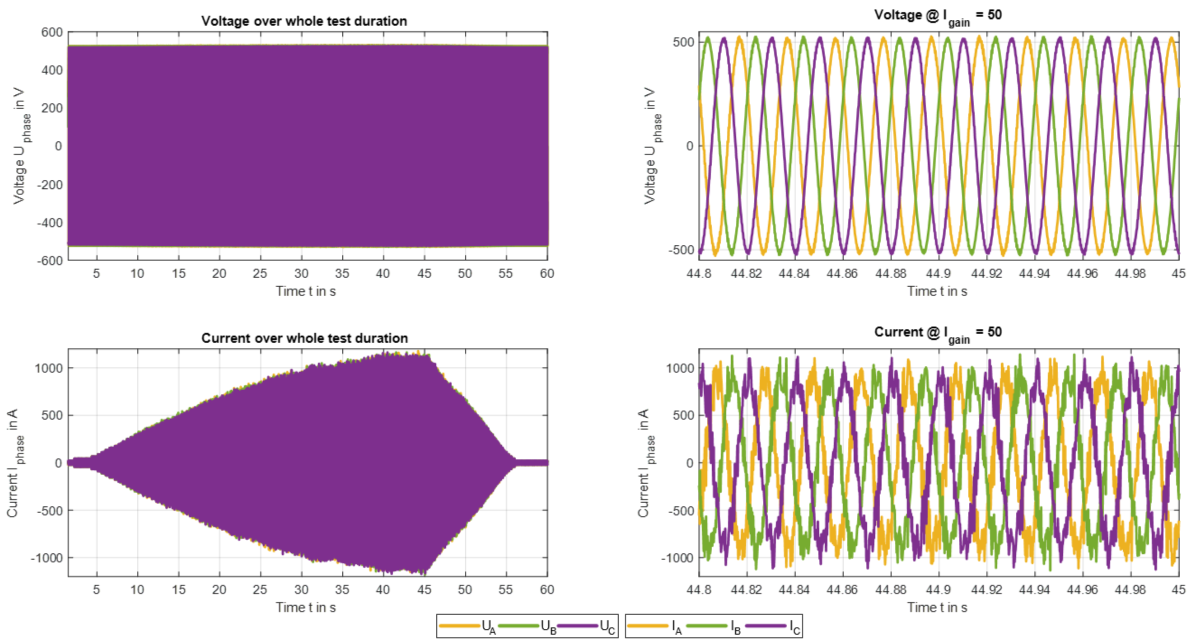

Figure 51: PHIL-test with grid model with 2 transformers

6 Summary and findings

6.1 Summary

In this master's thesis, the behaviour of a photovoltaic system is investigated when it is connected via an inverter to an industrial grid at 6 kV voltage level.

First, a grid simulation is designed in Simulink on the basis of the construction plans and then validated with a field test. During the field test of the industrial grid, a voltage and current measurement is carried out on each feeder and on the main busbar. After the verification with the results of the field test, it has been established that the simulation agrees very well with the values of reality. Thus, all subsequent considerations with the simulation lead to realistic results when adding a photovoltaic model.

Two types of instabilities are investigated for the industry grid. The first type of instability originates from the steady state and describes the instabilities that are generated due to the existing grid in one operating situation. Here only the voltage stability is examined in order to determine whether an undesirable voltage increase in the industrial grid would already occur with the planned power generation by the photovoltaic installation.

In the process, the limits of the maximum permitted voltage increase are determined by TOR-D2 and IEC 61000-2-4 and the formulas for voltage and current are defined based on the standards. It turns out that the feed-in of 8 MW of the photovoltaic installation only increases the voltage by 1.35 % at the main busbar of the industrial grid, which is far from the maximum permissible 10 %. Thus, it can be concluded from the steady state analysis that the power increase in the industrial grid caused by the photovoltaic installation alone will not lead to any problems, but that the correct cable cross-sections should be ensured for the connecting lines to the planned photovoltaic system.

The second source of instability is described by the transient case. Here, instabilities are investigated that arise due to the control algorithm as well as the dimensions of the inverter itself. In the course of the analysis, the impedance-based approach and the generalized Nyquist criterion provide an appropriate method for checking the stability of the individual components as well as the connection of all components.

The grid system is divided into two subsystems, one consisting of all components up to the connection point of the inverter and the second consisting of all components from the connection point of the inverter to the photovoltaic installation. Based on the separation of the systems, the impedance of these two subsystems can be calculated and their frequency response over a fixed frequency range observed by applying the frequency sweeping algorithm. Two inverters from different manufacturers that are suitable for building the photovoltaic system are reviewed in a laboratory test. A difference in the impedance of the inverters can be observed, which indicates that the controller and the components of the inverters are regulated differently.

The simulation of the industrial grid is also subjected to a frequency sweep in the same frequency range. For this, a current source is placed at the connection point of the inverter, which produces a harmonic that is superimposed on the fundamental current. With the frequency behaviour of the inverters and the grid obtained, a comparison of the curves can now be carried out and the impedance examined according to the stability criterion.

First, the impedances are considered individually and the real part of the admittance of the individual components is analysed. According to the stability criterion, a component/system is stable at a certain frequency if the real part of the admittance at this frequency is greater than zero. Since both inverters have negative real parts, the inverters have an instability at these frequency ranges according to this method. If now a resonance would occur from the grid impedance exactly at this frequency, the inverter would act like a resonance source and amplify this resonance by a negative damping. This would lead to a higher current load in the grid, which could overload the equipment.

Therefore, it must be determined whether the ratio between inverter impedance and grid impedance fulfils the stability criterion. This comparison corresponds to the ratio between inverter impedance and grid impedance over the entire frequency range, which is also called short circuit ratio. The short circuit ratio provides information about the stability of a grid. The higher this ratio, the more stable and secure the grid, and the less likely it is that harmonics will occur in the grid or that grid operation will be disrupted. By comparing the inverter impedance to the grid impedance, it can be determined; that the grid impedance is consistently lower than the inverter impedance by at least a factor of 10, resulting in a sufficient reserve between the two curves. Accordingly, the grid should not have any problems when connected to the inverter.

In the power-hardware-in-the-loop test, all three components, namely photovoltaic cell, inverter and grid, are tested together to obtain the overall system behaviour. Here, the simulation of the grid and the photovoltaic system is connected to the real world inverter via a real-time system, whereby the inverter behaves as if the grid and the photovoltaic panels are real hardware. Thus, the inverter also reacts as if it is in real grid operation. In the power-hardware-in-the-loop test, the inverter is operated in worst-case, which means that it is not operated at rated power but only at a small percentage of its rated power. Thus, it can be assumed that if the worst-case functionality is working correctly, it will also ensure the best-case functionality is provided. In addition, the current of the inverter is increased by the factor I_{gain} to a value that would not be possible in reality to test the behaviour of the inverter. During the tests, both inverters showed no difficulties of stability when connected to the simulated industrial grid as well as to the simulated photovoltaic installation, thus proving the overall system stability.

The industrial grid in connection with the photovoltaic panels and the inverter has thus successfully completed three stability tests, the steady-state test according to IEC 61000-2-4, the frequency sweeps based on the stability theory and the power-hardware-in-the-loop test. The voltage increase due to the one connected photovoltaic system does not increase needlessly, the system divided into subsystems has a stable behaviour up to 5000 Hz and the total system with connection of grid, inverter and photovoltaic is stable.

6.2 Outlook

Due to time constraints, only the models for an ideally symmetrical three-phase grid are carried out in the master's thesis. Therefore, the differences in the models for an asymmetrical grid would be of interest.

In addition, the resulting splitting into a positive sequence and a negative sequence and thus the following influences the d and q components.

Also, a comparison between the impedance curves of the frequency sweep between inverter model and real inverter would be interesting to be able to map the model of the inverter correctly via backwards engineering.

These points can be discussed in a following doctoral thesis.

7 Bibliography

[1] E. T. D. N. a. R. M. J. R. Aguero, “Modernizing the Grid: Challenges and Opportunities for a Sustainable Future,” *IEEE Power and Energy Magazine,* pp. vol. 15, no. 3, pp. 74-83, May-June 2017.

[2] X. W. a. F. Blaabjerg, “Harmonic Stability in Power Electronic-Based Power Systems: Concept, Modeling, and Analysis,” *IEEE Transactions on Smart Grid,* pp. vol. 10, no. 3, pp, My 2019.

[3] R. S. L. F. X. L. Q. C. a. Y. Z. Z. Zhang, “Hardware-in-the-loop Based Grid Compatibility Test for Power Electronics Interface,” *2019 20th International Scientific Conference on Electric Power Engineering (EPE),* pp. pp. 1-6, 2019.

[4] *IEC TS 63102:2021.*

[5] R.-C. L. C.-Y. C. S.-Y. C. J.-H. Teng, “Harmonic current predictors for wind turbines,” *Energies,* pp. 1314-1328, 2013.

[6] H. T. F. B. X. W. Z. H. a. S. G. H. Hu, “Train–Network Interactions and Stability Evaluation in High-Speed Railways–Part I: Phenomena and Modeling,” *IEEE Transactions on Power Electronics,* vol. 33, no. 6, pp. 4627-4642, 2018.

[7] C. R. P. W. S. H. N. Z. X. H. M. Chen, “Harmonic modelling and prediction of high speed electric train based on non-parametric confidence interval estimation method,” *Int J Electr Power Energy Syst,* vol. 87, pp. 176-186, 2017.

[8] E. S. E. Vasanasong, “The prediction of net harmonic currents produced by large numbers of residential PV inverters: Sydney Olympic village case study,” *Ninth international conference on harmonics and quality of power,* vol. 1, pp. 116-121, 2000.

[9] F. M. V. R. H.A.Pereira, “Harmonic current prediction by impedance modeling of grid-tied inverters: A 1.4 MW PV plant case study,” *International Journal of Electrical Power & Energy Systems,* vol. 93, pp. 30-38, 2017.

[10] J. J. A. A. a. T. S. T. Messo, “Time and frequency-domain evidence on power quality issues caused by grid-connected three-phase photovoltaic inverters,” *2014 16th European Conference on Power Electronics and Applications,* pp. 1-9, 2014.

[11] P. Kundur, Power System Stability and Control, New York, 1994.

[12] W. Cao, *Impedance-Based Stability Analysis and Controller Design of,* Tennessee, 2017.

[13] M. M. K. Z. X. Qianjin Zhang, “Stability problems of PV inverter in weak grid: a review,” *IET Power Electronics,* vol. 13, no. 11, pp. 2165-2174, 2020.

[14] W. X. a. B. F. Wang Y., “Harmonic instability assessment using state-space modeling and participation analysis in inverter-fed power systems,” *IEEE Trans. Power Electron.,* pp. 806-816, 2017.

[15] V. G. a. C. M. Guzman R., “Variable structure control for three-phase LCL-filtered inverters using a reduced converter model,” *IEEE Trans. Ind. Electron.,* pp. 5-15, 2018.

[16] G. A. I. R. C. T. R. B. a. B. C. P. E. I. Batzelis, “A State-Space Dynamic Model for Photovoltaic Systems With Full Ancillary Services Support,” *IEEE Transactions on Sustainable Energy,* vol. 10, no. 3, pp. 1399-1409, 2019.

[17] E. V. M. C. G. S. 1. S. 1. A. G. F. D. S. G. L. P. M. P. F. B. Giovanni Nobile, “Performance Assessment of Large Photovoltaic (PV) Plants Using an Integrated State-Space Average Modeling Approach,” *Energies,* vol. 13, 2020.

[18] J. Sun, “Impedance-Based Stability Criterion for Grid-Connected Inverters,” *IEEE TRANSACTIONS ON POWER ELECTRONICS,* vol. 26, no. 11, 2011.

[19] C. G. H. R. A. R. L. F. Ziqian Zhang, “Resonance Instability of Photovoltaic E-Bike Charging Stations: Control Parameters Analysis, Modeling and Experiment,” *Applied Sciences,* 2019.

[20] A. A. R. L. a. T. M. M. Berg, “Small-Signal Analysis of Photovoltaic Inverter With Impedance-Compensated Phase-Locked Loop in Weak Grid,” *IEEE Transactions on Energy Conversion,* vol. 35, no. 1, pp. 347-355, 2020.

[21] Q. Z. W. M. a. S. G. X. Zhang, “Impedance-based local stability criterion for standalone photovoltaic-battery hybrid system,” *2015 IEEE 6th International Symposium on Power Electronics for Distributed Generation Systems (PEDG),* pp. 1-6, 2015.

[22] B. D. a. L. F. Mao H., “Novel reduced-order small-signal model of a three-phase PWM rectifier and its application in control design and system analysis,” *IEEE Trans. Power Electron.,* pp. 511-521, 1998.

[23] a. B. Z. Sun J., “Input impedance modeling of single-phase PFC by the method of harmonic linearization,” *IEEE Appl. Power Electron. Conf., Austin, TX, USA, 2008,* pp. 1188-1194, 2008.

[24] S. A. a. V. G. Mattavelli P., “SSR analysis with dynamic phasor model of thyristor controlled series capacitor,” *IEEE Trans. Power Systems,* vol. 14, pp. 200-208, 1999.

[25] a. S. J. Cespedesand M., “Renewable energy system instability involving grid-parallel inverters,” *IEEE Appl. Power Electron. Conf., Washington, DC, USA, 2009,* pp. 1971-1977, 2009.

[26] W. X. a. B. F. Bakhshizadeh M., “Couplings in phase domain impedance modeling of grid-connected converters,” *IEEE Trans. Power Electron.,* vol. 31, pp. 6792-6796, 2016.

[27] a. S. J. Cespedes M., “Impedance modeling and analysis of grid-connected voltage-source converters,” *IEEE Trans. Power Electron.,* vol. 29, pp. 1254-1261, 2014.

[28] B. J. a. G. J. Baimel D., “Dynamic modeling of networks, microgrids, and renewable sources in the dq0 reference frame: A survey,” *IEEE Access,* vol. 2017, no. 5, pp. 21323-21335, 2017.

[29] Z. Zhang, *Test Guideline and Test Process of Power Hardware-in-the-Loop Test,* Graz: TU Graz – Institut für Elektrische Anlagen und Netze, 2020.

[30] E-Control, *Technische und organisatorische Regeln für Betreiber und Benutzer von Netzen - Teil D2.*

[31] *IEC 61000-2-4.*

[32] P. C. K. M. G. A. M. S. S. IEEE, “Experiences with Wind Power Plants with Low SCR,” *IEEE PES General Meeting,* 2015.

[33] Z. Zhang, *Power Electronics for Power Engineering,* Technical University of Graz, 2020.

[34] S. C. Gupta, “Phase-Locked Loops,” *Proceedings of the IEEE,* vol. 63, no. 2, 1975.

[35] F. Blaabjerg, Control of Power Electronic Converters and Systems, 2021.

[36] F. H.A.Pereiraa, “Harmonic current prediction by impedance modeling of grid-tied inverters: A 1.4 MW PV plant case study”.

8 List of figures

9 List of tables